

Eivind Ulstein Standal and Henning Levik Ørke

Flow field optimisation and stack design for Anion Exchange Membrane Water Electrolysis

Bachelor's project in Renewable energy, Engineer
Supervisor: Alejandro Oyarce Barnett

June 2020




Preface


This thesis, in a cooperation with SINTEF, is presented as the finishing Bachelor's degree of Engineering, ending the three year studies of Renewable energy at the Norwegian University of Science and Technology (NTNU).

Writing the report have been both challenging and time consuming, but also highly educational. We want to thank the people that has helped us with this thesis

Sincere thanks to our supervisor, Alejandro Oyarce Barnett (SINTEF), who gave us this rare opportunity and supportive guidance along the way. Also, to our external supervisors Stig Yngve Martinsen (SINTEF) and Tom-Andre Enebakk Eide (SINTEF), for all help and guidance. We would like to thank Simon Clark (SINTEF) for introducing simulation courses and other guidance, making us able to carry out the simulation methods. Thanks to Eugen Uthaug (NTNU) from the Department of Energy and Process Engineering, for lending us two licenses to COMSOL Multiphysics, making us able to perform the study with proper simulation tools. And lastly, thanks to Håvard Karoliussen (NTNU) who connected us with SINTEF to discuss the bachelor thesis.



Eivind U. Standal



Henning L. Ørke

Abstract

Anion Exchange Membrane Water Electrolysis (AEMWE) is a developing technology pursuing the mature PEM- and Alkaline water electrolysis technologies. Using the Anion Exchange Membrane (AEM) and an alkaline environment, the electrolytic process can be achieved with non noble metals as electrocatalysts, leading to a remarkable cost reduction. With this being state of the art technology, it still requires more research to advance, such as developing component materials specified for the AEMWE, ways to reduce the overpotentials, increasing the AEMWE efficiency, and membrane stability, during operation.

This thesis is an approach to optimise the flow field of the flow field plates by Computational Fluid Dynamics (CFD), and, to model, simulate and produce an AEMWE stack assembly with three cells of 50 cm². By our knowledge being one of the first in the world to produce an AEMWE stack assembly.

By designing the stack assembly, several things have been done to reduce the material usage. For instance, using two electrical insulated centre bolts, with passage through the stack assembly, reducing the volume of the end plates significantly. Another solution of the stack assembly, is attaching current terminals to the unipolar plates, avoiding the need for separate current collectors.

From fluid flow simulations in COMSOL Multiphysics, different flow field patterns and concepts have been analysed and compared to find the optimal solution for the flow field plates. The results have shown that by separately adjusting the inlet- and outlet channel design, the flow field can be even further improved, than by identical inlet- and outlet channels. The final optimisation resulted in a 50% flow distribution improvement in the most disadvantaged channel of the flow field.

Due to the corona virus, delays at the workshop lead to there being no practical tests of the stack assembly to present in the bachelor thesis.

Sammendrag

Anion Exchange Membrane VannElektrolyse (AEMVE) er en moderne teknologi med utspring fra PEM- og AWE vannelektrolyse. Anion Exchange Membrane (AEM) og et alkalisk miljø gjør at elektrolyseprosessen kan utføres med elektrokatalysatorer av uedle metaller, noe som fører til en betydelig kostreduksjon. Det at dette er relativt ny teknologi gjør at det fortsatt kreves forskning for videreutvikling, for eksempel utvikling av spesifikke komponentmaterialer for AEMVE, finne måter å redusere overpotensialer på, og å øke effekt og membranstabilitet under operering.

Denne rapporten er et forsøk på å optimere fluidfeltet til uni- og bipolare plater, ved hjelp av Computational Fluid Dynamics (CFD), og å modellere, simulere og produsere en AEMVE stack, bestående av tre celler med et aktivt areal på 50 cm². Gjennomføringen av dette fører til at vi (etter hva vi vet) er av de første i verden til å produsere en AEMVE stack.

Flere ting har blitt gjort for å redusere bruk av materiale, under modelleringen av AEMVE stacken. For eksempel er det brukt to strømisolerende bolter gjennom stacken, noe som fører til en bemerkelsesverdig volumreduksjon. En annen løsning som har blitt gjennomført er å designe de unipolare platene med strømterminaler, som fører til at det ikke trengs egne plater for strømtilkoblingen.

Fra simuleringene av fluidflyt i COMSOL Multiphysics har forskjellige konsepter blitt analysert og sammenlignet, for å finne de mest optimale løsningene til de uni- og bipolare platene. Resultatene viser til at fluidfeltet kan forbedres ytterligere, ved å justere inlet- og outlet kanaldesignet separat, enn å ha identisk inlet- og outletkanaler. Den endelige optimeringen viste en 50% forbedring av væskedistribusjon, i den mest vanskeligstilte kanalen i flowfieldet.

På grunn av omstendighetene rundt koronaviruset, og forsinkelser ved verkstedet, vil det ikke bli presentert praktiske stacktester i denne rapporten.

Contents

Preface	i
Abstract	ii
Sammendrag	iii
Introduction	1
1 Theory	2
1.1 Basic principles of water electrolysis	2
1.1.1 Cell potential	3
1.1.2 Actual cell potential	3
1.2 Low temperature water electrolysis	6
1.2.1 Mature water electrolysis technologies	6
1.2.2 AEM Water electrolysis	7
1.2.3 Status of water electrolysis technologies	8
1.3 Advanced technology	10
1.3.1 Polymeric Anion Exchange Membrane	10
1.3.2 Porous Transport Layer	10
1.3.3 Electrocatalyst layer	11
1.4 Stack assembly	13
1.4.1 Flow field plates	13
1.4.2 Gasket	14
1.4.3 End plate	14
1.5 Flow field theory	14
1.5.1 Channels	15
1.5.2 Ribs	16
1.5.3 Flow field pattern	17
1.5.4 The Navier-Stokes equations	18
1.6 Material Properties	19
1.6.1 Young's Modulus	19
1.6.2 Poisson's ratio	19
1.6.3 von Mises stress	20
1.6.4 Margin of safety	21
2 Methods	22
2.1 Solid edge	22
2.2 Stack design and materials	22
2.2.1 End plates	22
2.2.2 Flow field plate materials and design	25
2.2.3 MEA	29
2.3 COMSOL Multiphysics	30
2.4 Simulation	31
2.4.1 Computational Fluid Dynamics	31
2.4.2 Fluid flow simulation	33
2.4.3 Structural Mechanics simulation	34

2.5	Matlab	37
3	Results	38
3.1	Fluid flow simulation	38
3.1.1	Flow field pattern design	38
3.1.2	Centre channel variations	40
3.1.3	Channel depth	42
3.1.4	Inlet	44
3.1.5	Immersion channel	45
3.1.6	Channel width	48
3.1.7	Flow field with identical inlet/outlet	49
3.1.8	Final flow field	50
3.2	Structural mechanics simulation	55
3.2.1	Gasket compression	55
3.2.2	von Mises stress	58
4	Discussion	61
4.1	Flow field simulations	61
4.1.1	Choosing a flow field pattern	61
4.1.2	Centre channel optimisation	62
4.1.3	The effect of the channel depth	63
4.1.4	Inlet region	64
4.1.5	Flow field with identical sides	67
4.1.6	Final flow field simulations	67
4.2	Structural mechanics simulations	69
4.3	Stack components	71
4.3.1	End plate	71
4.3.2	Flow field plates	72
4.3.3	Stack assembly	72
5	Conclusion	74
A	Design solid edge	
A.1	End plate dimensions	
A.2	Bipolar plate dimensions	
A.3	Unipolar plate dimensions	
A.4	Bridge dimensions	
A.5	Gasket dimensions	
A.6	Flow field dimensions	
B	Components and materials	
B.1	Stainless steel 316 Datasheet	
B.2	Inconel 625 Alloy Datasheet	
B.3	EPDM 4000 HG-60 Datasheet	
B.4	Helical compression spring Datasheet	
B.5	RENY bolt Datasheet	

C Fluid flow simulations from COMSOL

C.1	Different flow field patterns	
C.2	Centre channels	
C.3	Different channel depths	
C.4	Inlet geometries	
C.5	Immersion channels	
C.6	Width of channels and inlet	
C.7	Flow field with identical inlet/outlet	
C.8	Final flow field	
C.8.1	Five channels	
C.8.2	Stack with one flow field	
C.8.3	Complete stack with three flow fields	
C.9	Fluid properties	
C.9.1	Water properties	
C.9.2	KOH properties	

List of Figures

1.1.1 Cell potential at different pH at SEP [10]	3
1.1.2 An illustration of the Tafel plot and the a and b parameters, edited from reference[11]	4
1.1.3 Polarisation curves of a typical anion-exchange membrane water electrolyser	5
1.1.4 Efficiency of a typical anion-exchange water electrolyser [12]	6
1.2.1 Operating principles of Alkaline and PEM water electrolysis.[17]	7
1.2.2 Polarisation curves of AEMWE with different catalyst for OER and Pt/c for HER, in 1M KOH (a) and 0.1M KOH(b) at 50°C, edited from reference.[21]	9
1.3.1 MEA, edited from reference [22]	10
1.3.2 Example of the chemical structure of a homogenous polysulfone AEM [22]	10
1.3.3 The conduction of water and evolved gas in the Porous Transport Layer [26]	11
1.3.4 CCS and CCM processes, edited from reference [30]	12
1.3.5 The electrocatalysts role in reducing the activation overpotential [31] . . .	12
1.4.1 Components of the AEMWE stack	13
1.5.1 Straight flow field pattern illustrating channel and ribs.[32]	15
1.5.2 Laminar and turbulent flow, edited from reference. [42]	16
1.5.3 Serpentine flow field (a) and straight flow field (b).[46]	17
1.5.4 Slugs forming in PEMWE at 2[A/cm ²] in the flow fields from figure 1.5.3, edited from reference. [46]	18
1.6.1 Graph illustrating a tensile test. [51]	19
1.6.2 Cube before and after stretching, illustrating a Poisson's ratio of 0.5. [56]	20
1.6.3 Stress-Strain Relationship under Uniaxial Tensile Loading [58]	21
2.2.1 End plate model, top- and bottom side, respectively	23
2.2.2 Swagelock couplings	23
2.2.3 Bolt and nut for stack clamping	24
2.2.4 Spring for bolt centering	24
2.2.5 procentage increase of ICR before and after corrosion testing at two different compression pressures	25
2.2.6 Illustration of the bipolar plate. Dimensions specified in appendix A.2.1. .	26
2.2.7 Illustration of the bridge (a) and the bridge assembled on the bipolar plate (b). Dimensions specified in appendix A.4.	26
2.2.8 Illustration of the unipolar plates. Dimensions specified in appendix A.3. .	27
2.2.9 Illustration of the the final flow field. Dimensions specified in appendix A.6.1.	28
2.2.10 Illustration of the gasket assembled on a bipolar plate. Dimensions specified in appendix A.5.	29
2.2.11 Gasket cut out with a template (a) and fitted on a unipolar test plate made from aluminium (b).	29

2.2.12	CCM fabrication procedure a) Catalytic ink solution, b) hot vacuum plate and c) finished CCM.	31
2.4.1	Illustrating a model with coarser and finer mesh.[71]	32
2.4.2	Flow field velocity simulation in COMSOL	33
2.4.3	Flow field pressure simulation in COMSOL	34
2.4.4	Compression simulation	34
2.4.5	Meshing of components	35
2.4.6	Extremely fine mesh, bridges	35
2.4.7	Compression simulation, 115 [N] per bolt: von Mises stress from the gasket compression, from above.	36
2.4.8	Simulating pressure on the inside of the gasket.	36
3.1.1	Velocity field in [m/s] for different flow field patterns, simulated at 50g/min from the inlet at the top.	39
3.1.2	Velocity fields in [m/s] of different centre channels with a flow rate of 50g/min. Inlet from the left with sub channel (1-5) from the top. Dimensions specified in figure C.2.1.	40
3.1.3	Illustrating the pressure drop distribution as contour lines at 50g/min over the channel in figure C.2.1b, with a channel depth of 1mm.	42
3.1.4	Pressure drop for different channel depths (0.5-1.3mm) of the channel in figure 3.1.3 as a function of the simulated flow rate.	42
3.1.5	Pressure drop over different geometries with a length of 1000mm, Pipe (6.35mm), duct (16.5x5mm) and duct with radius (2.5mm radius), illustrated in figure C.4.1.	44
3.1.6	Pressure contour of the different channel geometry under the bridge with a flow rate of 10g/min. The model dimensions are specified in figure C.5.1.	45
3.1.7	Pressure contour of the channel ramp under the bridge, where the channel is moved up 1mm in 1, 1.5, 2 and 3mm. The model dimensions are specified in figure C.5.1.	46
3.1.8	Velocity field of the channel ramp under the bridge, where the channel is moved up 1mm in 1, 1.5, 2 and 3mm. The model dimensions are specified in figure C.5.1.	47
3.1.9	Velocity field of different channel widths, 2mm (a) and 2.5mm (b) with 1mm rib at 50g/min. Specified dimensions in figure C.6.1.	48
3.1.10	Velocity field of the five channels in the flow field with a flow rate of 50 g/min per channel. Dimensions specified in figure C.7.1.	49
3.1.11	Velocity field of the channels in the final design at 50g/min per channel. Dimension specified in figure A.6.1	50
3.1.12	Flow distribution in the channels shown in figure 3.1.11, displaying the flow rate in every sub channel as a function of the simulated flow rate.	51
3.1.13	Pressure drop over the different channels in figure 3.1.11 of up to 50g/min per channel.	52
3.1.14	The final flow field reversed with 50g/min per channel from the outlets on the left side.	52
3.1.15	Flow distribution in the channels with a single inlet of up to 250g/min	53
3.2.1	Gasket displacement graph.	55
3.2.2	Compression simulation, 115 [N] per bolt: Gasket displacement	56
3.2.3	Compression simulation, 115N per bolt: Gasket deformation from above.	57

3.2.4	Compression simulation, 115 [N] per bolt: Gasket displacement, x- and y-direction from above.	57
3.2.5	Von Mises stress in two gaskets at 0.6mm compression in (a) and including a pressure of 5Bar on the inside in (b).	58
3.2.6	Compression simulation, 115 [N] per bolt: von Mises stress on the bridges of the three cells.	59
A.1.1	Original end plate dimensions, before decreased length by centre hole . .	
A.1.2	Dimensions of the final end plate design. Top figures: Top and bottom surface, respectively. Bottom left figure: Short surface and Swagelok coupling, Bottom right figure: Dimensions between bolt-, inlet and coupling holes.	
A.2.1	Final dimensions of the bipolar plates.	
A.2.2	Previous design of flow field plates, with gasket groove.	
A.3.1	Dimensions of the unipolar plates with terminal, the rest is similar to the bpp in figure A.2.1	
A.4.1	Dimensions of the bridge and bridge groove.	
A.5.1	Dimensions of the gasket, with either 1 or 1.5mm thickness.	
A.6.1	Dimensions of the inlet(upper) and outlet(lower) side of the final flow field.	
B.1.1	Stainless steel 316, end plate material, datasheet, edited from reference.[74]	
B.2.1	Inconel 625 Alloy, datasheet, edited from reference.[75]	
B.4.1	Helical compression spring data sheet.	
C.2.1	Centre models used to simulate pressure drop and the fluid distribution in the sub channels. The dimensions are in [mm], and the depth is 1mm. . .	
C.4.1	Models used to simulate pressure drop in the inlet geometries, values in [mm]. Pipe is the inlet from the connection to the stack and duct is the channel from the pipe to the sub channels, with and without radius. . . .	
C.5.1	Models for simulating from inlet to channels under the bridge. Figure (a) has a dimension change and (b-e) have a ramp that is moving the channel up 1mm in different lengths.	
C.6.1	Models used to simulate the different channel widths in figure 3.1.9, where (a) has 2mm channels and (b) has 2.5mm channels.	
C.7.1	Model used for simulating the different channels with identical half sides, where the values are in [mm] and the depth of the channels is 1mm. Channel 1 is on the right side and the same goes for sub channel 1.	
C.8.1	Model in COMSOL of the final flow field divided into five separate channels. Each sub channel is referred to as Sub x.x (Sub "channel number" 1-5, starting at the top") and the dimensions is specified in appendix A.6. . .	
C.8.2	Model used to simulate the fluid flow of the flow field with one inlet. . . .	
C.8.3	Model used to simulate the fluid flow in the stack with three flow fields. . .	
C.9.1	Kinematic and dynamic viscosity of water from 0.1-100°C, edited from reference.[76]	
C.9.2	Density of water from 0.1-100°C, edited from reference.[77]	
C.9.3	Density and viscosity of KOH solutions at different temperatures, edited from reference. [78]	

List of Tables

1.1.1	Tabular of HER and OER in acidic and alkaline environment. [7]	2
1.2.1	Advantages and disadvantages of AWE, PEMWE and AEMWE.	7
1.2.2	Status of Alkaline and PEM water electrolysis from 2017, edited from reference.[16]	8
3.1.1	Pressure drop over the flow fields in figure 3.1.1 at 50g/min.	38
3.1.2	Flow rate in the sub channels and pressure drop over the channels simulated at 50g/min, displayed in figure 3.1.2.	41
3.1.3	The effect of the different centre channel design in figure 3.1.2.	41
3.1.4	Flow distribution with different depths for the channel in figure 3.1.3, at 50g/min. Displaying flow rate [g/min] in each sub channel.	43
3.1.5	Flow rate [g/min] in the sub channels and pressure drop [Pa] over the channels in figure 3.1.10, with a flow rate of 50g/min.	49
3.1.6	Flow rate [g/min] in the sub channels and pressure drop [Pa] over the channels from figure 3.1.11, with a flow rate of 50g/min per channel.	50
3.1.7	Flow rate [g/min] in the channels from figure 3.1.15 and pressure drop [Pa] over the flow field.	53
3.1.8	Flow rate [g/min] in the final flow field with one inlet at 250g/min for different solutions.	54
3.1.9	Flow rates for the different flow fields in the stack and pressure drop over the stack.	54
C.1.1	Results from simulations on the flow fields in figure 3.1.1 at 50g/min. Displaying the pressure [Pa] over the flow fields.	
C.2.1	Results from simulations on different centre channels (figure C.2.1) with a flow rate of 50g/min. Displaying the average velocity in the sub channels (cross section: 1.04x1mm) and pressure over the channels.	
C.3.1	Results from the simulations on the centre channel in figure C.2.1b with different depths, ranging from 0.5-1.3mm. Displaying the pressure [Pa] with a flow rate of up to 50g/min (at 1.0).	
C.3.2	Results from the simulations on the centre channel in figure C.2.1b with different depths, ranging from 0.5-1.3mm. Displaying average velocity [m/s] in the sub channels (cross section: Depthx1.04mm) at a flow rate of 50g/min.	
C.4.1	Results from the simulation on different geometries in figure C.4.1 with a length of 1000mm and a flow rate of up to 250g/min (factor=1.0). Displaying the pressure drop [Pa] over the different models.	
C.6.1	Pressure results from simulations of the models in C.6.1 at 50g/min.	
C.7.1	Results from the simulation on the flow field in figure C.7.1, with a flow rate of 50g/min per channel. Displaying average velocity in sub channels (cross section: 1.04x1mm) and pressure over the channels.	

C.8.1	Results from the simulation on the final design of the channels in figure C.8.1. Displaying the average velocity in the sub channels and pressure [Pa] over the channels with a flow rate of up to 50 g/min(Factor=1.0).
C.8.2	Results from simulations of the model in figure C.8.2 at 250g/min, displaying the average velocity [m/s] in the sub channels (cross section:1.04x1.2mm) for different solutions.
C.8.3	Pressure readings related to table C.8.4, which display the pressures over the model in figure C.8.2 with a factor of 250g/min.
C.8.4	Results from the simulation on the model in figure C.8.2 with a flow rate of up to 250g/min (Factor=1.0). Displaying the Average velocity in the sub channels (cross section: 1.04x1.2mm) of model C.8.2.
C.8.5	Results from the simulation of the stack displayed in figure C.8.3. Displaying the average velocity in each sub channel (25 per flow field with a cross section: 1.04x1.2 mm) for the flow fields in the stack, and pressure over the stack.

List of Symbols

ΔH	Change in enthalpy
ΔP	Pressure drop [Pa]
ε	Strain [%]
η	Efficiency
η_a	Activation overpotential [V]
η_c	Concentration overpotential [V]
η_o	Ohmic overpotential [V]
μ	Dynamic viscosity [Pa·s]
ρ	Density [kg/m ³]
σ	Stress [Pa]
σ_d	Deviatoric stress [Pa]
σ_v	Volumetric stress [Pa]
σ_{VM}	von Mises stress [Pa]
\vec{V}	Velocity field [m/s]
A_c	Cross section [m ²]
D_h	Hydraulic diameter [m]
E	Actual cell potential [V]
E°	Standard cell potential [V]
E_{loss}	Cell overpotential [V]
E_y	Young's Modulus [Pa]
F	Faraday constant - 96 485 [C/mol]
f	Friction factor
g	Acceleration of gravity [m ² /s]
h_L	Head loss [m]
I	Applied current density [A/cm ²]
I_0	Exchange current density [A/cm ²]

I_L	Limiting current density [A/cm^2]
K_L	Loss factor
L	Length [m]
M	Molarity [mol/L]
n	Number of mol
P	Pressure [Pa]
P_o	Vetted perimeter [m]
R	Gas constant - 8.314 [J/K· mol]
Re	Reynolds number
T	Temperature [K]
t	Time [s]
V	Velocity [m/s]
ν	Kinematic viscosity [m^2/s]

Acronyms

AEM Anion Exchange Membrane.

AEMWE Anion Exchange Membrane Water Electrolysis.

AWE Alkaline Water Electrolysis.

BPP Bipolar Plate.

CCM Catalyst Coated Membrane.

CCS Catalyst Coated Substrate.

CFD Computational Fluid Dynamics.

CL electrocatalyst layer.

CNC Computer Numerical Control.

GHG Green House Gas.

HER Hydrogen Evolution Reaction.

ICR Interfacial Contact Resistance.

MEA Membrane Electrode Assembly.

MoS Margin of Safety.

NTNU Norwegian University of Science and Technology.

OER Oxygen Evolution Reaction.

PEM Proton Exchange Membrane.

PEMWE Proton Exchange Membrane Water Electrolysis.

PS-DVB polystyrene-divinylbenzene.

PSF polysulfone.

PTL Porous Transport Layer.

SEP Standard Electrode Potential.

ss316 stainless steel 316.

UPP Unipolar Plate.

Glossary

anion Negatively charged atom.

ball milling A grinding method that grinds nanotubes into extremely fine powders..

CAPEX Cost to acquire, maintain and upgrade physical assets.

cation Positively charged atom.

channel Tracks in which the fluid is transported.

concentration gradient Solutes, moving through a solution or gas from an area with a higher number of particles to an area with a lower number of particles..

ductile material Materials which can withstand a high amount of deformation before tearing.

electric potential Minimum voltage needed to move electrons through the circuit.

electrode A solid electric conductor.

electrolyte A substance dissociating into ionic solution, to conduct electrons.

empirical Originating in or based on observation or experience.

flow field Pattern that distributes fluid over a surface.

flow field plate Electron conducting plate with a flow field.

fluid Referring to liquid or gas.

gasket A material shaped to seal between two surfaces.

inlet/outlet Section to/from the flow fields that distributes/collect the fluid.

isotropic Having identical values of a property, in all directions.

laminar Used to describe fluid flow that is controlled and streamlined.

meshing Dividing a model up into small elements, used in simulations.

monomer a molecule that can be bonded to other identical molecules to form a polymer..

O-ring Circular shaped sealing that is used in a groove.

Poisson's ratio Ratio of relative strain normal to the applied load.

polarisation curve Voltage/current density characteristics of a cell, graphical presented.

product A substance created from a chemical reaction.

reactant A substance that create a chemical reaction.

Reynolds number Dimensionless number used to describe the state of fluid flow.

rib Land area between channels.

sintering Increasing the density of a material and forming bridges between particles, by melting..

stack All parts of a water electrolyser assembled.

stamping A method used to press bipolar plates into shape.

strain Ratio of deformation over initial length.

stress Force per unit area.

sub channel Smaller tracks into which the channel is divided.

turbulent Used to describe fluid flow that is chaotic.

ultrasonic homogenization A mechanical process to reduce particles in a liquid so that they become uniformly small and evenly distributed..

viscosity Resistance of a fluid.

wt% Weight percentage, amount of substance in a solutions.

Young's Modulus Material property, stiffness of a material.

Introduction

As technologies advance, and Green House Gas (GHG)-emissions increases, new sustainable solutions has to replace outdated fossil fuel solutions. Both to prevent global warming, and environmental pollution. Hydrogen being the most abundant atom in the universe [1], producing only water and heat by combustion, may play a key role in cutting the GHG-emissions.[2]

Water electrolyzers makes it possible to convert electricity into hydrogen, by using electrons to split water into hydrogen and oxygen. Using renewable energy sources such as wind- or solar power, makes this a zero GHG-emission process.[2] Both wind and solar power are weather dependant, leading to a varying power generation. If the production is higher than the consumption, it will lead to the excess energy being lost. By storing the excess energy and using it when the production is low, the electricity production would be more balanced, efficient, and sustainable. One way of storing the excess energy is to use the electricity to produce hydrogen, with low temperature water electrolysis.

Reversing the electrolytic process with fuel cells, using hydrogen and oxygen to produce water and electricity, make hydrogen applicable for both production- and storage of energy. Fuel cells are proving to be more efficient than conventional fossil fuel engines, reducing fuel consumption with more than 50%, which make them highly applicable in the transport section, among other [3]. This leaves a huge market for the hydrogen technology.

Developing the low temperature water electrolysis is essential for lowering production cost and making the electrolytic process more efficient. Anion Exchange Membrane Water Electrolysis (AEMWE) is a newer technology of low temperature water electrolysis, based on the more mature technologies Proton Exchange Membrane Water Electrolysis (PEMWE) and Alkaline Water Electrolysis (AWE). This combination has the potential of high performance at a low cost, but AEMWE is a developing technology that need more research for stability and power efficiency.[4]

The main objective of this bachelor's thesis is to model and construct a 3 cell AEM electrolyser stack, with an active area of 50cm^2 , and validate its performance under relevant operating conditions. Due to the flow field plates being essential components of the stack assembly, the design and optimisation of the flow fields will be a priority.

Chapter 1

Theory

1.1 Basic principles of water electrolysis

In the process of water electrolysis, water (H_2O), is split into hydrogen gas (H_2) and oxygen gas (O_2), by adding electrons (e^-) to the water. This is done by connecting two electrodes to a DC power supply and placing the two electrodes in the water, creating an electric potential between the electrodes. [5] H_2O is a molecule balanced by two hydrons (H^+) cations and one oxide anion (O^{2-}) anion. Cations and anions are positively and negatively charged atoms, respectively, and are categorised under the common term: ions [6].

When adding e^- to the H_2O , H_2O is used as an electrolyte and dissociates into an ionic solution of hydrons (H^+) and hydroxide (OH^-) [7]. Water as a neutral medium is a very weak electrolyte because of its very low concentration of ions, making it difficult to conduct e^- [8]. A solution to this is to dissolve substances of higher ion concentration in water, leading to a more efficient electrolysis and conduction of e^- .

The electrodes are called the cathode and anode, and have different reactions that occur. The cathode electrode is the electrode which distributes electrons to the electrolyte, making its polarity negative. Because of its negative polarity, it attracts H^+ cations to absorb e^- . This makes the Hydrogen Evolution Reaction (HER) occur - the production of H_2 . [7] When the H^+ absorb e^- from the cathode, their polarity gets reduced, leading to a reduction of their oxidation state [9]. In this case H^+ is the reactant, reacting with the e^- . H_2 is the product, produced from the reaction. Oxygen production occurs at the anode, called Oxygen Evolution Reaction (OER). The anode has a positive polarity, attracting e^- carrying anions, and making them divide by absorbing the e^- . This leads to an increase in the molecules oxidation state, and is called oxidation. [4] The HER and OER is presented in tabular 1.1.1.

Table 1.1.1: Tabular of HER and OER in acidic and alkaline environment. [7]

Type of reaction	Acidic environment	Alkaline environment
Hydrogen Evolution Reaction	$4H^+ + 4e^- \rightleftharpoons 2H_2$	$4H_2O + 4e^- \rightleftharpoons 2H_2 + 4OH^-$
Oxygen Evolution Reaction	$2H_2O \rightleftharpoons O_2 + 4H^+ + 4e^-$	$4OH^- \rightleftharpoons 2H_2O + 2O_2 + 4e^-$

1.1.1 Cell potential

To convert the electrical energy to chemical energy, a certain amount of voltage has to be applied. This is called the cell potential, and this is the potential of voltage between the anode and cathode. The potential of each electrode varies by the polarity of the water solution. If the solution contains a majority of cations, the solution becomes acidic, leading to a positively charge increase on both electrodes. If it is a majority of anions, it becomes alkaline, and the charge on each electrode decreases.[10] Figure 1.1.1 presents the Standard Electrode Potential (SEP) (1 Molar, 25 °C, and 1 atm) of the anode and cathode, at different pH conditions.

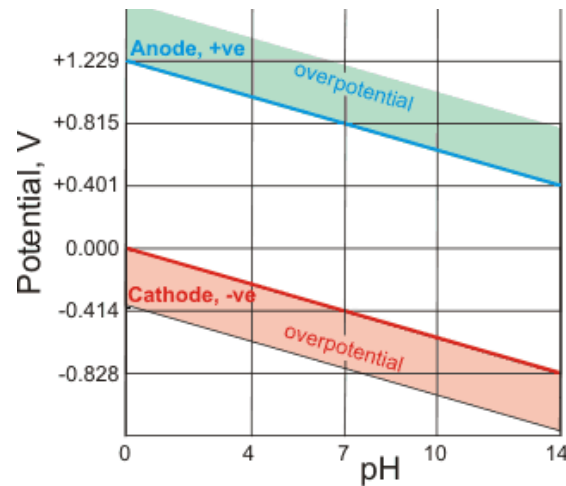
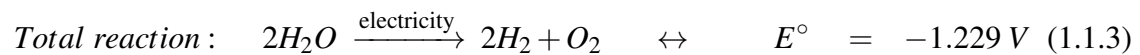
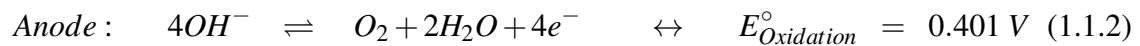


Figure 1.1.1: Cell potential at different pH at SEP [10]

The standard cell potential of alkaline water electrolysis is shown in equation 1.1.1, 1.1.2 and 1.1.3 [4].



1.1.2 Actual cell potential

The standard cell potential E° is theoretical, and in practice there will be losses in the conversion process, and transfer of ions between the electrodes. These losses are called overpotentials η , and makes the energy conversion of the electrolysis demand a higher applied voltage. E_{loss} is introduced in equation 1.1.4[11], where E_{cell} is the actual cell potential, and expressed in equation 1.1.5, where E_{cell} is the actual cell potential.

$$E_{\text{cell}} = E^{\circ} + \Sigma E_{\text{loss}} \quad (1.1.4)$$

$$\Sigma E_{loss} = \eta_a + \eta_o + \eta_c \quad (1.1.5)$$

There are three main categories for the overpotentials, ohmic- η_o , activation- η_a and concentration overpotential η_c [11].

Activation overpotential

The activation of the electrolytic process demands a higher amount of energy than when operating. This is called the activation overpotential and is a barrier of the e^- transfer at the electrode interfaces. The barrier of the e^- transfer comprises preceding- and following surface conversions, adsorption and desorption to- and from the electrode interface, respectively, etc.[11] η_a is expressed by equation 1.1.6[11].

$$\eta_a = \frac{RT}{\alpha nF} \ln i_0 - \frac{RT}{\alpha nF} \ln i = a + b \ln i \quad (1.1.6)$$

Equation 1.1.6 is the well known Tafel equation, derived by the swizz chemist Julius Tafel from the Butler-Volmer equation. $a = \frac{RT}{\alpha nF} \ln i_0$ represents the overpotential, where i_0 is the exchange current of the cell, α is the transfer coefficient and F is the Faraday constant. $b = \frac{RT}{\alpha nF}$ is the Tafel slope, describing the change rate of the activation overpotential at a certain current density i . [11] The Tafel equation is presented in a Tafel plot, in figure 1.1.2

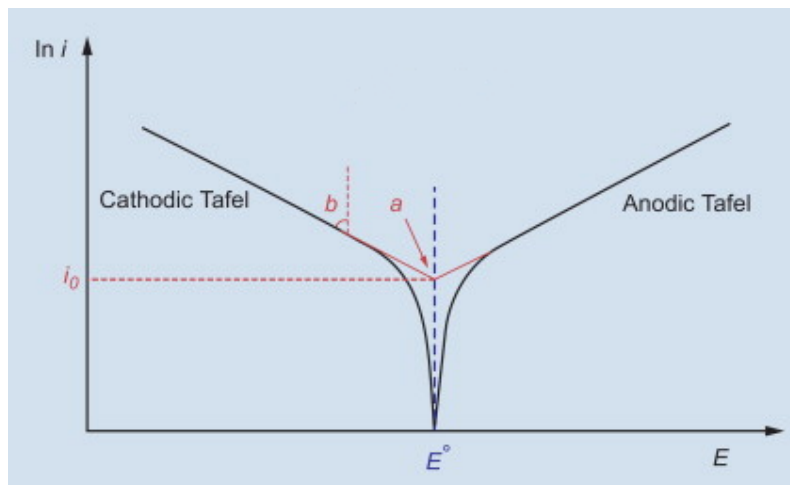


Figure 1.1.2: An illustration of the Tafel plot and the a and b parameters, edited from reference[11]

Ohmic overpotential

The ohmic overpotential is the internal resistance R_{ohmic} of an electrolytic cell, multiplied by the current density I of the cell. All the components of an electrolytic cell has a given resistance characteristic to charge flow, affecting the e^- and ion conduction. η_o include ionic- R_{ion} , electronic- R_{e^-} and contact resistance $R_{contact}$ of the electrolyte and cell assembly. This involves current through wiring, connections, contacts and electrodes, and ion conduction through the membrane (further explained in the following sections) and electrolyte.[11] η_o is defined by equation 1.1.7[11].

$$\eta_o = I \cdot R_{ohmic} = I(R_{e^-} + R_{ion} + R_{contact}) \quad (1.1.7)$$

Equation 1.1.7 states that η_o changes linearly with the current density of the cell. Studies [12] show that the majority of the ohmic overpotential in AEMWE is caused by the conduction of ions through the membrane.

Concentration overpotential

The higher the current of e^- is through the cell, the more reactants are consumed at the electrodes, which further increases the concentration gradient of reactants and products at the electrode surfaces.[11] If the reaction occur more rapid than the mass transfer of the electrolyte, it will lead to a depletion of reactants, or an accumulation of products at the electrode surface. This cause a limiting current density i_0 , which is the maximal current density of the electrolytic cell.[13] The concentration overpotential η_C is a result of the concentration gradient created, presented in equation 1.1.8[13], where R is the gas constant and T is the temperature in Kelvin.

$$\eta_c = \frac{RT}{nF} \ln\left(\frac{i_L}{i_L - i}\right) \quad (1.1.8)$$

Polarisation curve

The applied cell voltage and current density characteristics of a cell is often used as an analogy of its efficiency. These are called polarisation curves and illustrates the total applied cell voltage versus the current density. Figure 1.1.3 (a) presents the ohmic overpotential linear curve, and the activation- and concentration overpotentials combined as the overpotentials of the cathode and anode. The limited mass transportation, making the cell reach its limiting current, will eventually lead to an asymptote in the polarisation curve. This is usually where the curve ends. The overpotentials can also be summed to a curve showing the operating voltage versus the current density of the cell, as shown in figure 1.1.3 (b).

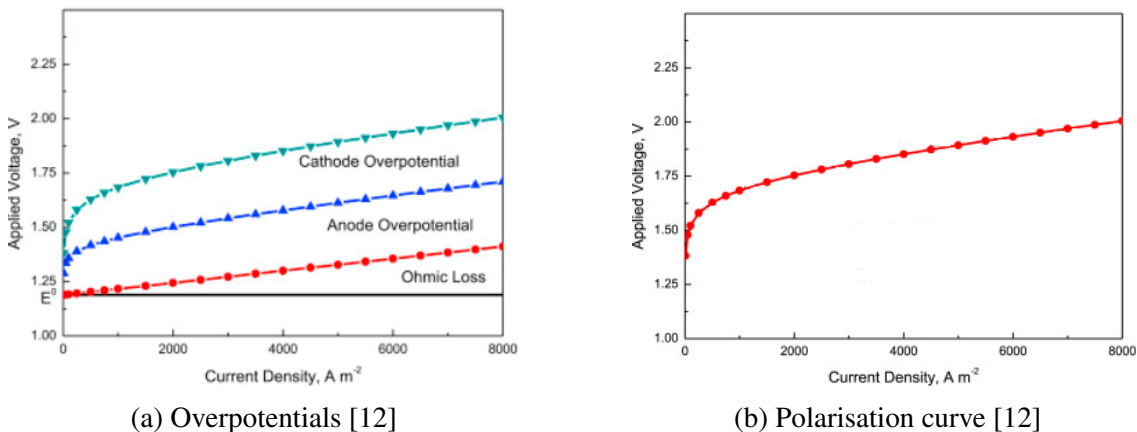


Figure 1.1.3: Polarisation curves of a typical anion-exchange membrane water electrolyser

Studies [12] show that the total overpotential in a typical AEMWE is majorly attributed by the activation overpotential of the HER and OER occurring at the cathode and anode.

Efficiency

Not to be confused, the symbol η is the symbol of efficiency, not the overpotentials. The efficiency of a water electrolyser describes the amount of energy lost (E_{loss}) in the cell, relative to how much energy is applied to the cell (E_{cell}).[12] This is compared to 100% which would be the optimal electrolytic efficiency, as seen in equation 1.1.9[12].

$$\eta = 1 - \frac{E_{loss}}{E_{cell}} \quad (1.1.9)$$

The efficiency of a typical AEMWE is shown in figure 1.1.4, showing the efficiency decreasing as the current density increase. Even though the efficiency decrease, the production of hydrogen will increase, as the current density increase. The efficiency of the electrolyser describes how much of the energy applied to the electrolytic cell that gets "lost" during transfer and conversion in the cell.[12]

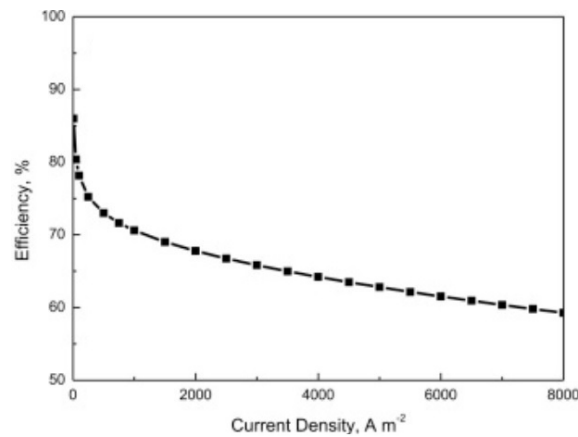


Figure 1.1.4: Efficiency of a typical anion-exchange water electrolyser [12]

1.2 Low temperature water electrolysis

Conventional electrolysis benefits from the concepts HER and OER, and facilitates the environments for the favourable reactions. The electrolysis method is defined by the operating environment and the components that is used to enhance the reactions. Currently, there are three low temperature water electrolysis technologies, AWE, PEMWE and AEMWE [14]. Each have their own advantages and disadvantages, listed in table 1.2.1, making them suitable for different applications.

1.2.1 Mature water electrolysis technologies

In AWE it is common to use a solution of water and up to 40 weight percentage (wt%) of potassium hydroxide- (KOH) or sodium hydroxide (NaOH) as the electrolyte. This is to favour the formation of OH^- . The electrodes are separated by a diaphragm, permeable to OH^- anions.[15] This is illustrated in figure 1.2.1.

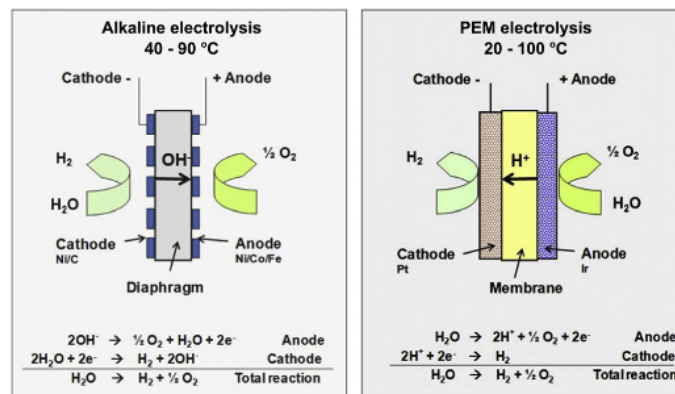
AWE is a mature technology with low investment and maintenance cost, while the drawbacks are the operating range and performance. The load range is limited to around 20% or more, where there may be cross contamination between the product gasses at lower

Table 1.2.1: Advantages and disadvantages of AWE, PEMWE and AEMWE.

AWE	PEMWE	AEMWE
Advantages		
Mature technology	Mature technology	Non noble catalyst
Non noble catalyst	Higher performance	Non corrosive electrolyte
Long term stability	Higher voltage efficiency	Compact cell design
Low CAPEX	Rapid system response	Low CAPEX
Megawatt range	Compact cell design	High operating pressure
	High load dynamics	
	Megawatt range	
Disadvantages		
Lower current density	Higher CAPEX	Not mature
Limited load dynamic	Noble metal catalyst	Membrane degradation
Corrosive liquid electrolyte		
Low operating pressure		

loads, which could result in a flammable mixture.[16] Since there are high ohmic losses in the electrolyte and diaphragm, the operating current density is relatively low [17].

In PEMWE, the electrodes are in direct contact with the membrane, forming a Membrane Electrode Assembly (MEA) [15]. Water is added to the anode side and H^+ is transported through the membrane to form hydrogen at the cathode side, as illustrated in figure 1.2.1. PEMWE has higher costs because it requires noble metals for catalysts. This is due to the acidic environment created by the proton exchange membrane.[16] Compared to the porous diaphragm in AWE, the membrane in PEMWE is a solid polymer electrolyte, which have improved performance, lower crossover of gasses and the ability to operate with different pressure on each side [18].

**Figure 1.2.1: Operating principles of Alkaline and PEM water electrolysis.[17]**

1.2.2 AEM Water electrolysis

AEMWE is a combination of PEMWE and AWE, where the MEA also consists of a solid polymer electrolyte membrane, but instead of the proton conductive ability of the Proton Exchange Membrane (PEM), the Anion Exchange Membrane (AEM) is able to conduct

OH^- [18]. In AEMWE, water is added to the cathode side, where water is reduced to form hydrogen, while OH^- is transported through the MEA to form oxygen and water at the anode side [19]. This is shown in the reactions in equation 1.1.1-1.1.3.

The OH^- conductivity over the AEM is important for the performance of the AEMWE. Since the water has a relatively low conductivity of OH^- , a solution of KOH is usually applied to both the anode- and cathode side to increase the ionic conductivity of the cell.[20] Instead of a high concentration of KOH like in AWE, AEMWE usually operates in 0.1-1M KOH [18, 20, 21], which is approximately 0.5-5 wt%. By operating in an alkaline environment, non-noble metals can be used for the OER catalyst in AEMWE, which can lower the cost compared to PEMWE [22].

1.2.3 Status of water electrolysis technologies

AWE and PEMWE are both commercially available multi-manufacturer technologies, where AWE has been around for over a century and PEMWE has come in the last decades. The difference between them is that AWE was built for stationary operations and is adapted to the modern requirement for flexible operations, while PEMWE has been more developed to fit the requirements for flexible operations.[16] Table 1.2.2 lists the status of AWE and PEMWE from 2017.

Table 1.2.2: Status of Alkaline and PEM water electrolysis from 2017, edited from reference.[16]

	AWE	PEMWE
Operating parameters		
Cell temperature [$^{\circ}\text{C}$]	60–90	50–80
Typical pressure [bar]	10–30	20–50
Current density [A/cm^2]	0.25-0.45	1.0-2.0
Flexibility		
Load flexibility (% of nominal load)	20-100	0-100
Cold start-up time	1-2h	5-10min
Warm start-up time	1-5min	<10s
Efficiency		
Nominal stack efficiency (LHV)	63-71%	60-68%
specific energy consumption [kWh/Nm^3]	4.2-4.8	4.4-5.0
Available capacity		
Max. nominal power per stack [MW]	6	2
H_2 production per stack [Nm^3/h]	1400	400
Cell area (m^2)	<3.6	<0.13
Durability		
Life time [kh]	55-120	60-100
Efficiency degradation per year	0.25-1.5%	0.5-2.5%
Economic parameter		
Investment costs [$\text{€}/\text{kW}$]	800-1500	1400-2100
Maintenance costs (% of investmen cost per year)	2-3	3-5

In recent years, AEMWE has become an alternative to AWE and PEMWE, with at least

one manufacturer, Enapter[23]. For AEMWE to be competitive, it must outperform similar existing technologies, either by price, durability or performance.

Several studies have looked at ways of improving the performance of AEMWE. By using non-noble metals for the HER catalyst, a current density of $1\text{A}/\text{cm}^2$ was obtained at 1.9V [18], while another study achieved $1.5\text{A}/\text{cm}^2$ at 1.9V using noble metals for catalysts [20]. In a more recent study, even higher performances were achieved, as shown in figure 1.2.2, where $2.0\text{A}/\text{cm}^2$ was obtained at $1.85\text{-}1.9\text{V}$, with non-noble metals for the OER catalyst [21].

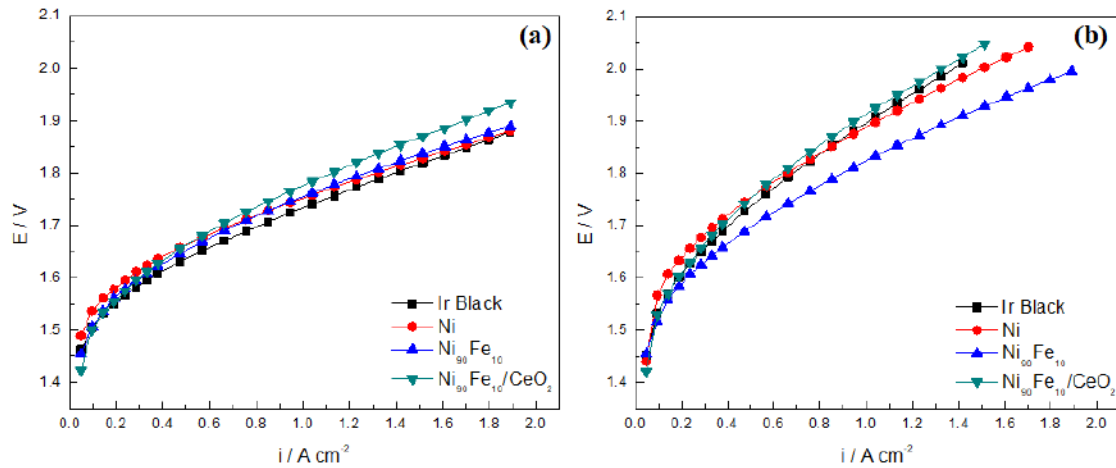
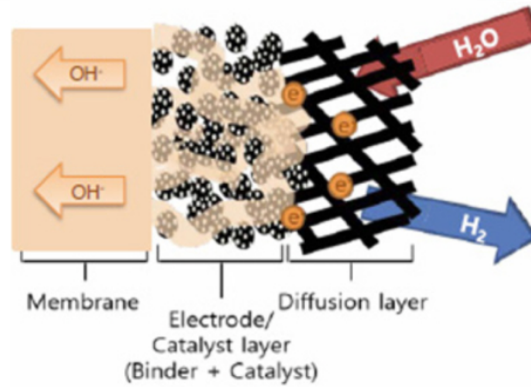


Figure 1.2.2: Polarisation curves of AEMWE with different catalyst for OER and Pt/c for HER, in 1M KOH (a) and 0.1M KOH(b) at 50°C , edited from reference.[21]

1.3 Advanced technology

To make the water electrolysis reaction happen more efficient, special components and materials are developed. The MEA illustrated in figure 1.3.1 consists of three essential components of today's water electrolyzers. The polymeric Anion Exchange Membrane, and the catalyst and diffusion layer, located on both sides of the membrane.[22]



Membrane electrode assembly

Figure 1.3.1: MEA, edited from reference [22]

1.3.1 Polymeric Anion Exchange Membrane

The polymeric AEM is used as a semi permeable barrier between the reactions occurring on the cathode and anode. It is impermeable to e⁻ and other reactants or products, only conducting OH⁻. Creating the AEM, monomers are bonded together, creating a semi permeable polymeric gel with fixed ionic charge. Quarternary amines are used as cation-exchange carrier groups, based on polystyrene-divinylbenzene (PS-DVB) polymer or polysulfone (PSF).[24, 4] The ionic conductivity of the AEM is controlled by the number of cationic groups in the polymer chain backbone, and this is essential for the conduction of OH⁻. [22]

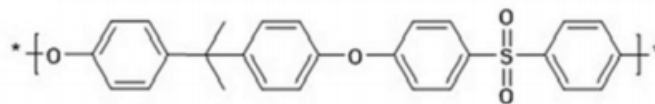


Figure 1.3.2: Example of the chemical structure of a homogenous polysulfone AEM [22]

A high quality AEM will have a low crossover of fuel and products, leading to a higher hydroxide conduction and current density.[4] To have a long term operating AEM, it is also important that the properties of the membrane is stable, during operation, increases in temperature and more alkaline environment. [22]

1.3.2 Porous Transport Layer

When water flow through the cell, gases evolve at the catalyst layer. As the name Porous Transport Layer (PTL) implies, it is a porous layer made of sintered metal, e.g. Ni,

stainless steel or Ti, used to transport species in and out of the catalyst layer. The PTL is permeable to water, product gases, in addition to conduction of electrons, heat, and mechanical supporting of the MEA.[25] First, the PTL conducts the water to the electrocatalyst, and then returning the evolved gas back to the water stream, as showed in figure 1.3.3 (a) and (b), respectively.

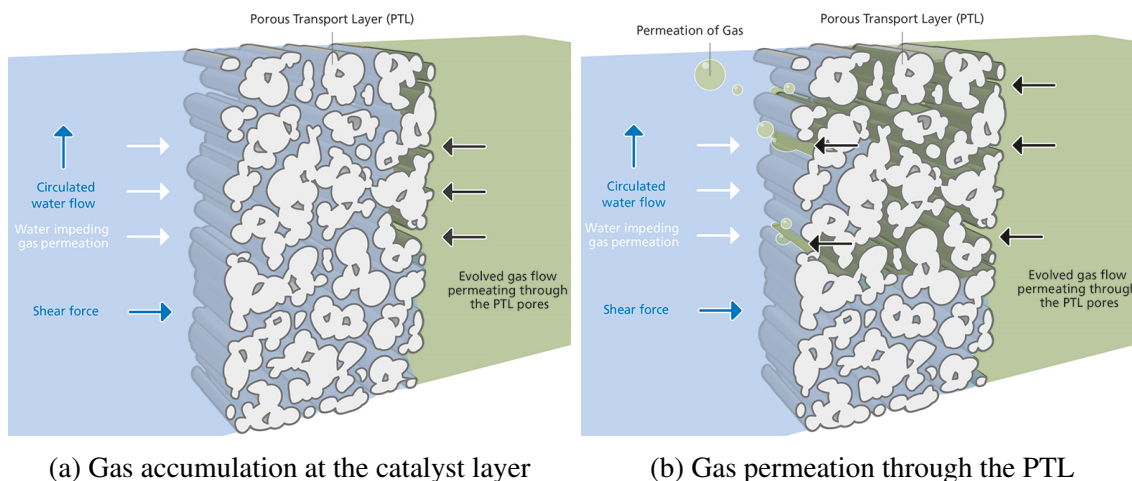


Figure 1.3.3: The conduction of water and evolved gas in the Porous Transport Layer [26]

There are limited information about PTL material for AEMWE, but there has been some testing on titanium (Ti)-based materials from PEMWE [25, 27]. Microstructural properties of the PTL, such as the pore size, thickness, porosity and morphology, are some of the properties influencing the performance of the electrolyser. [25]

1.3.3 Electrocatalyst layer

The electrocatalyst layer (CL) is a nanoscale porous layer of metal, reducing the overpotential for the OER and HER.[28, 22] The layer is a blend of metal catalyst, ionomer and solvents blended together by ultrasonic homogenization, or by a grinding method called ball milling. [28] The alkaline environment in AEMWE make the OER less demanding than for the acidic environment in PEMWE, which make it possible to use non noble metals as electrocatalysts.[22] For the OER, presently, IrO_2 , Ni, Ni-Fe alloys, graphene, $\text{Pb}_2\text{Ru}_2\text{O}_{6.5}$ and $\text{Cu}_{0.7}\text{CO}_{2.3}\text{O}_4$ are used, and Pt black, CuCoO_x , Ni-Mo, Ni/ CeO_2 - La_2O_3 /C, Ni and graphene for the HER electrocatalyst.[4] Currently, there are developments for reducing the loading of the metal catalyst, and increase efficiency.[28] There is still limited results from AEMWE single cell tests, making it hard to prove the efficiency of current electrocatalyst.[22]

The CL are often attached to either the AEM or PTL, as a coated layer. This is usually done by combining, or using one of two coating methods, called the Catalyst Coated Substrate (CCS)- and Catalyst Coated Membrane (CCM) method.[29] The two methods are illustrated in figure 1.3.4.

The CCS fabrication is usually done by depositing the CL directly on top of the PTL, by for example sintering the CL to the PTL, also called hot-pressing. The membrane material often does not withstand temperatures above 70°C , which means that the CCM fabrication uses other methods for coating, such as using a spray or a doctor blade. [29]

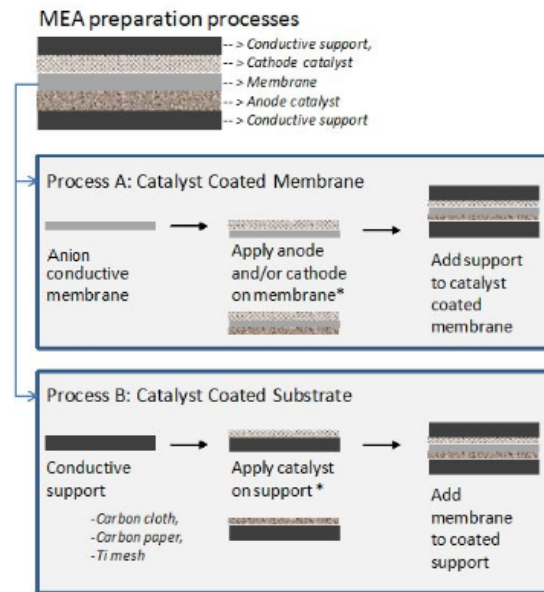


Figure 1.3.4: CCS and CCM processes, edited from reference [30]

The CL makes a big impact on overcoming the activation barrier of the electrolytic process, and reducing the activation overpotential described in previous sections.[31] An analogy of the CL’s role in reducing the activation overpotential is illustrated in figure 1.3.5. ΔH is the change in enthalpy, before and after activation.

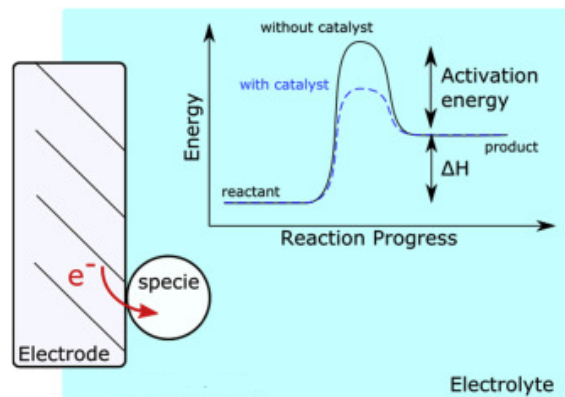


Figure 1.3.5: The electrocatalysts role in reducing the activation overpotential [31]

1.4 Stack assembly

In modern water electrolysis, the MEA is placed between electron conducting plates and assembled into a stack to make a cell. The electrolyte is pumped through channels in the plates to deliver reactants to the active cell area while simultaneously removing products. By repeating the layers of MEA and plates, several cells can be combined in series in a single stack, as illustrated in figure 1.4.1.

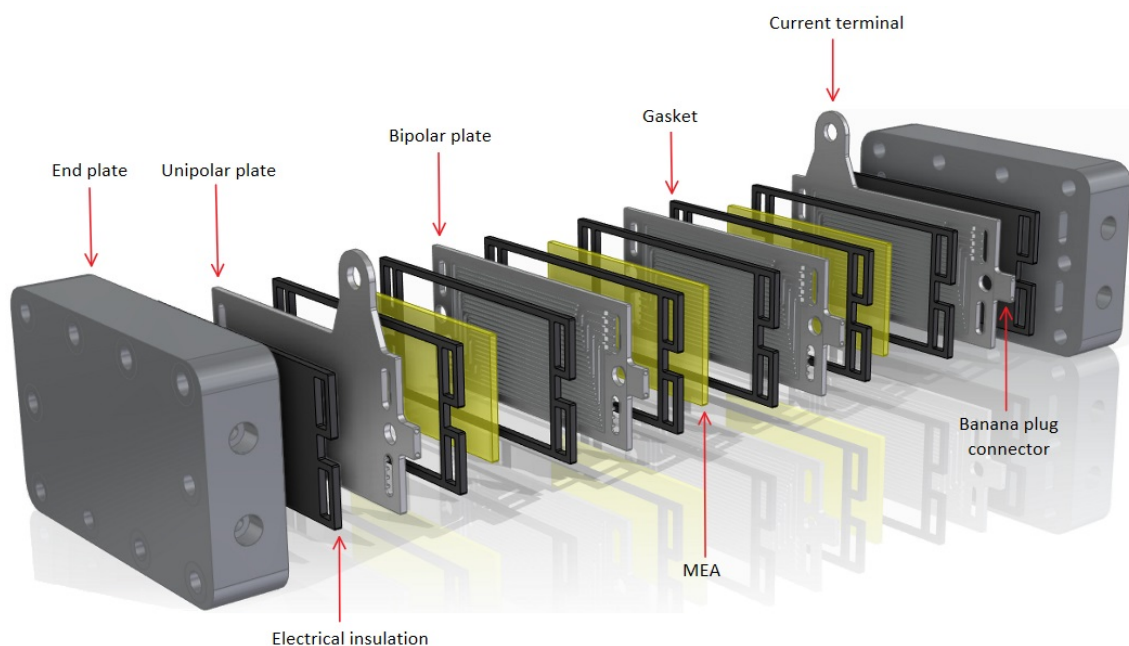


Figure 1.4.1: Components of the AEMWE stack

1.4.1 Flow field plates

The plates in contact with the MEA is referred to as flow field plates. These are further categorised as Bipolar Plate (BPP) or Unipolar Plate (UPP), depending on how many cells they are in contact with.

BPPs are used to combine the cells in series, making one side the anode plate and the other side the cathode plate. Each side of the plate has a flow field to evenly distribute the fluid across the active cell area, this is explained in more detail in section 1.5. The BPP also has the function of transferring electrons between cells, separating the reactants from each other and to physically support the MEA.[32] This requires a material that is electrically conductive, impermeable to reactants and strong enough to withstand the compression and pressure forces.

Depending on the water electrolysis method, bipolar plates could be the most expensive part in a stack. In PEMWE the bipolar plates is usually made of titanium, which could account for half of the stack cost.[14] By using AEMWE, the bipolar plates can be made of a lower cost material like stainless steel instead [29]. Another cost reduction of making the bipolar plates is to use a stamping method. This presses the plates into shape, instead of milling them with Computer Numerical Control (CNC). The stamping method

will both save time during mass producing and make it possible to make thinner plates, which reduces weight and space.[33]

At each end of the connecting cells there is a UPP. This is identical to the BPP, with the exception that there is only a flow field on one side, which make the plate either anode or cathode. The UPP is either directly connected to the DC power supply with a terminal connector, and function as a current collector, or is in contact with a separate current collector plate that is connected.

1.4.2 Gasket

Between each flow field plate and MEA, there is a gasket that seal to create a fluid tight connection. This is to prevent the reactants and products from each side to get in contact or to leak out of the cell. Gaskets are used between two flat surfaces and need to be compressed enough to create a pressure tight seal. When compressed, the gasket will fill the gap between the surfaces and should therefore be made of a material that is easily deformed.[34] The material must also handle the operating environment, which depends on the fluids corrosive nature, pressure and temperature [35].

It is also possible to use a O-rings to seal. O-rings has a circular shape and is used in a groove that is cut into one of the surfaces. When pressure is applied on the inside of the O-ring, it will be pushed against the outer groove wall and create a seal between the contacting surfaces.[36]

1.4.3 End plate

The stack is compressed between two end plates to seal the cells and make electrical contact, while creating fluid passage to and from the flow fields [37]. To have the end plate electrical isolated from the stack, a low conductive material can be used between the end plate and current collector.

It is important to have a uniform compression of the stack and therefore the end plates should be made from a strong and rigid material [37]. Bolts are evenly distributed along the edge of the plates and are used to clamp the stack together. If the clamping force is unevenly distributed on the end plates, the pressure distribution will vary and lead to less contacting points in the active cell area, which will lower the performance [38]. Improper pressure distribution can also cause leakage over the seal.

1.5 Flow field theory

In water electrolysis, the products formed in the cell must be removed so that new reactants can create more product. This is done by creating flow fields that transport the reactants to the cell, while simultaneously removing products. The flow field is usually milled or formed into the flow field plates as a pattern, which consist of channels and ribs to distribute reactants evenly to the electrodes [32]. Channels are the tracks in the plate, while the ribs are the shoulder separating the channels to create a pattern, as illustrated in figure 1.5.1.

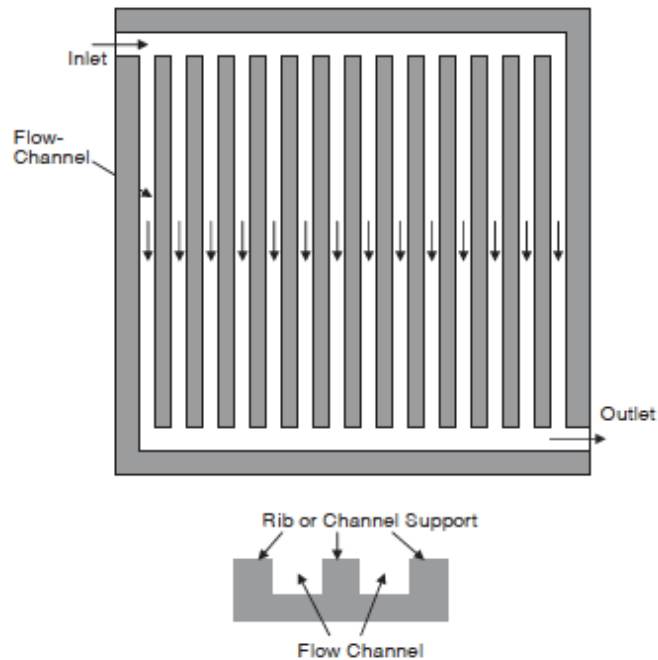


Figure 1.5.1: Straight flow field pattern illustrating channel and ribs.[32]

1.5.1 Channels

In the stack, the flow field is in contact with the PTL and the fluid flows internally through the channels. The shape, size and path of the channels affect the fluid flow and pressure drop, where a uniform pressure drop is necessary to evenly distribute the reactants across the active cell area.[39]

Pressure drop and Head loss

When fluid is transported through a system, it requires a certain pressure from a pump to maintain constant flow. This pressure must overcome the friction loss in the system, also referred to as pressure drop, which can be divided into major and minor losses. Major losses are caused by the friction between wall surfaces and the fluid, depending on the roughness of the wall and the fluid viscosity. Viscosity is the friction in a fluid that opposes the layers from flowing at different velocities relative to each other. The viscosity changes with temperature and pressure, where a fluid that have low viscosity will flow more easily.[40] Minor losses are due to directional and dimensional changes, which comes from entrances, bends and other disturbances that redirect the fluid flow. In smaller systems with a lot of bends, the minor losses can be greater than the major losses. The total pressure drop ΔP can be calculated as head loss h_L from equation 1.5.1, which is the pressure drop divided by the fluid density ρ and the acceleration of gravity g , $h_L = \frac{\Delta P}{\rho g}$. [41]

$$h_{L,total} = \underbrace{\left(f \frac{L}{D_h}\right)}_a + \underbrace{\left(\sum K_L\right)}_b \frac{V_{avg}^2}{2g} \quad (1.5.1)$$

There are two parts in equation 1.5.1, where both are dependent on the average velocity V_{avg} and the acceleration of gravity g . The first part (a) is the major losses, where L is the

length of the pipe, D_h is the hydraulic diameter calculated from equation 1.5.3 and f is the friction factor. The friction factor is found in tables obtained from practical experiments and depends on the geometry and Reynolds number. The second part (b) is the minor losses, where the loss factor K_L is found in tables obtained from practical experiments. Since factors are obtained from experimental results, an error of ten percent or more should be taken into the calculation. [41]

Laminar and Turbulent flow

Fluid flow behaves in three ways, it flows laminar, turbulent or in transition between the two. When the flow is laminar, the fluid is transported in a controlled streamlined manner, this occurs at lower velocities or for highly viscous fluids in smaller pipes. At higher velocities, the fluid flow becomes turbulent with fluctuating velocity and disturbed motion, giving a more chaotic flow that increases the friction from the channel surface. [41]

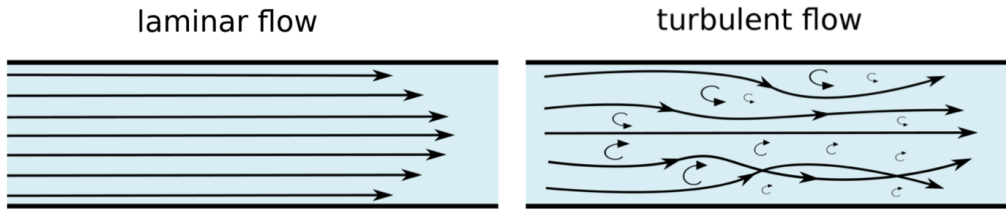


Figure 1.5.2: Laminar and turbulent flow, edited from reference. [42]

Reynolds number

Whether the flow is laminar or turbulent (illustrated in figure 1.5.2), in a given channel at constant velocity, can be estimated from Reynolds number. Reynolds number is the relationship between kinetic energy and the internal viscous forces of the liquid, which can be calculated from equation 1.5.2.[43] Under practical conditions, the fluid flow in circular pipes is laminar for Reynolds number up to 2300, in transition up to 4000, and then turbulent. This estimate will be affected of the roughness and interference through the pipe. [41]

$$Re = \frac{V_{avg} D_h}{\nu} \quad (1.5.2)$$

V_{avg} is the average velocity of the cross section of the channel, ν is the kinematic viscosity that depends on the fluid and temperature and D_h is the hydraulic diameter. The hydraulic diameter is found with equation 1.5.3, where A_c is the cross section and P_o is the wetted perimeter.[41]

$$D_h = \frac{4A_c}{P_o} \quad (1.5.3)$$

1.5.2 Ribs

Ribs are the part of the flow field that is in direct contact with the PTL, giving physical support and electrical contact to the MEA. The flow field is designed to fit the active cell

area, which limits the area of ribs and channels. This causes the ribs and the channels to influence each other, so that changing the width of the ribs will affect the width of the channels.

The channel width to rib ratio is important to optimise the flow field for a better performance. If the ribs are narrower, the electrical contact resistance increases, while wider ribs lead to narrower channels and therefore increased pressure drop [44]. For the electrical contact with PTL, a ratio of rib to total area of the flow field of less than 0.45 will have significant increase of ohmic losses, while a ratio above 0.57 will have insignificant effect of lowering the ohmic losses [39].

When the stack is assembled, the MEA is compressed between the flow field of the anode and cathode side. If the compression force on the stack is low, the contact resistance between the ribs and PTL will increase. This is due to the surface roughness of the contacting materials, where only the tips of the unevenness will have contact. On the other hand, with too much compression force, the ribs could damage the MEA and resulting in a leakage over the membrane.[45] For an uniform compression, the contacting areas should be evenly distributed and overlap with the other flow field. If the anode and cathode plates are not aligned properly, local stress could occur and damage cell components.[32]

1.5.3 Flow field pattern

Both channels and ribs are important for the performance, where the width of the channels affect the pressure drop and the width of the channels and ribs affect the current density [44]. This should be considered when design a flow field pattern, to optimise the cell performance.

Each design has pros and cons that suits different applications. Figure 1.5.3 illustrates two common flow fields with a single serpentine channel and straight parallel channels. For fuel cells, straight parallel channels have lower pressure drop where flow tends to follow the path with least resistance, while in serpentine pattern the flow is in one or multiple longer channels that have higher pressure drop but has distribution across the entire flow field.[32]

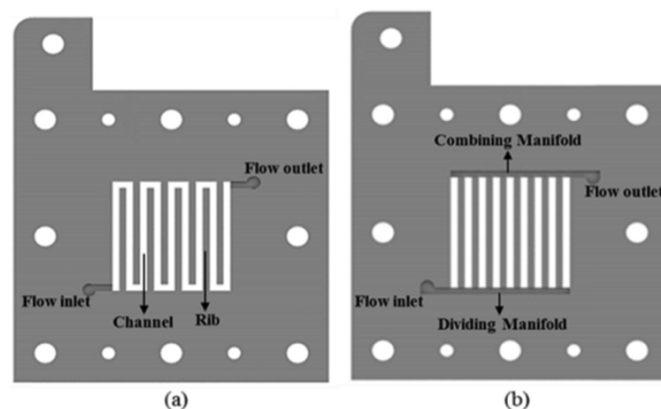


Figure 1.5.3: Serpentine flow field (a) and straight flow field (b).[46]

In water electrolysis, there are a two-phase flow consisting of liquid flow with gas bubbles. When gas bubbles are merged, they are combined into bigger bubbles that is referred

to as slugs, illustrated in figure 1.5.4. These slugs will hinder water to be transported to the catalyst layer and thus lower the cell performance. Slugs increase with current density and the channel length, while an increase in flow rate delays forming of slugs depending on the cell temperature [46].

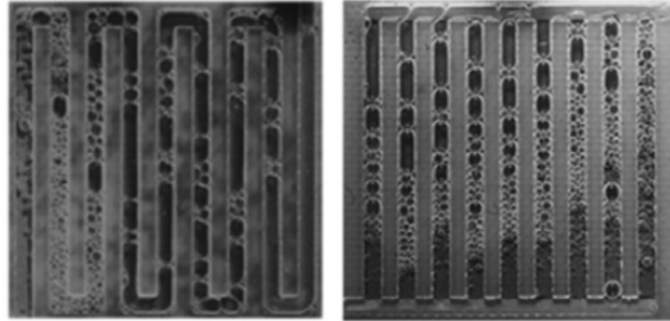


Figure 1.5.4: Slugs forming in PEMWE at 2[A/cm²] in the flow fields from figure 1.5.3, edited from reference. [46]

1.5.4 The Navier-Stokes equations

The Navier-Stokes equation is basically the momentum equation for fluids and is solved in combination with the continuity equation. Combined, these represent the conservation of momentum and the conservation of mass. Depending on the problem, the equations can be simplified or expanded according to the fluid that is analysed.[47] For incompressible fluids with constant viscosity, the Navier-Stokes equation and the continuity equation can be solved with equation 1.5.4 and 1.5.5, respectively.[48]

$$\underbrace{\rho \frac{D\vec{V}}{Dt}}_1 = \underbrace{-\vec{\nabla}P}_2 + \underbrace{\rho\vec{g}}_3 + \underbrace{\mu\nabla^2\vec{u}}_4 \quad (1.5.4)$$

The Navier-Stokes equation is written as Newton's second law, $m\vec{a} = \sum \vec{F}$. In (1), the mass is represented by the density ρ and the acceleration as the change in the velocity field \vec{V} with respect to time t . The other half represents the forces, where (2) is the surface force with pressure p , (3) is the gravitational force and (4) is the viscous force with the dynamic viscosity μ . [49]

$$\vec{\nabla}\vec{V} = 0 \quad (1.5.5)$$

When the boundary conditions are set for a specified geometry, equation 1.5.4 and 1.5.5 can be used to calculate the velocity and pressure fields of the flow [48].

1.6 Material Properties

1.6.1 Young's Modulus

Young's Modulus is the stiffness of a material and is the ratio between stress and strain.[50] This can be found by performing a tensile test on the material, where the material is stretched along the length, and the stress is plotted as a function of the strain. Figure 1.6.1

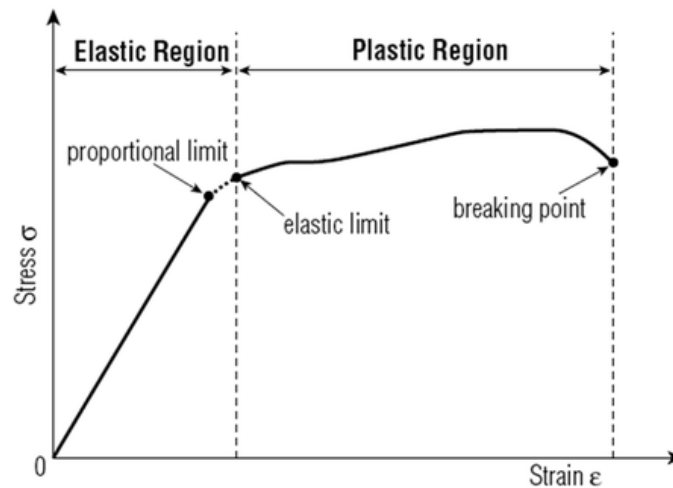


Figure 1.6.1: Graph illustrating a tensile test. [51]

is an example of how a material will behave in a tensile test, with force per unit area as stress in the y-axis and the extension as strain in the x-axis. The plot is divided into the elastic- and the plastic region. The plastic region has a linear ratio of stress and strain, where the material will go back to the original state when the stress is released. If the material is stretched into the plastic region, it will deform and be permanently damaged, where further extension will break the material. Young's Modulus E_y can be found in the elastic region as the gradient of the slope from equation 1.6.1, where a higher value means a stiffer material. In the equation, σ is stress and ϵ is the strain that are the extended length divided by the original length. [52]

$$E_y = \frac{\sigma}{\epsilon} \quad (1.6.1)$$

1.6.2 Poisson's ratio

Poisson's ratio is a coefficient that describes materials ability to change in the directions that is perpendicular to where it is compressed or stretched, illustrated in figure 1.6.2.[53] For isotropic materials in the elastic region, the coefficient has a theoretical value between -1 and 1/2, where most common materials have a value between zero and 1/2.[54] With a Poisson's ratio of 1/2 the material will have a constant volume, which means that a compression in one direction is fully transferred to the expansion in the other directions, while stretching has equal but opposite effect. Rubber is a material close to this limit, while cork material has a value close to zero. When Poisson's ratio is zero, there is no change perpendicular to the compression or stretching, which is useful when inserting a cork into a wine bottle. On the other side of the scale, materials with negative values will increase perpendicular to the compression or stretching and decrease when compressed, which is mostly engineered materials.[55]

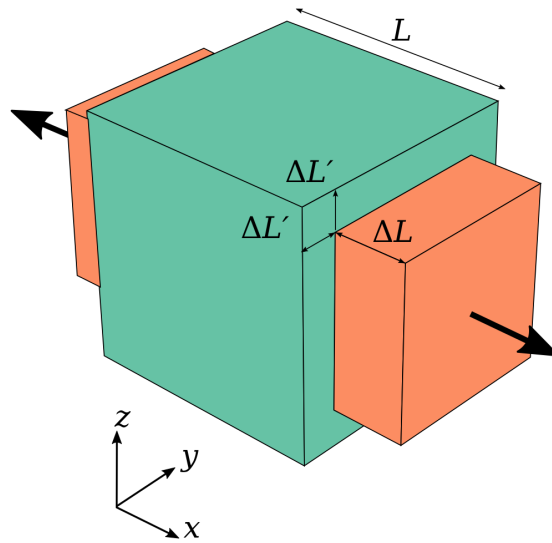


Figure 1.6.2: Cube before and after stretching, illustrating a Poisson's ratio of 0.5. [56]

1.6.3 von Mises stress

When designing components it is usually preferred to keep the component strain in the elastic region in figure 1.6.1, so it does not get fractured or deformed. Von Mises stress equation is used to determine if an isotropic- and ductile material will yield, when a certain complex load is applied. When applying the load to a component, for example compressing the component, an amount of energy gets transferred from the compression, to the object. This energy will either get stored in the component as a volume strain, or deviatoric strain. The volume strain will scale the volume of the component, and the deviatoric strain will affect the shape of the component, by shearing and distortion. The total von Mises stress is calculated by equation 1.6.2[57] where σ_v is the volumetric stress and σ_d is the deviatoric stress. [57]

$$\sigma_{VM} = \sqrt{\frac{2}{3} \cdot (\sigma_v + \sigma_d)} \quad (1.6.2)$$

Even though it is an empirical process, comparing the von Mises stress with the yield strength of the component material, will give a good sense if the material will yield or not. The yield strength of a material is the maximal stress a material can withstand before permanent deformation. When the curve enters the uniform plastic deformation area in figure 1.6.3, after the elastic deformation area, the material of the component will become more and more deformed as the stress increases. The deformation continues followed by necking, and fracture in the material. [57]

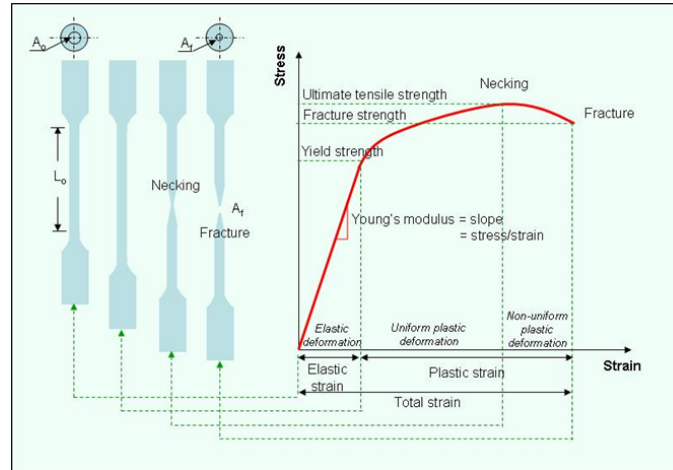


Figure 1.6.3: Stress-Strain Relationship under Uniaxial Tensile Loading [58]

1.6.4 Margin of safety

The Margin of Safety (MoS) is calculated to estimate if a given structure satisfies the strength requirements of an applied load.[59] The MoS is calculated with the expression in equation 1.6.3[59].

$$MoS = \frac{(Allowable\ yield\ stress) - (Required\ stress)}{Required\ stress} \quad (1.6.3)$$

A rule of thumb for having a structure with adequate strength for the applied load, is to have a $MoS \geq 0$. [59]

Chapter 2

Methods

2.1 Solid edge

Solid edge is a computer aided design program that make it possible to build 3-D models and drawings of parts, assemblies or wiring of electrical systems. [60]

Solid edge has two types of environments, ordered and synchronous. In ordered mode all sketches become a step, and further saved as memory. It is not possible to edit particular faces or relationships, and it is only possible to edit previous sketches and saved memory in this environment. The ordered mode can be seen as an assembly of surfaces glued together to a part. In synchronous environment, on the other hand, all faces and relationships can be edited. When editing a surface, it merges together with other contact faces. This makes the contact surfaces to one whole part, instead of separated, glued surfaces.[61]

For this project, Solid Edge 2020 student version is used, for building 3-D models of the end plates, flow field plates, bridges, gaskets and PTLs.[62] The modelling is done in synchronous mode with ISO metric standard, and converted as step files and drawings for the production suppliers.

Solid edge was also used to create models for fluid flow simulations in COMSOL Multiphysics. This was done by either making the models from scratch, or by using other modelled parts as cut-out tools, to form the flow field. The modelled parts created in solid edge was also assembled as a stack and imported into COMSOL Multiphysics for structural mechanic simulations.

2.2 Stack design and materials

2.2.1 End plates

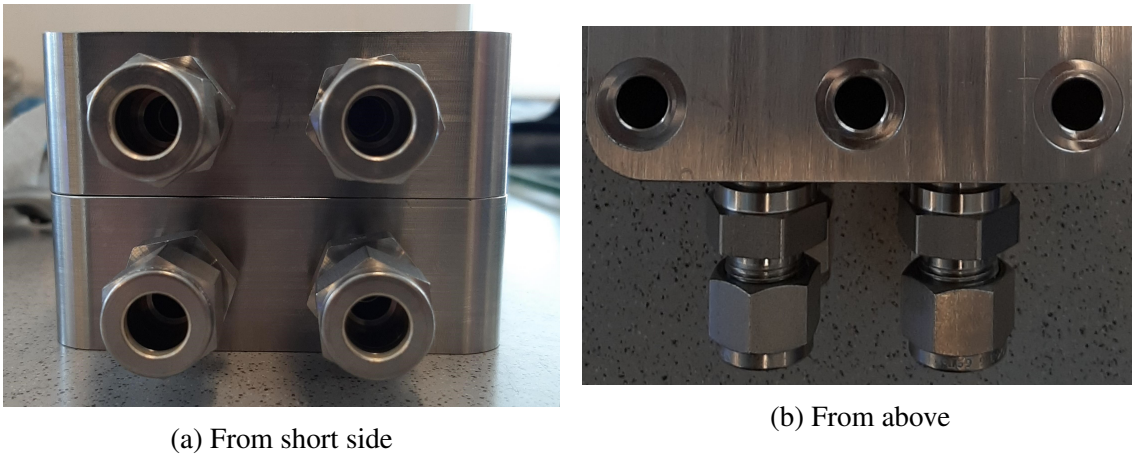
The end plates of the AEMWE stack are made of stainless steel 316 (ss316), with the properties shown in appendix B.1. Models of the end plates are illustrated in figure 2.2.1. There are 10 holes at the outer surface of both end plates, for bolts, and each of the holes at the top end plate have a 0.5mm groove for the helical compression springs.

Each end plate have four ISO 1/4" parallel threads, two on each short surface, to connect 3/8" Swagelok tube fittings. The Swagelok fittings is a connection between the water pump hose and the end plates, leading water from the water hose to the stack inlets, on the inner surface of the end plates. On the interface of the transition from the Swagelok fitting



Figure 2.2.1: End plate model, top- and bottom side, respectively

connection to the inlets, there will be placed a teflon gasket for sealing. The Swagelok fittings are shown in figure 2.2.2



(a) From short side

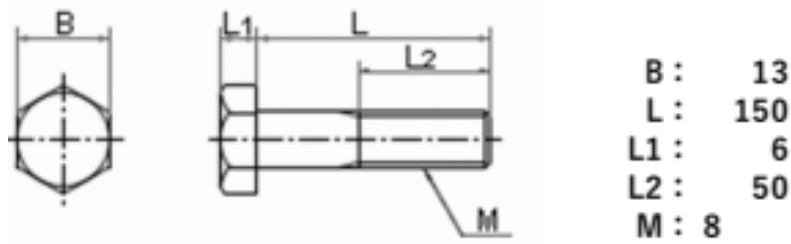
(b) From above

Figure 2.2.2: Swagelok couplings

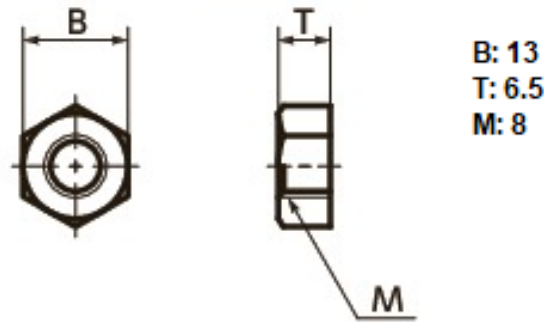
The dimensions of the end plates are shown in appendix A.1. To make the stack composition easier, it was intended to use guiding picks in the two small holes between the inlet/outlet in figure A.1.1. A solution to this was to move the centre bolt holes between the inlet/outlet, as in figure A.1.2, reducing the length of the end blocks with 32.5mm. The two centre bolts will be used as guidelines for the stack composition, leading the bolts through the stack, and constitute a significant reduction in the end plate volume. Comparing it with the original end plate design, it leads to a total volume reduction of more than 18%.

Clamping (bolts/nuts/springs)

Choosing the right bolts, nuts and springs for the compression of the stack is essential. For this AEMWE stack, bolts and nuts of RENY-material are chosen, with the parameters presented in figure 2.2.3 (a) and (b).



(a) RENEY bolt parameters in [mm] [63]

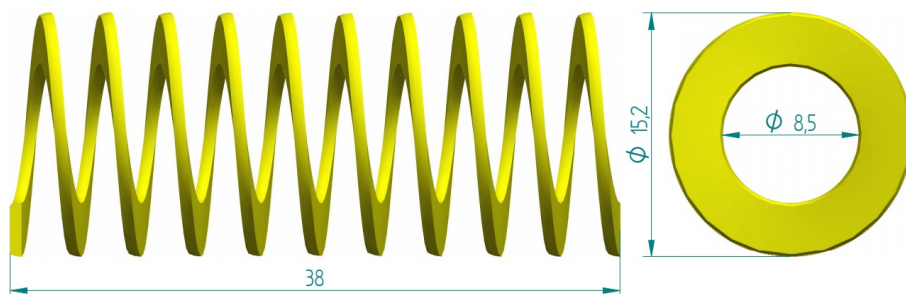


(b) RENEY nut parameters in [mm] [63]

Figure 2.2.3: Bolt and nut for stack clamping

RENY bolts(NBK1560) are used as substitutes for metal in a variety of applications, such as automobiles, machinery and construction. The RENEY material also has electrical insulation properties, making it applicable for electrical installations and electronics.[64] What makes the RENEY bolts the most durable of all plastic bolt materials is the polyamid MXD6 based polymer, reinforced with 50% glass fiber. In addition to this, the RENEY bolts also withstand up to 10% KOH solution. [65] The physical- and chemical properties of the RENEY bolts can be found in appendix B.5[63].

The helical compression spring are used for centring- and keeping the bolts in place. The springs used in this project are compression springs from FIBRO. The model being used is number 241.17.16.038, from the datasheet in appendix B.4 [66]. The springs that are used in this project got a guide sleeve of 15.2mm instead of 16mm that it is in the datasheet. A 3-D Model of the spring is shown in figure 2.2.4.

**Figure 2.2.4: Spring for bolt centering**

2.2.2 Flow field plate materials and design

Material selection

The bipolar plates must fulfil a number of different requirements such as high mechanical strength, high corrosion resistant, high heat conduction, high electrical conductivity and low Interfacial Contact Resistance (ICR). In this study, the selection of BPP material was made by SINTEF, which carried out a series of corrosion and ICR screening tests. A detailed summary of these measurements are out of the scope for this study, however, figure 2.2.5, shows a summary of the percentage increase in ICR after undergoing electrochemical corrosion testing. As possible to observed from the graph, the Inconel 625 showed a very stable behaviour after undergoing corrosion testing, the material shows the lowest increase in ICR. The bipolar plates were therefore decided to be made from Inconel 625, where the material properties are given in appendix B.2.

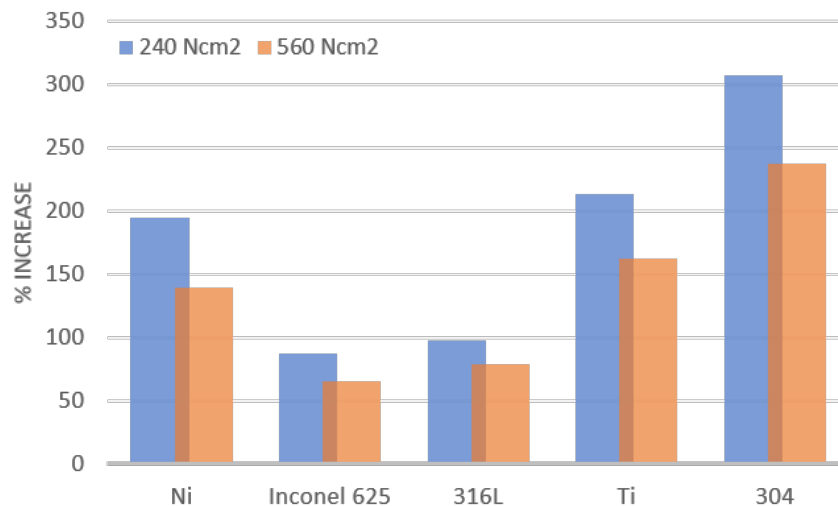


Figure 2.2.5: percentage increase of ICR before and after corrosion testing at two different compression pressures

Bipolar plates

The bipolar plates were designed with both the anode and cathode flow field on the same plate, with a thickness of 3mm, where both sides were made identical, illustrated in figure 2.2.6. This required a design that had inlets and outlets for both the anode and cathode side, which were connected to the flow field on one side of the plate and sealed from the other.

Each flow field was connected to the inlet and outlet on their respective side, giving an uneven surface for the gasket to seal. The solution to this was to make an immersion from the flow field area to the inlet/outlet areas with a ramp connecting the planes and flow channels. To support the gasket and refine the channel size at the immersion, a bridge component was designed (see figure 2.2.7). To have the same properties as the rest of the plate, the bridge was made from the same material.

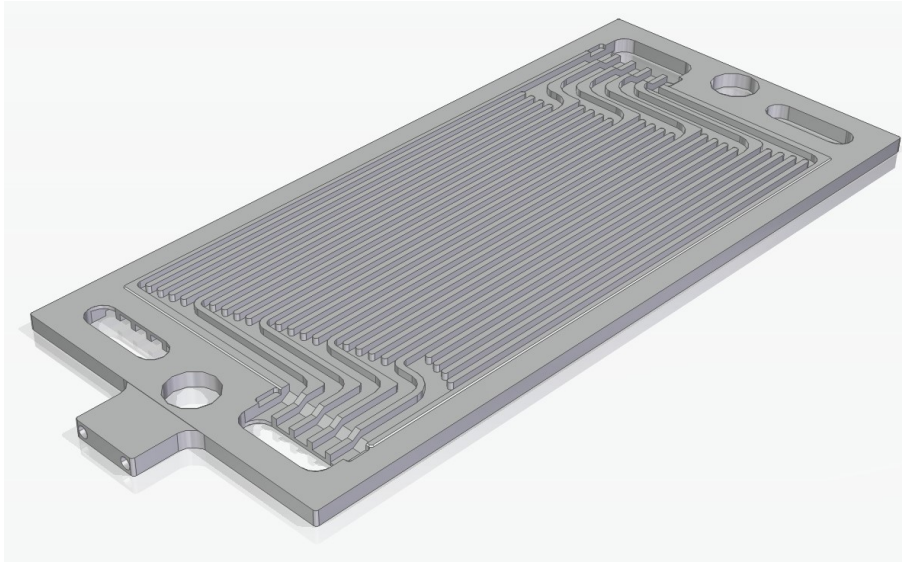
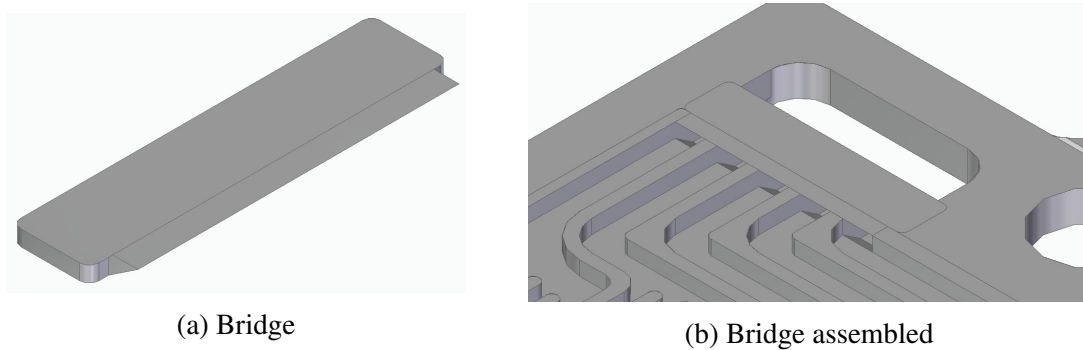


Figure 2.2.6: Illustration of the bipolar plate. Dimensions specified in appendix A.2.1.

Since the bridge was cut down into the plate, the channels were lowered as well. This made a height difference between the flow field and the inlet channel. By making a ramp from the lowered channels to the flow field, the channels could pass under the bridge without changing dimensions.



(a) Bridge

(b) Bridge assembled

Figure 2.2.7: Illustration of the bridge (a) and the bridge assembled on the bipolar plate (b). Dimensions specified in appendix A.4.

The inlets/outlets were dimensioned according to the width of the channels and ribs of the flow field and to prevent it from becoming a bottleneck. Between the inlets/outlets on each end of the plate there are holes for the bolts to go through, which also function as guide pins during assembly, to centre the plates.

In this stack, the PTL is either 0.5mm or 1mm thick, which is combined with a 1mm or 1.5mm gasket, respectively. To reduce the required gasket compression, the area around the edge of the flow field was lowered by 0.2mm. The edge was used to support and prevent the PTL from entering the flow channels at the edges of the flow field, while the corners against the gasket were angled to remove sharp points for the gasket to expand into. Originally, there were also edges around the inlets, outlets and around the plate, but these were removed to make more room for the gasket to expand.

To take measurements between the cells, a connector for 2mm banana plugs was made as an extension of the short side of the plate, shown above the bolt hole in figure 2.2.6. The connector was added outside of the plate to have more material around the holes, and to move them away from where the gasket would be compressed. Each connector was made with two holes, so that the plugs between the plates did not stand in the way of each other.

Unipolar plates

The unipolar plates were made identical to the bipolar plates except that they only had flow field on one side and were made with a terminal for the DC power supply, illustrated in figure 2.2.8. A unipolar plate was made for each side of the stack, where the current terminals were placed differently to prevent the connecting bolts coming into contact. The terminals also had to be long enough for the power supply to be connected without touching the end plates.

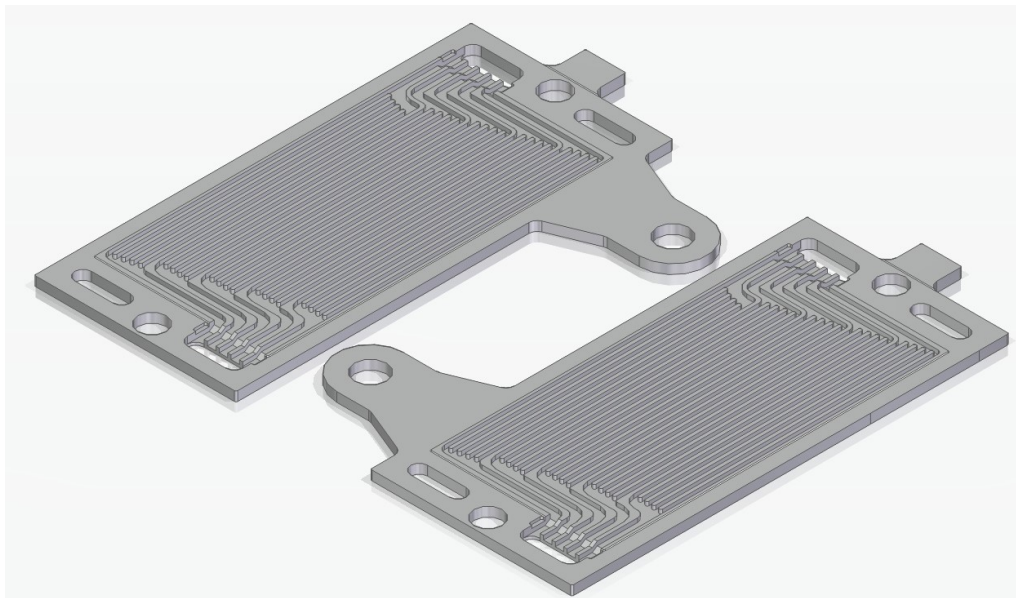


Figure 2.2.8: Illustration of the unipolar plates. Dimensions specified in appendix A.3.

Flow field

The flow field was designed to be used on both sides of a bipolar plate, which would be made from CNC milling, for an active cell area of 50cm^2 . These limitations laid the foundation for creating the flow field.

It was decided to make the flow field with the dimensions of $10 \times 5\text{cm}$. The next step was to decide the channel and rib widths. Since both channel and ribs are important for the cell performance, the widths were kept similar and set to 1.04mm and 1mm , respectively. This made it possible to start and end with channels in the active cell area, which at 5cm gave 25 channels and 24 ribs.

The flow field pattern used in the stack is shown in figure 2.2.9, where five channels from the inlet split into five sub channels each. This combines the shorter paths from a straight flow field, with multiple separate channels used in serpentine flow fields.

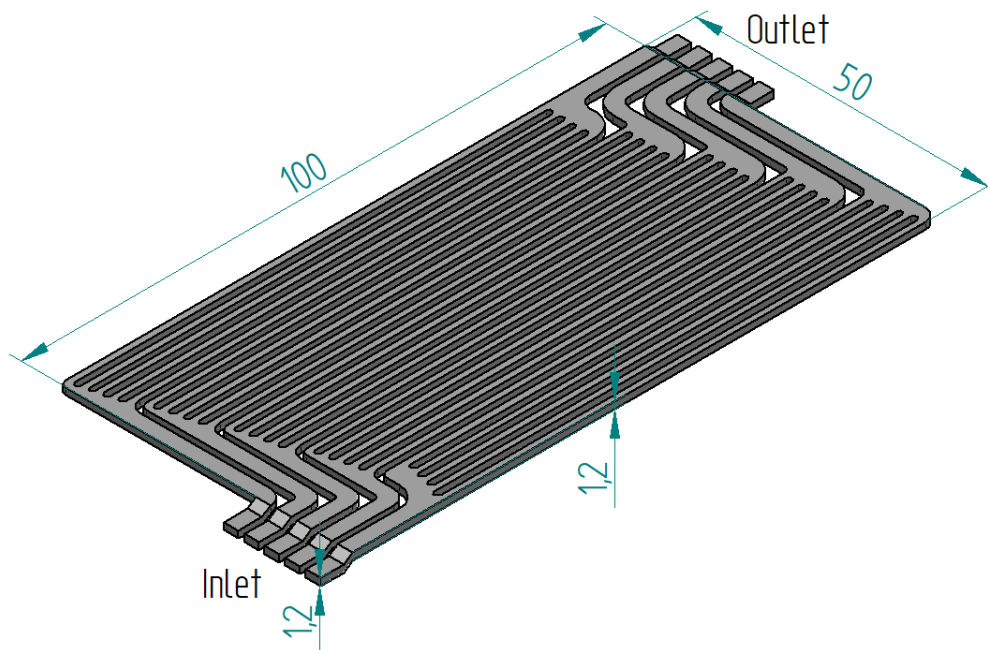


Figure 2.2.9: Illustration of the the final flow field. Dimensions specified in appendix A.6.1.

Fluid simulations in COMSOL Multiphysics were used to optimise the flow field, to get a uniform flow distribution among the sub channels, with low pressure drop. This were done by changing the channel dimensions, while keeping a similar pressure drop in the different channels. The distribution were improved by designing the channels with specified inlet and outlet side, where the specified dimensions of the flow field is given in appendix A.6.

Gaskets

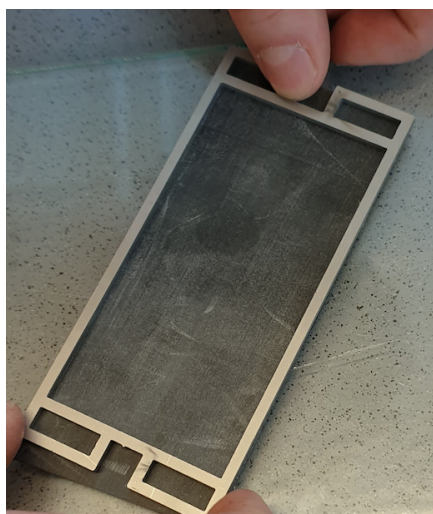
When designing and simulating the stack, a 1.5mm thick sheet of EPDM 4000 HG-60 rubber was used as gasket material (Datasheet in appendix B.3). The material has a Young's modulus of 1.8MPa, estimated between 0-100% deformation according to ISO37, and a Poisson's ratio of 0.5. If the gasket is used in a groove like an O-ring, the width can be as wide as the thickness, but if there are no support on the low pressure side, the gasket should be wider than the thickness of the gasket. For a relatively thin gasket, the compression is around 20-25%. [67]

One continuous gasket is used to seal the flow field, inlets and outlets, as illustrated in figure 2.2.10, where the width of the gasket is 3mm. Since the PTL has a height of 1mm, the gasket must be lowered with 0.5mm. This is done by placing the gasket 0.2mm below the rib surface, on the milled down surface of the plates, while the remaining 0.3mm is done by compressing the gasket. The other option was to use a 0.5mm PTL with a 1mm gasket, which required the same compression.

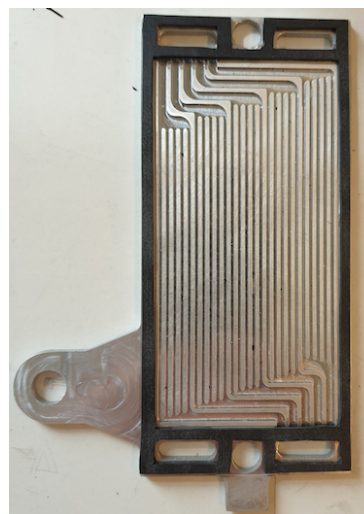


Figure 2.2.10: Illustration of the gasket assembled on a bipolar plate. Dimensions specified in appendix A.5.

The gaskets were cut out manually with the use of a template (see figure 2.2.11a), which was made of stainless steel and milled with CNC. This was to get a solid and accurate template for making even gaskets. To account for the cutting tool, which was a scalpel, the template was reduced with 0.1mm on each side, making the thickness 2.8mm. The gaskets were tested on a unipolar test plate that was made from aluminium, to see how the gasket fitted (see figure 2.2.11b). By using the same material and template, a gasket without the hole for the flow field was cut out and used to isolate the end plates.



(a) Gasket template



(b) Gasket on UPP

Figure 2.2.11: Gasket cut out with a template (a) and fitted on a unipolar test plate made from aluminium (b).

2.2.3 MEA

In this study, a Catalyst Coated Membrane (CCM) configuration was chosen for the AEMWE. In addition to the CCM, the CCM was assembled between two porous transport layer (PTLs), thus forming the complete membrane electrode assembly (MEA).

The MEAs were fabricated by SINTEF using some IP protected materials and procedures. Yet, a summary of the fabrication process is given below:

The electrodes are fabricated directly on the Anionic Exchange Membrane by spraying catalyst inks on the two sides of the AEM. The catalyst ink for the cathode consisted of commercially available 60% of Platinum on carbon support (Alfa Aesar) and anion exchange ionomer (selected by SINTEF). The ink is then diluted in a deionized water:IPA 1:1 solution. The ink is prepared targeting a final catalyst loading of 1 mg Pt/cm^2 on the electrode and the components are weighed in order to have a 24wt% of ionomer on the electrode and a final concentration of 3wt% of Pt/C in the ink. The catalyst ink for the anode consists of a mixture of Ir black (Alfa Aesar) and the same anion exchange ionomer (selected by SINTEF) as for the cathode was used. The target for the final catalyst loading is 3 mg Ir/cm^2 on the electrode and the components are weighed in order to have a 9wt% of ionomer on the electrode and a final concentration of 6wt% of Ir in solution.

A total of three 50cm^2 CCMs were coated using Anion Exchange Membrane (selected by SINTEF), which was received exchanged in hydroxide form and stored in DI water. The membrane was first dried and held on vacuum plate: this helps flatten the membrane, that is naturally wrinkled when dry. The vacuum plate is also heated at a temperature of 70°C . The shape of the active area was defined by putting a plastic template over the membrane and is finally spray coated by hand using a commercial airbrush connected to Argon gas line. Once one side is coated, the process is repeated on the other side with the other catalyst ink: the final result is a Catalyst Coated Membrane (CCM) (see figure 2.2.12).

To complete the MEA, Ni alloy felts were used as porous transport layers (PTLs) on both anode and cathode. The Ni PTLs are 0.5mm in thickness and have a porosity of approximately 66%. The PTLs were acquired from Bekaert.

2.3 COMSOL Multiphysics

COMSOL Multiphysics is a modelling and simulation program that solves physical problems based on advanced numerical methods.[68] In this case, version 5.5 was used to simulate fluid flow over the flow field plates and to perform stress test on the stack to simulate the compression on the gaskets. Due to personal computer limitations, the simulations have been performed with stationary studies for both fluid flow and stress, where simplifications have been used if possible. For more demanding tasks, an auxiliary sweep was performed.

3D-models of the stack were created and assembled in Solid edge, and imported as STP files to COMSOL. In COMSOL meshing was added, and parts were connected with the automatic form union function. The form union option makes the stack assembly work as one component, and merges contact surfaces. This make the simulation linear, and easier to compute. This can cause the simulation results to deviate from practice.

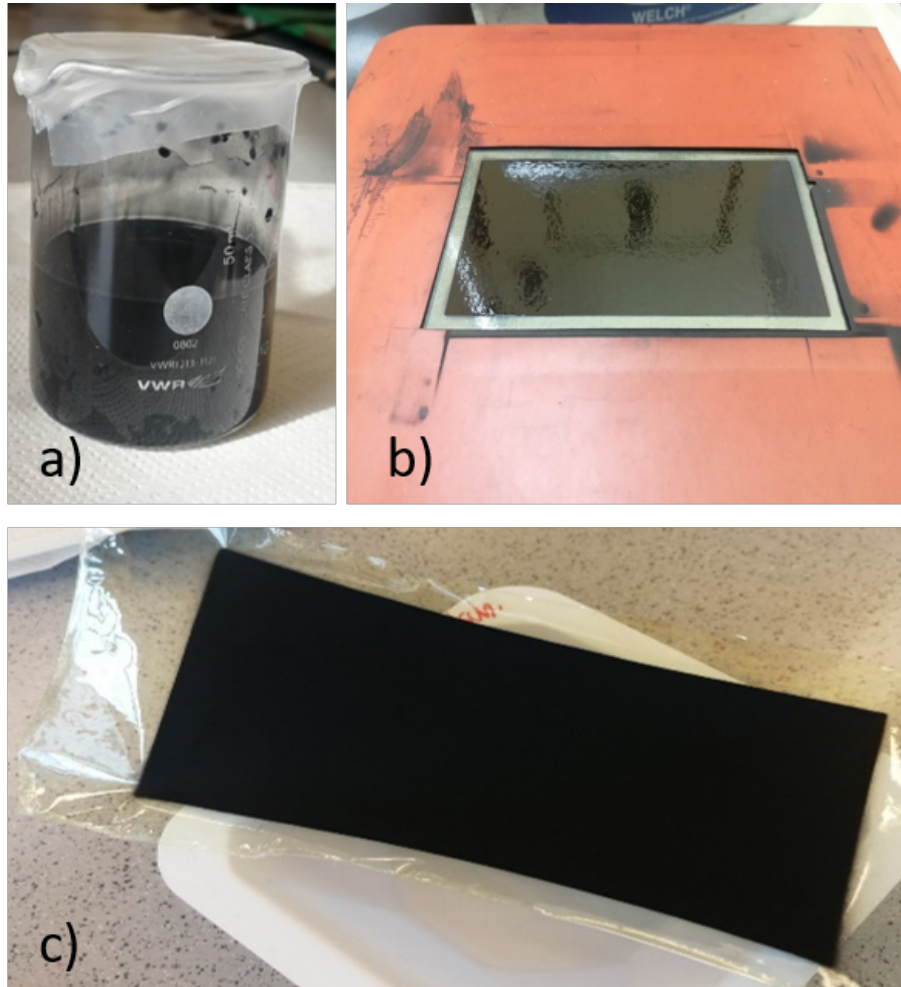


Figure 2.2.12: CCM fabrication procedure a) Catalytic ink solution, b) hot vacuum plate and c) finished CCM.

2.4 Simulation

2.4.1 Computational Fluid Dynamics

Fluid flow can be analysed from practical experiments or from calculations. Experiments requires equipment, while calculations can be done with the use of computers. Simulations of fluid flow with computers is called CFD and have made it possible to analyse fluid flow behaviour of more advanced problems. CFD is not a replacement for experimental results but a tool used to complement and reduce the required amount of experimental testing. Analysing the fluid flow with CFD requires numerical methods and a mathematical model like the Navier-Stokes equations, which is used to simulate fluid flow.[69] Where CFD has limitations, is for solving turbulent fluid flow that requires appropriate turbulent models and more computer resources. [70]

Meshing

Since the mathematical model only can be solved when assuming linearity, the geometry is divided up into smaller elements, where calculation is performed [69]. This grid that divides the model geometry into smaller elements is called a mesh, which is illustrated in

figure 2.4.1. The size and shape of the elements depend on the model geometry and the fineness of the mesh, where the mesh quality is important for a reliable result. There is an optimal quality of the mesh, where increasing the number of elements have little affect for the result. The optimal mesh can be found by starting with a coarse mesh and gradually increasing the fineness.[69] Finer mesh can give a more accurate result but requires more time and computer resources to perform. [70]

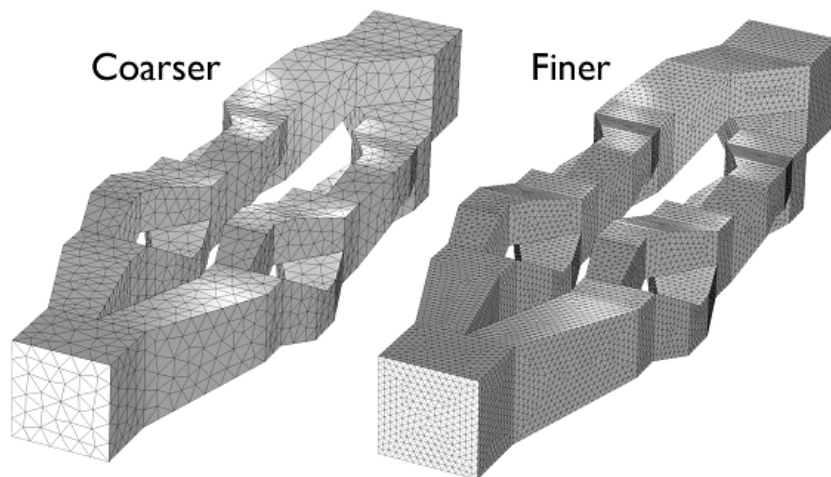


Figure 2.4.1: Illustrating a model with coarser and finer mesh.[71]

Boundary conditions

When simulating fluid flow, the model must be set with boundaries to establish a path, entrance and exit point for the flow. This is referred to as boundary conditions, which are set for walls, inlets and outlets. The walls of the model stop the fluid from passing through and is usually set with a no-slip condition, where the fluid velocity in contact with the wall is zero.[48] For the inlet and outlet, the boundaries are set with velocity- or pressure-specified conditions, where they can have either of them but not both. These conditions are used to calculate how the fluid flows through the system, to reach the boundary condition set. For example, when specifying the inlet with velocity and the outlet with pressure, the pressure at the inlet and the velocity at the outlet necessary to achieve both boundary conditions are calculated.[70]

Solving CFD

Every element in the mesh are set with initial starting conditions and solved using equation 1.5.4 and 1.5.5. If all parts of equation 1.5.4 is put on one side, the computation will run until the solution is close to zero in all the elements. How close it gets to zero before finding a solution is dependent on the margin of error set, which is the difference in error from the previous calculation. Each time the value is above this margin, another calculation is needed, and this is referred to as an iteration.[69] The number of iterations for each computation is different and could require thousands, before the difference between the error converges to a steady solution.[70]

2.4.2 Fluid flow simulation

Fluid flow simulation was used to find and optimise the flow field for the flow field plates, where different inlet/outlets, channel dimensions and patterns were tested and compared. To simplify the simulations, the flow field were divided up into sections and compared individually before it was assembled and tested.

The fluid simulation is based on the Navier-Stokes equations and the continuity equation, which was solved with the use of boundary conditions for inlet, outlet and walls of the model, to calculate the mass flow and pressure in the model geometry [47]. The simulations was performed with laminar flow of single phased liquid water, which was in the program, where simulations with a KOH solutions had to be added as a blank material with parameters for density and dynamic viscosity. Meshing was put to normal, and then finer or coarser depending on the model. For boundary conditions, the inlet was specified with different rates of mass flow, walls had a no-slip condition and the outlet was set to ambient pressure.

Results were compared by flow velocity [m/s] and pressure [Pa]. Velocity was displayed as a slice in the geometry, shown in figure 2.4.2, to analyse how the fluid travelled through the flow field. For more accurate results, the velocity was plotted from the average derived values by selecting the surface of the desired cross section, which gave the average velocity in each sub channel. This was possible since the flow field was cut in half and assembled in solid edge, where the connection between the parts made a surface. The average velocity was then converted to flow rate [g/min] for comparison.

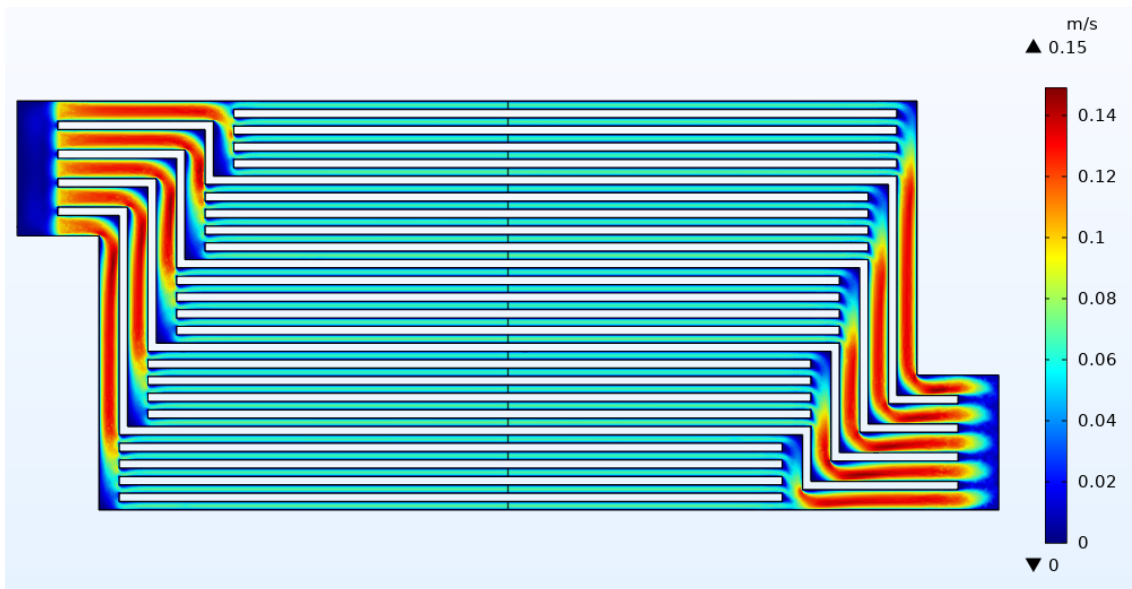


Figure 2.4.2: Flow field velocity simulation in COMSOL

Pressure was displayed as surface and contour to give an indication on where the impact zones were, shown in figure 2.4.3. More accurate data was plotted by using the maximum- and minimum derived value for volumes and selecting the relevant geometry. This gave the maximum- and minimum pressure, respectively, which was used to find the pressure drop.

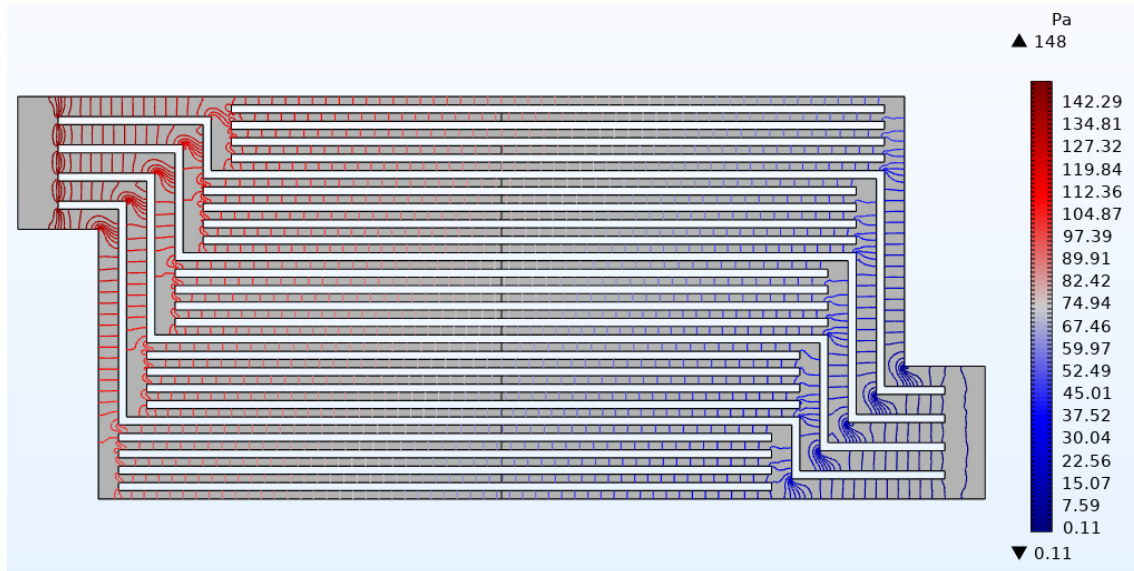


Figure 2.4.3: Flow field pressure simulation in COMSOL

2.4.3 Structural Mechanics simulation

To compress the gaskets for the desired length, the force on each bolt of the stack had to be estimated. To do this, a simulation method called structural mechanics were used. This simulation method also made it possible to analyse the deformation of the gaskets, horizontal expansion, and stress and strain that arose as a result of the compression.[72] To analyse the expansion of the gaskets is essential for estimating the groove length for the gaskets. This is for not having the gasket expansion interfering with other components, and to prevent leakage. An analogy of the structural mechanics simulation is shown in figure 2.4.4

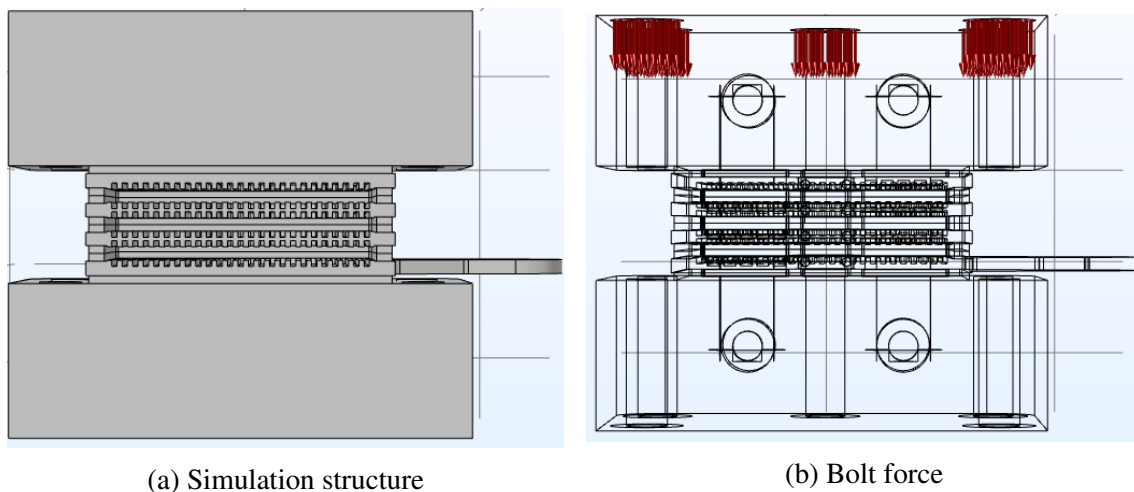


Figure 2.4.4: Compression simulation

Simulations were performed on half of the stack size, with one- and three cells, shown in figure 2.4.4a. Boundary conditions were set to symmetry on all cut edges, fixed constraint on the bottom surface of the stack, and boundary load at the top surface. To simulate the force from the bolts with boundary load, surfaces were added in Solid Edge with the same surface area of the springs used to keep the bolts in place. The force from the bolt surface

is shown in figure 2.4.4b. The mesh was put to normal (Figure 2.4.5a), and the quality adjusted for parts and surfaces of interest, as shown in figure 2.4.5 and 2.4.6.

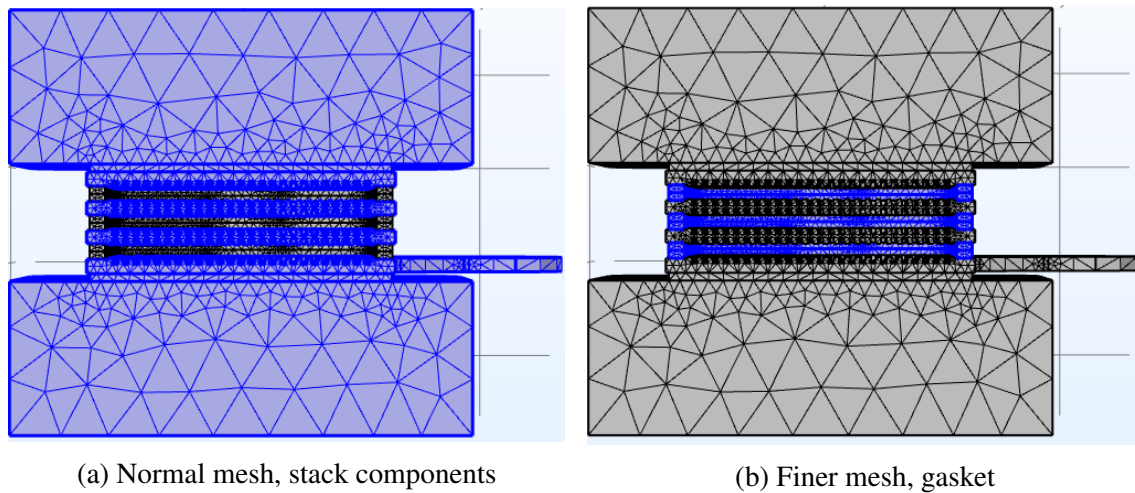


Figure 2.4.5: Meshing of components

The built in material “Steel AISI 4340” was used on every part except for the gaskets, which had a blank material with different values for Young’s modulus, Poisson’s ratio and material density. There are 6 gaskets, as marked blue in figure 2.4.5b, needed to be compressed for a total of 1.8mm. Two and two gaskets are paired on top of each other in the stack, forming three layers, one for each cell. For the visualisation of the mesh of the bridges in figure 2.4.6, other components between the end plates have been hidden.

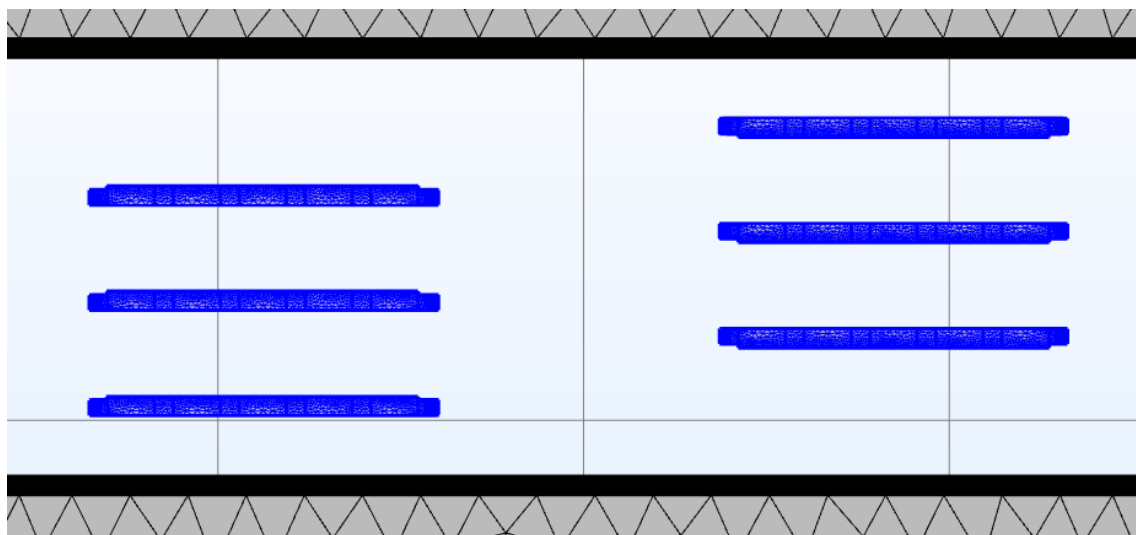
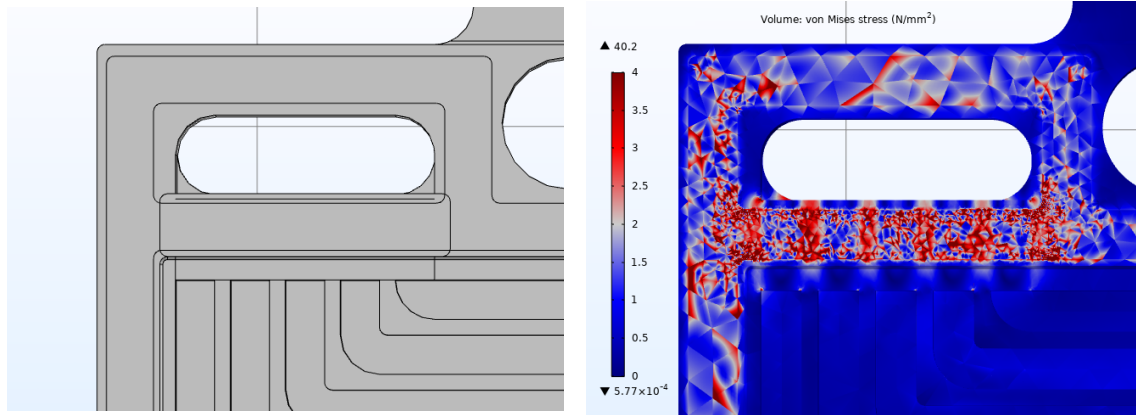


Figure 2.4.6: Extremely fine mesh, bridges

The stress and strain occurring on components from the compression, was analysed with a volume plot of the von Mises stresses. The von Mises stress was further compared with the yield strength of the component material, to evaluate the margin of safety.

The most fragile component of the stack are the bridges, being 0.8mm thick. The bridges will support the gaskets during compression, which may cause a high amount of stress on the bridges. Figure 2.4.7 visualise the gasket compression on a flow field plate. The

figure shows the bridge area, with the bridge lying on top of the inlet’s ribs. This is what causes the red vertical lines of von Mises stress after compression, in figure 2.4.7b.



(a) Bridge area from area from above.

(b) von Mises stress, bridge area.

Figure 2.4.7: Compression simulation, 115 [N] per bolt: von Mises stress from the gasket compression, from above.

To simulate the stress and strain in the gaskets under compression and operating pressure, two gaskets were assembled between the end plates. The compression was simulated with prescribed displacement, while pressure was added with boundary load on the inside of the gasket, as seen in figure 2.4.8.

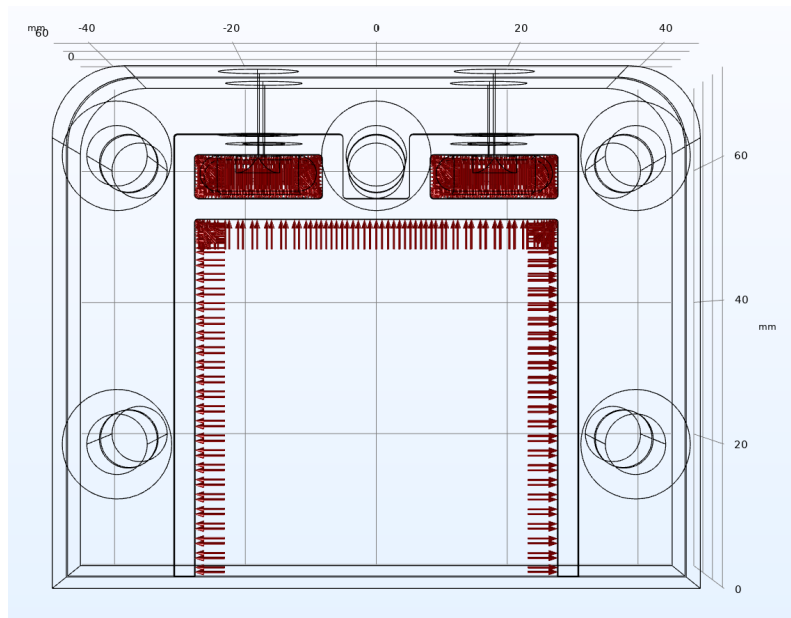


Figure 2.4.8: Simulating pressure on the inside of the gasket.

2.5 Matlab

Matlab is a tool for solving mathematical problems with over 300 functions and the option to make own functions, where results can be displayed graphically [73]. In this case, Matlab R2019a/b was used for simple calculations of the results from fluid simulation in COMSOL, and used to display the data in graphs.

Chapter 3

Results

3.1 Fluid flow simulation

The simulation was first used to find the best flow field pattern to optimise. In the next step different parts of the flow field were separated and individually simulated for better performance, while in the last step the parts were combined to create a flow field with uniform flow distribution and low pressure drop.

All fluid flow simulations were performed with automatically added normal mesh and with water at 20°C unless other information is provided. The results from COMSOL were calculated in Matlab, where the average velocity was converted to flow rate with equation C.0.1, where the water density of 998kg/m³ was from appendix C.9.1, and pressure drop was calculated from the minimum and maximum pressure readings from COMSOL.

3.1.1 Flow field pattern design

The simulations on the flow fields in figure 3.1.1 were performed with a coarse mesh and a flow rate of 50g/min. This was to see how the fluid was distributed among the sub channels, and to find a design to optimise. The fluid distribution is shown in figure 3.1.1 as a velocity field in the centre of the flow field, while the results of the pressures are given in table C.1.1 and are displayed as pressure drop in table 3.1.1.

Table 3.1.1: Pressure drop over the flow fields in figure 3.1.1 at 50g/min.

Flow field	Pressure drop [Pa]
Straight	343
Straight V-neck	212
5ch horizontal	181
5ch vertical	190

In figure 3.1.1 the velocity in the flow fields are given with their respective colour scale and vary with each figure. Both 3.1.1a and 3.1.1b have a lower distribution in the centre sub channels, while 3.1.1c and 3.1.1d have a repeating pattern in the channels that favour the last sub channel from the inlet.

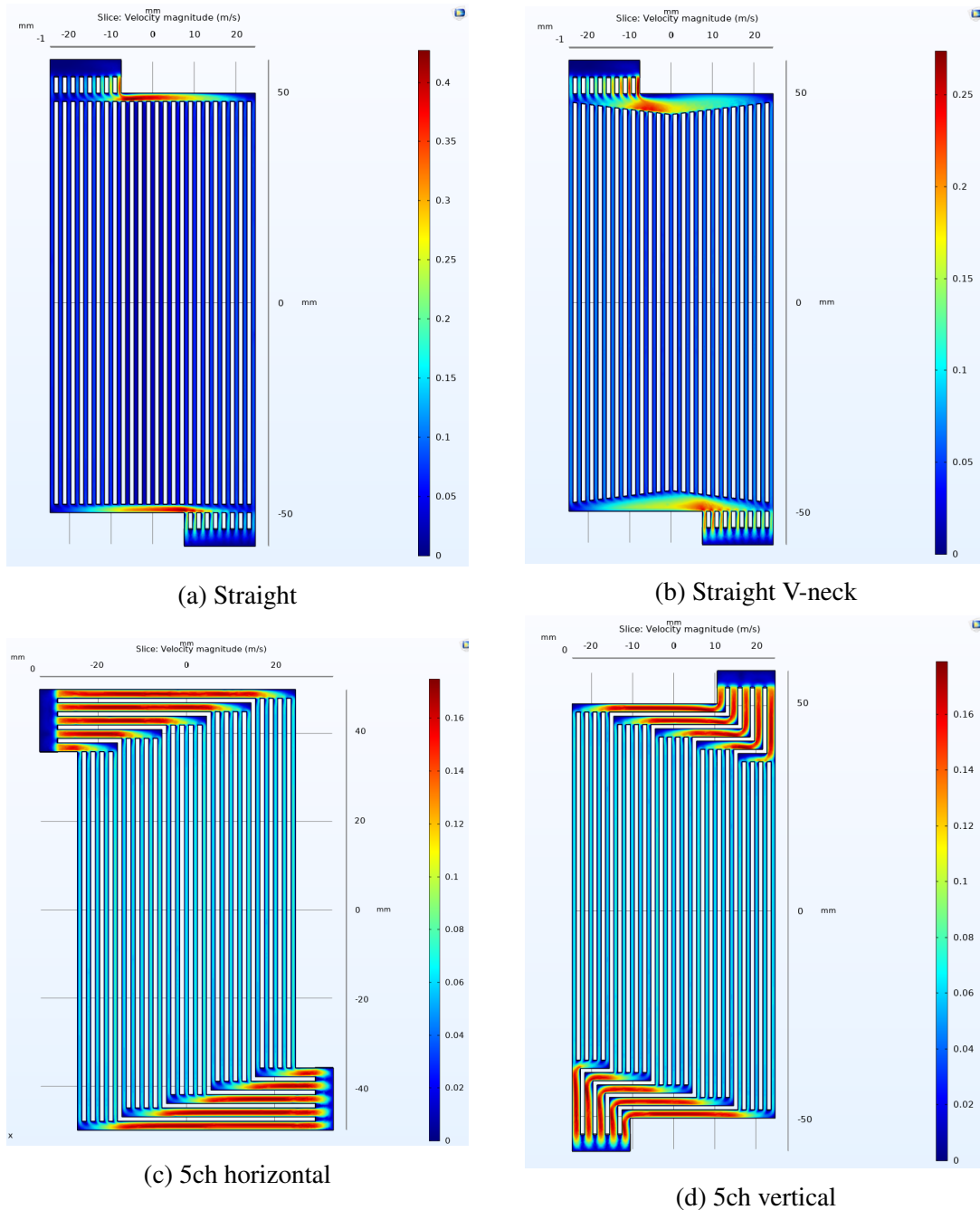


Figure 3.1.1: Velocity field in [m/s] for different flow field patterns, simulated at 50g/min from the inlet at the top.

3.1.2 Centre channel variations

The flow field pattern from figure 3.1.1d were selected as the design to optimise, where the first step was to find out how the flow distribution in the sub channels could be improved. This was done by only simulating on the centre channel with different changes, illustrated in figure 3.1.2. The results from the simulations are given in table C.2.1 and presented as flow rate and pressure drop in table 3.1.2.

In figure 3.1.2, the velocity field shows the fluid distribution in the channels, where even coloured sub channels indicate a uniform distribution, while dark blue areas indicate low flow zones. The effect of the changes is listed in table 3.1.3.

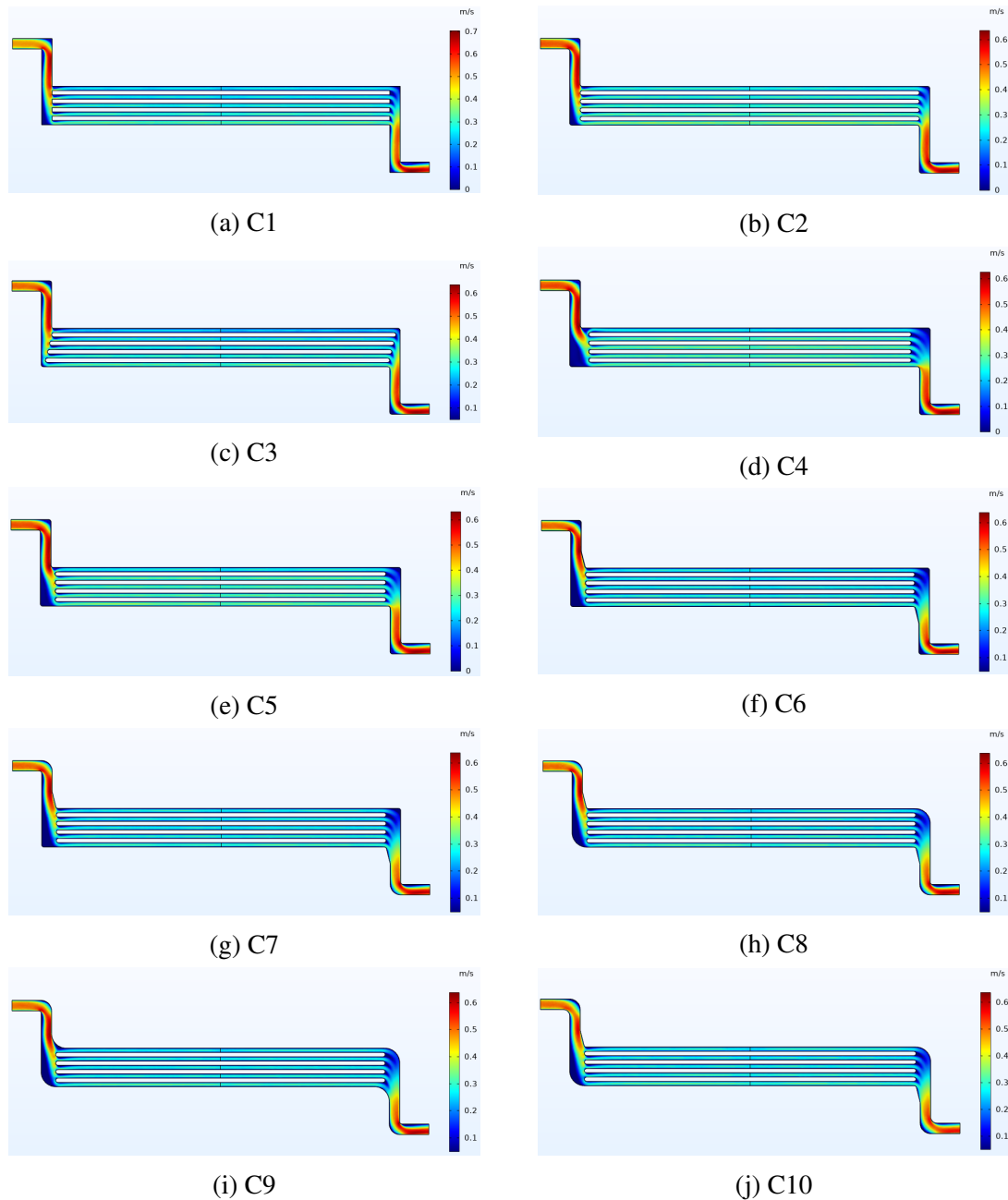


Figure 3.1.2: Velocity fields in [m/s] of different centre channels with a flow rate of 50g/min. Inlet from the left with sub channel (1-5) from the top. Dimensions specified in figure C.2.1.

From table 3.1.2, the flow distribution in the channels favour sub channel 5, while sub channel 1 have the worst flow rate. In channel C1, the difference between sub channel 1 and 5 is 2.96g/min, while the difference in C10 is 1.18g/min, with 255Pa lower pressure drop. These simulations showed what changes to different parts of the channel did for the flow distribution, and was used as the foundation when optimising the entire flow field.

Table 3.1.2: Flow rate in the sub channels and pressure drop over the channels simulated at 50g/min, displayed in figure 3.1.2.

Channel	Flow rate [g/min]					Pressure drop [Pa]
	Sub 1	Sub 2	Sub 3	Sub 4	Sub 5	Total
C1	8.52	9.04	9.64	10.34	11.48	1035
C2	8.83	9.24	9.59	10.16	11.21	947
C3	8.30	9.59	9.73	10.39	11.04	965
C4	8.02	10.11	10.50	10.14	10.26	914
C5	8.18	10.23	9.97	10.13	10.53	926
C6	9.31	9.59	9.67	9.97	10.50	896
C7	9.30	9.65	9.66	9.96	10.47	888
C8	9.37	9.63	9.61	9.93	10.49	882
C9	9.36	9.59	9.57	9.88	10.66	882
C10	9.35	9.58	9.60	9.96	10.53	780

Table 3.1.3: The effect of the different centre channel design in figure 3.1.2.

Channel	Change	Effect
C1	Original design	High pressure drop and bad flow distribution
C2	Rounded edges/corners	Lower pressure drop and better distribution
C3	Different length of ribs	Restriction for sub 5 inlet and sub 1 outlet
C4/C5	Shorter rib length	Better distribution in sub 2-5 and worse in sub 1
C6	Incline to the sub channels	Better flow rate in sub 1
C7	Outer bend radius	Remove dark blue zones
C8	Radius above sub channels	Remove dark blue zones
C9	Radius to the sub channels	Less restriction for sub 5 outlet
C10	Inner bend radius	Lower pressure drop

3.1.3 Channel depth

Pressure drop

To see how the channel depth affected the pressure drop, multiple depths was tested for the same channel, ranging from 0.5 to 1.3 mm with a flow rate of up to 50g/min. Figure 3.1.3 illustrate how the pressure drop over the channel is distributed. The results from the simulation are given in table C.3.1 and displayed in figure 3.1.4 with pressure drop as a function of the simulated flow rate. From the graph in figure 3.1.4, the pressure drop is increasingly increased when the channel depth is lowered.

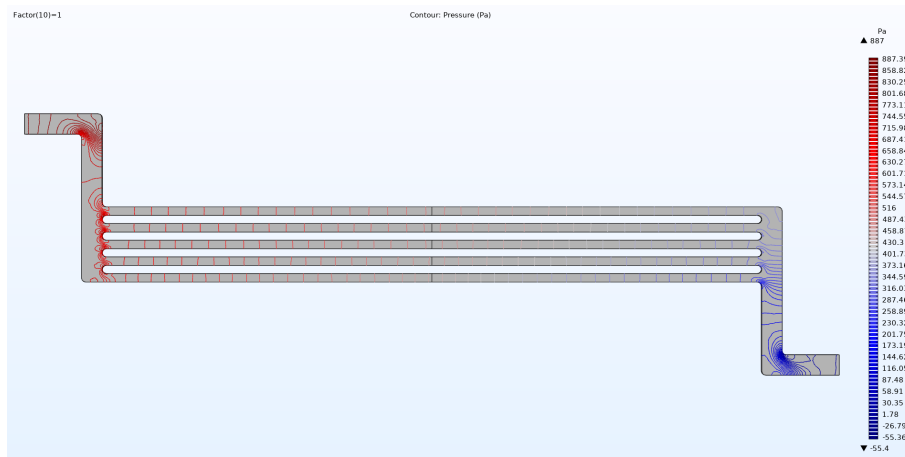


Figure 3.1.3: Illustrating the pressure drop distribution as contour lines at 50g/min over the channel in figure C.2.1b, with a channel depth of 1mm.

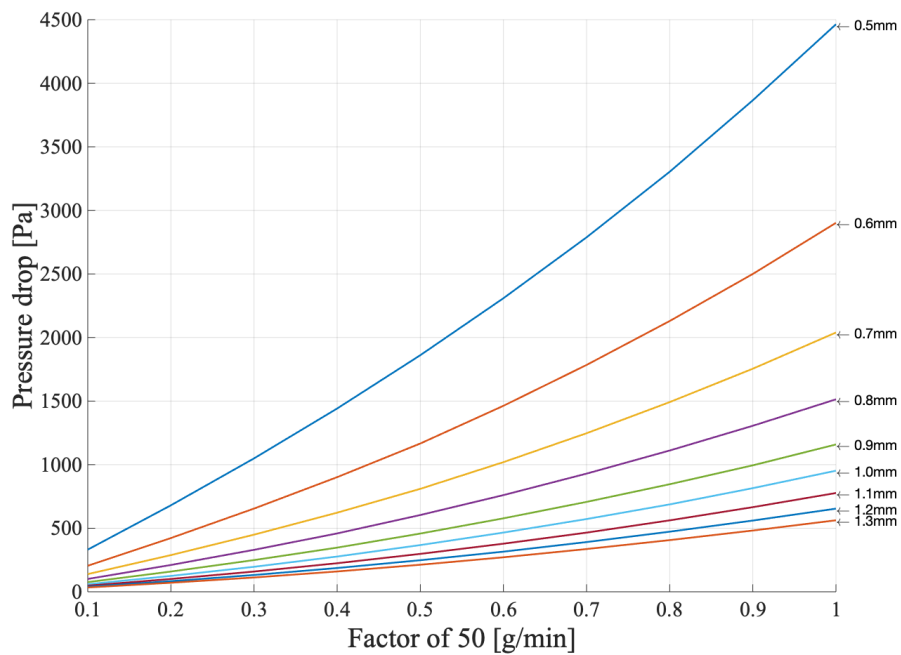


Figure 3.1.4: Pressure drop for different channel depths (0.5-1.3mm) of the channel in figure 3.1.3 as a function of the simulated flow rate.

Flow distribution

The simulations used to find the pressure drop in figure 3.1.4 were used to find the flow distribution for the different depths. This was to see if the distribution was affected by the channel depth. The velocity results at 50g/min from the simulations are given in table C.3.2 and displayed as flow rate in table 3.1.4.

From table 3.1.4, the flow rate in the sub channels is increased from sub channel 1 to 5 for all depths, where there is no correlating change in the flow rate in the sub channels as the depth of the channel changes.

Table 3.1.4: Flow distribution with different depths for the channel in figure 3.1.3, at 50g/min. Displaying flow rate [g/min] in each sub channel.

Depth	Sub 1	Sub 2	Sub 3	Sub 4	Sub 5
0.5 mm	8.82	9.23	9.58	10.19	11.08
0.6 mm	8.95	9.18	9.57	10.22	11.12
0.7 mm	8.87	9.20	9.57	10.20	11.08
0.8 mm	8.81	9.18	9.57	10.21	11.13
0.9 mm	8.79	9.25	9.62	10.20	11.24
1.0 mm	8.85	9.25	9.58	10.21	11.14
1.1 mm	8.75	9.22	9.68	10.27	11.11
1.2 mm	8.67	9.30	9.69	10.34	10.98
1.3 mm	8.77	9.23	9.65	10.19	11.04

3.1.4 Inlet

To find the bottle neck in the inlet from the supply to the channels, the different geometries was simulated with a flow rate of up to 250g/min at a length of 1000mm. The results are given in table C.4.1 and shown in figure 3.1.5, where the pipe is the entrance from the supply connection and the duct is the passage from the pipe to the flow fields. From the graph, the pressure drop is higher in the pipe, which has a steeper curve, while the radius on the duct has a small increase.

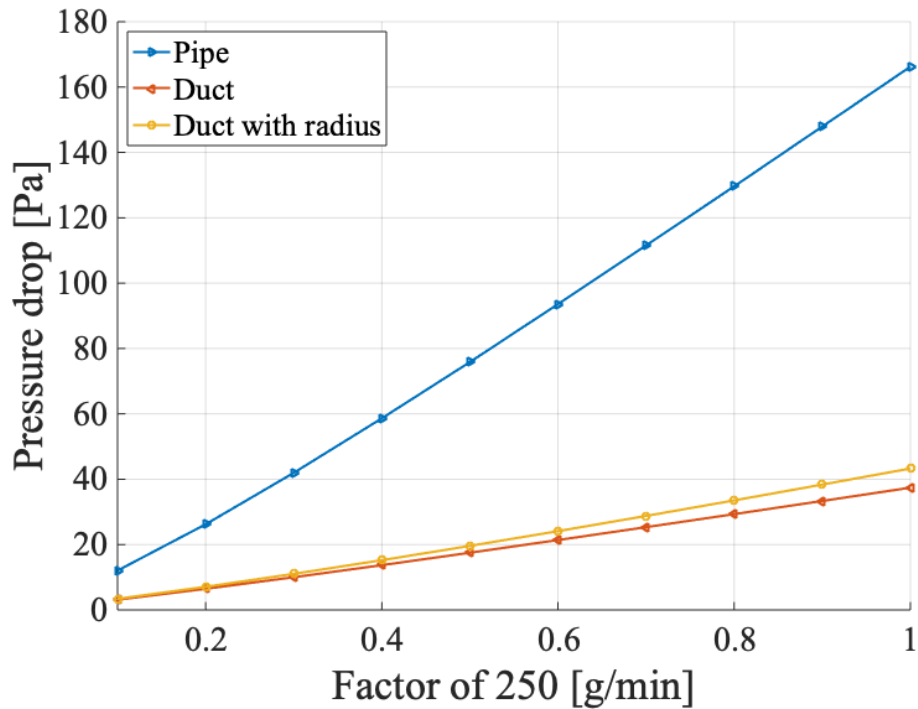


Figure 3.1.5: Pressure drop over different geometries with a length of 1000mm, Pipe (6.35mm), duct (16.5x5mm) and duct with radius (2.5mm radius), illustrated in figure C.4.1.

3.1.5 Immersion channel

The channels had to pass under the bridge that supported the gasket, which gave a restriction on the channels. Two different solutions were simulated to reduce the implication this had to the flow field. Figure 3.1.6 shows the pressure contour over the different solutions, with dimensional changes in 3.1.6a and a ramp in figure 3.1.6b. From the figures, the pressure drop was around 70Pa with dimension changes and around 50Pa with a ramp.

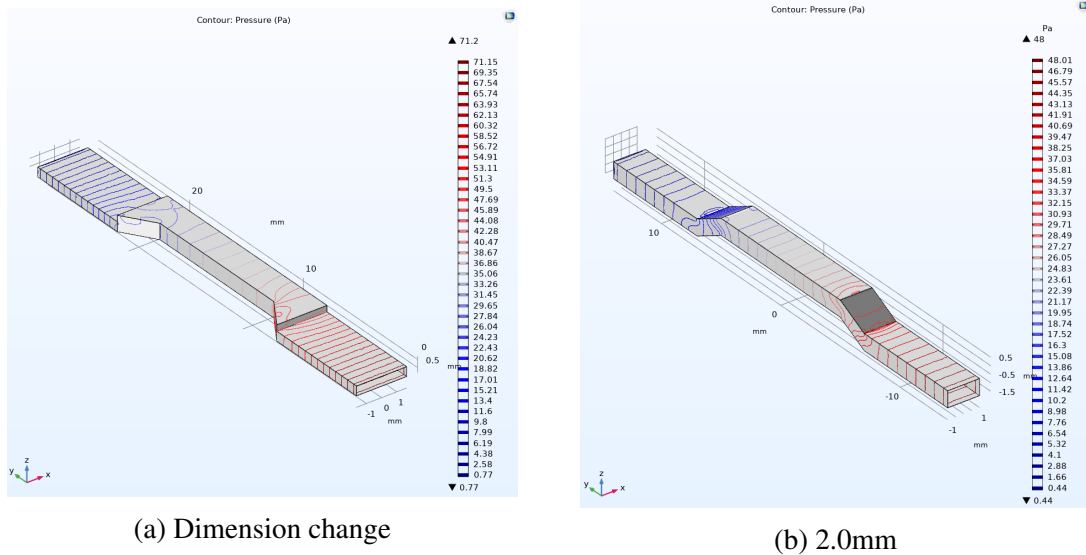


Figure 3.1.6: Pressure contour of the different channel geometry under the bridge with a flow rate of 10g/min. The model dimensions are specified in figure C.5.1.

Ramp

Since the ramp design had a lower pressure drop, this was chosen and further simulated to find the optimal design of the ramp. The results from the simulation of the different ramp designs are displayed with pressure contour in figure 3.1.7 and velocity field in figure 3.1.8.

From figure 3.1.7, the collection of contour lines in the ramp is reduced for the increased ramp length, where in figure 3.1.7d the ramp has little effect on the contour lines.

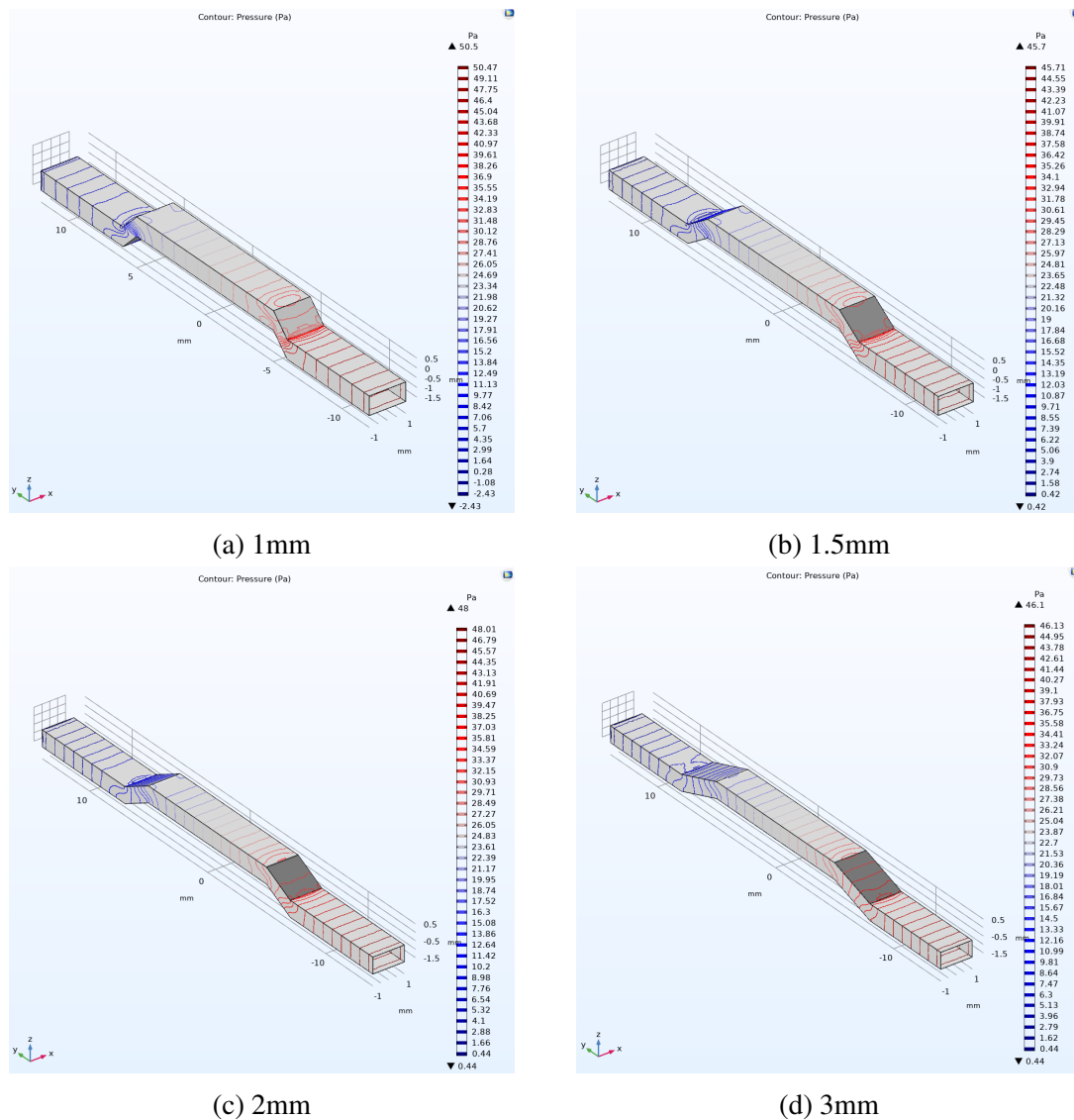


Figure 3.1.7: Pressure contour of the channel ramp under the bridge, where the channel is moved up 1, 1.5, 2 and 3mm. The model dimensions are specified in figure C.5.1.

The velocity field in figure 3.1.8 indicate that the velocity is highest in the ramp and decreases with the increased length, where the change between figure 3.1.8a and 3.1.8b.

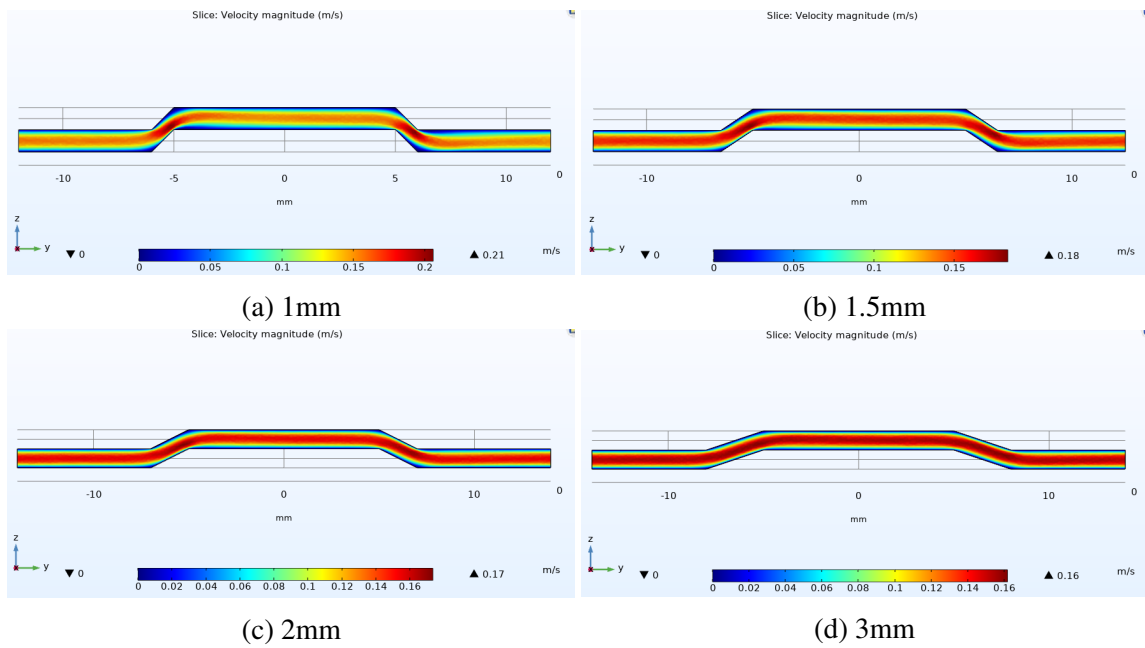


Figure 3.1.8: Velocity field of the channel ramp under the bridge, where the channel is moved up 1mm in 1, 1.5, 2 and 3mm. The model dimensions are specified in figure C.5.1.

3.1.6 Channel width

To see the effect of changing the channel width from the inlet to the sub channels, two flow fields were simulated with a flow rate of 50g/min, see figure 3.1.9. The pressure results are given in table C.6.1, which gave a pressure drop of 215Pa and 171Pa for the flow field in figure 3.1.9a and 3.1.9b, respectively. In the figures, the transparent section between the inlet and flow field is the immersed channel and ramp section, which is at another height than the velocity slice and therefore not included. The velocity fields have different colour scales, where the velocity in the 2.5mm channels to the sub channels are lower.

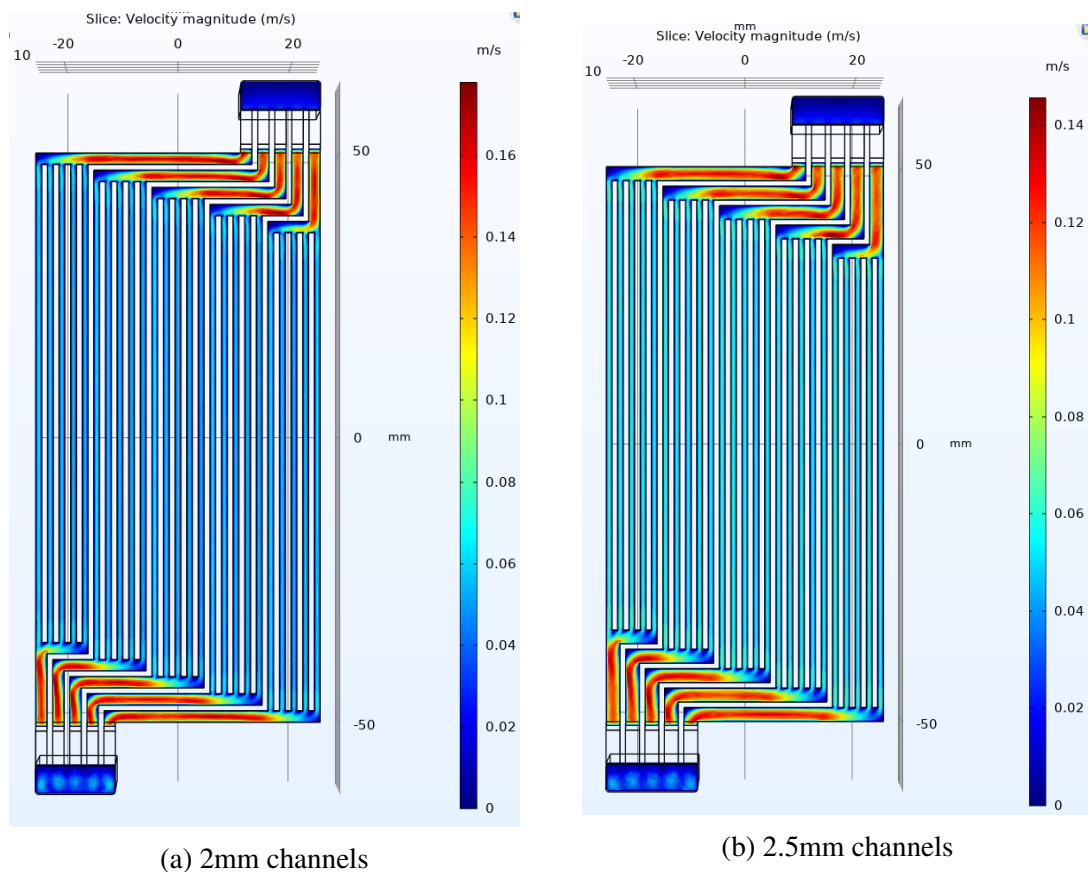


Figure 3.1.9: Velocity field of different channel widths, 2mm (a) and 2.5mm (b) with 1mm rib at 50g/min. Specified dimensions in figure C.6.1.

3.1.7 Flow field with identical inlet/outlet

Figure 3.1.10 illustrates how the flow distribution could be optimised by using the simulations from 3.1.2 as a starting point and changing the parameters for each channel in the flow field. The simulation was performed with a flow rate of 50g/min per channel, where the results are given in table C.7.1 and displayed in table 3.1.5 as flow rate in the sub channels and pressure drop over the channels.

In figure 3.1.10, the flow field is made from two identical half side with the inlets on the left side. Channel 1 to 5 starts from the top and the same goes for the sub channels. The flow in channel 1 is different from the rest, where the inlet is directly above the sub channels. There are also dark blue areas above the sub channels in all of the channels, which indicate that the fluid has low or no velocity.

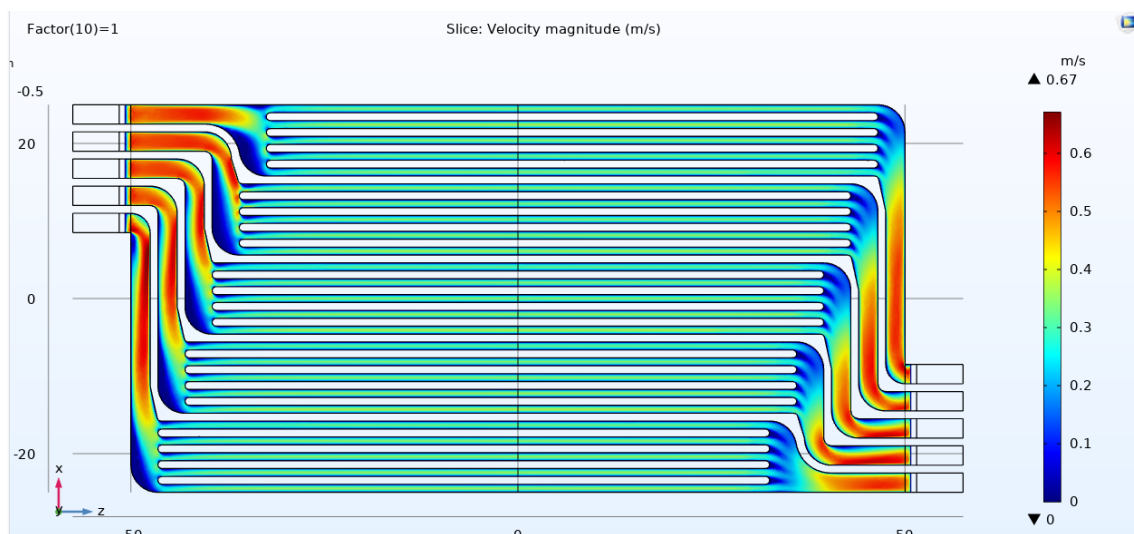


Figure 3.1.10: Velocity field of the five channels in the flow field with a flow rate of 50 g/min per channel. Dimensions specified in figure C.7.1.

From table 3.1.5, channel 3 and 4 has the worst distribution, where the flow rate increases from sub channel 1 to 5 with a maximum difference of 1.34g/min and 1.5g/min, respectively.

Table 3.1.5: Flow rate [g/min] in the sub channels and pressure drop [Pa] over the channels in figure 3.1.10, with a flow rate of 50g/min.

Channel	Sub 1	sub 2	Sub 3	Sub 4	Sub 5	Pressure drop
1	9.60	10.45	9.82	9.46	9.80	1029
2	9.90	9.52	9.54	9.88	10.34	1069
3	9.19	9.61	9.74	10.09	10.53	1064
4	9.08	9.59	9.74	10.10	10.58	1049
5	9.22	9.86	9.96	10.07	10.03	1000

3.1.8 Final flow field

Simulations were performed on flow field channels with different inlet and outlet changes to improve the flow distribution from figure 3.1.10.

Five separate channels

To optimise each channel, the flow field was simulated with five separate inlets, illustrated in figure 3.1.11 where the inlets are on the left side and channel 1 is on the top, the same applies to the sub channels. The simulation was performed at a flow rate of up to 50g/min per channel, where the results are given in table C.8.1. From the values obtained in table C.8.1, the flow rate in the sub channels is presented in table 3.1.6 and shown in figure 3.1.12, while the pressure drop over the channels is shown in figure 3.1.13.

Figure 3.1.11 shows the velocity field in the channels of the final design, where the first channel has a dark blue area above the sub channels, which indicate low or no velocity.



Figure 3.1.11: Velocity field of the channels in the final design at 50g/min per channel. Dimension specified in figure A.6.1

From table 3.1.6, channel 4 has the worst distribution were the difference between sub channel 1 and 5 is 0.7g/min.

Table 3.1.6: Flow rate [g/min] in the sub channels and pressure drop [Pa] over the channels from figure 3.1.11, with a flow rate of 50g/min per channel.

Channel	Sub1	Sub 2	Sub 3	Sub 4	Sub 5	Pressure drop
1	9.42	9.84	9.57	9.76	10.09	709
2	9.93	9.84	9.46	9.65	9.80	725
3	9.62	9.76	9.58	9.75	9.97	717
4	9.36	9.81	9.69	9.78	10.06	709
5	9.40	9.80	9.85	9.86	9.77	704

In figure 3.1.12, the graphs display the flow rate in the sub channels as a function of the simulated flow rate. In channel 4 and 5 the flow rate in sub channel 1 starts to decrease from a factor of 0.6, while channel 1 has a wider consisting spread.

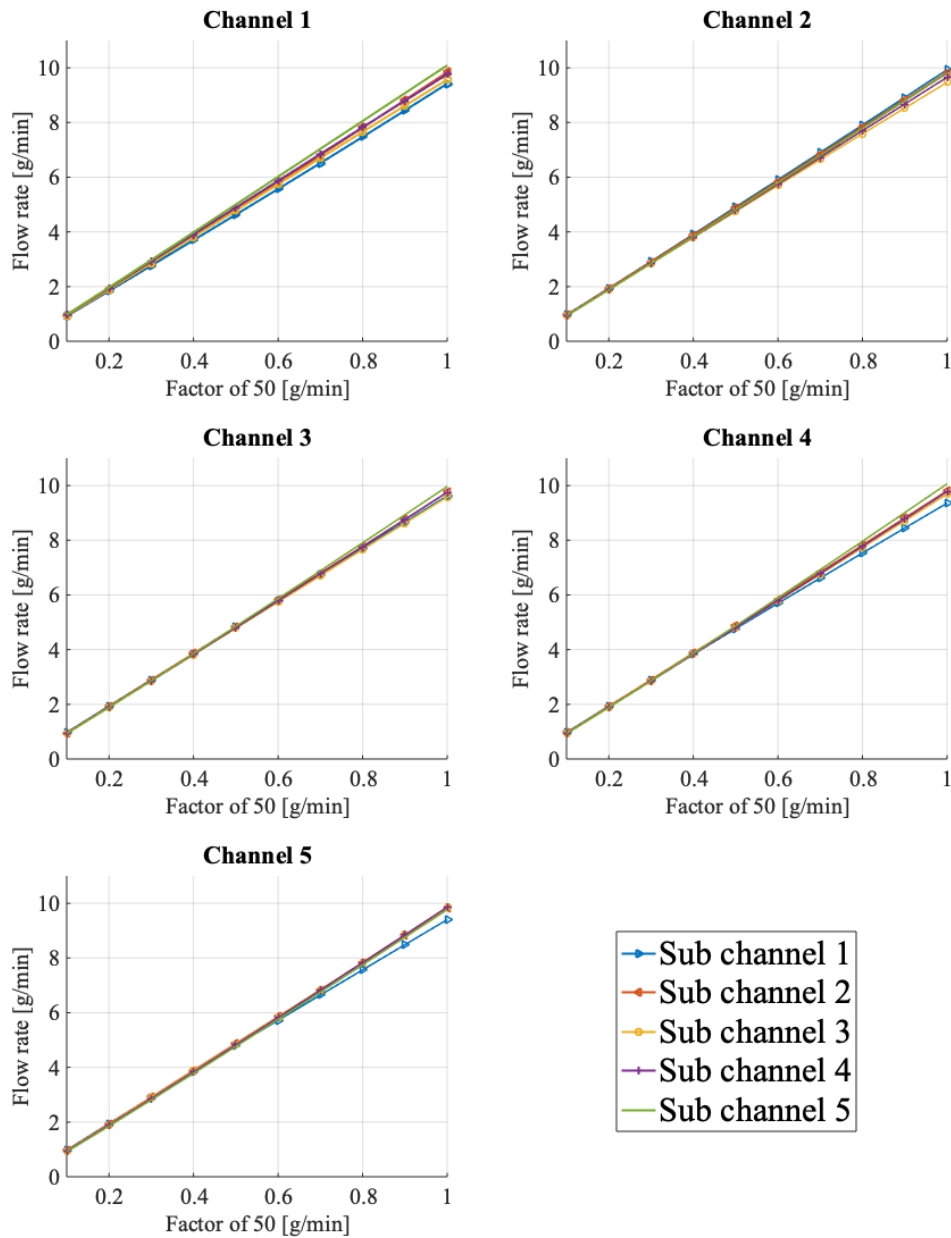


Figure 3.1.12: Flow distribution in the channels shown in figure 3.1.11, displaying the flow rate in every sub channel as a function of the simulated flow rate.

Figure 3.1.13 shows the pressure drop over each channel as a function of the simulated flow rate. The increase in flow rate has an ever increasing pressure drop over the channels, where channel 2 has the highest pressure drop, then followed by channel 3.

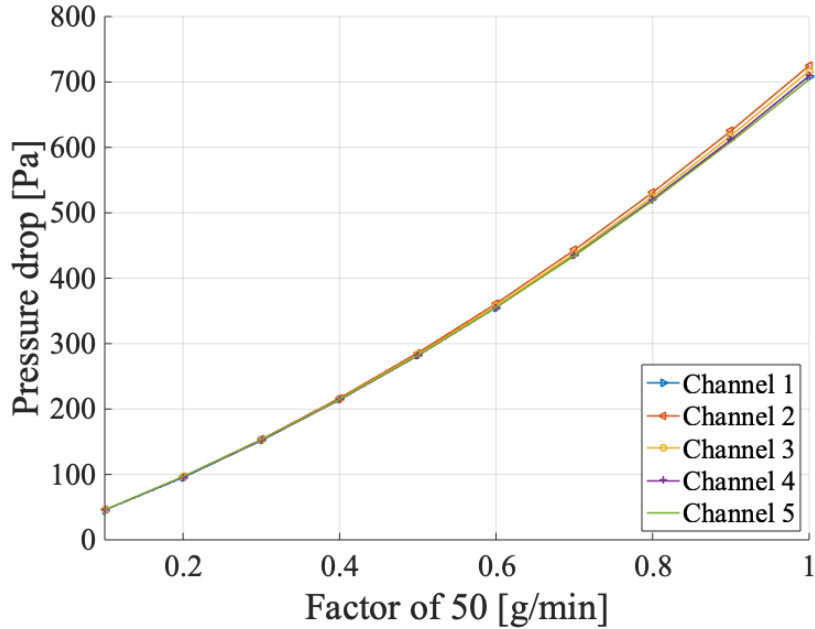


Figure 3.1.13: Pressure drop over the different channels in figure 3.1.11 of up to 50g/min per channel.

To see how the flow field performed from the wrong side, a simulation with 50g/min per channel were tested from the outlet side. In figure 3.1.14, the velocity field from the simulation illustrates how the flow would be distributed. From the figure, the velocity in the first sub channel from the outlets are much lower than the rest.

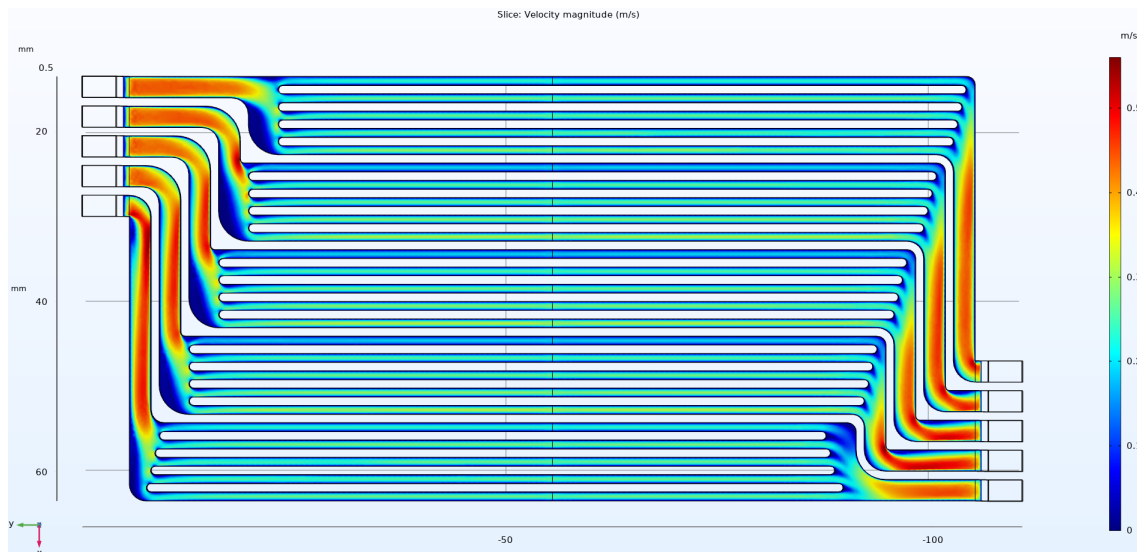


Figure 3.1.14: The final flow field reversed with 50g/min per channel from the outlets on the left side.

Stack with one flow field

To see if the flow distribution between the channel was even, a simulation of the flow field with one inlet was performed (see figure C.8.2). The simulation was with a flow rate of up to 250g/min, the results is given in table C.8.4 and showed as flow rate per channel in figure 3.1.15 and table 3.1.7 with the pressure drop over the simulated model.

In figure 3.1.15 the flow rate in the sub channels is combined as the total flow rate in the channels. From the graph, channel 2 and 3 has a slightly lower flow rate, while channel 1 and 5 has the highest flow rate. Table 3.1.7 gives the values from the simulation, where the difference between channel 1 and 2 is 1.38g/min at a simulated flow rate of 250g/min.

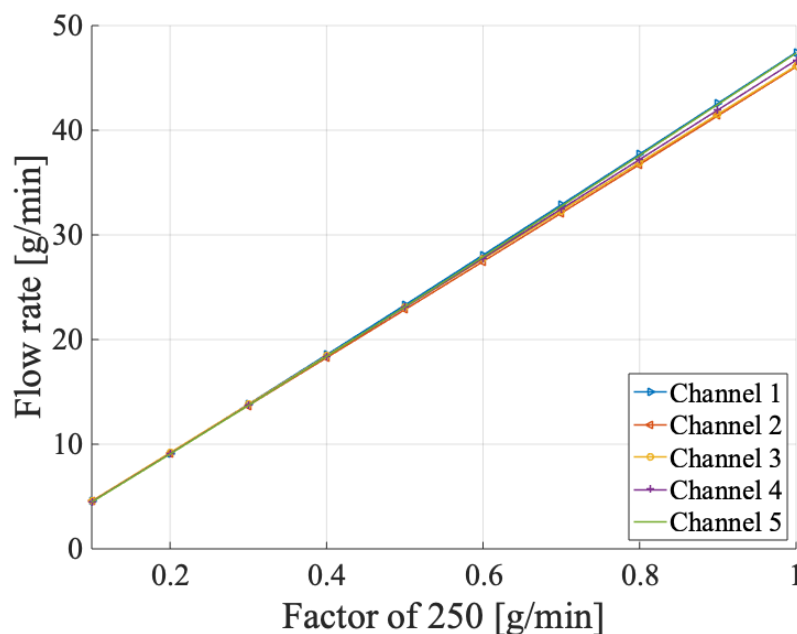


Figure 3.1.15: Flow distribution in the channels with a single inlet of up to 250g/min

Table 3.1.7: Flow rate [g/min] in the channels from figure 3.1.15 and pressure drop [Pa] over the flow field.

Flow rate [g/min]	Ch 1	Ch 2	Ch 3	Ch 4	Ch 5	Pressure drop
0.2/50	9.15	9.11	9.19	9.09	9.05	108
0.4/100	18.55	18.26	18.44	18.39	18.39	254
0.6/150	28.08	27.46	27.69	27.77	27.91	438
0.8/200	37.72	36.72	36.92	37.20	37.59	660
1.0/250	47.44	46.06	46.16	46.69	47.36	920

Since the simulated water at 20°C vary from the 1M KOH solution used under operations, a simulation was performed on the final flow field with both water and 1M KOH at 60°C. The density of water and 1M KOH at 60°C are 983kg/m³(figure C.9.2) and 1034kg/m³(figure C.9.3), respectively, where the results from the simulations are given in table C.8.2 and displayed in table 3.1.8. From pressure readings in table C.8.2, the pressure drop over the model were 932Pa with water and 695Pa with KOH.

In table 3.1.9, the flow rate in the sub channels for 1M KOH at 60°C and Water at 60°C are displayed and compared with water at 20°C (values from table C.8.4). There are similar trends between water and KOH, where the flow rate vary more with 1M KOH with a the difference in channel 4 at 1.25g/min between sub channel 1 and 5.

Table 3.1.8: Flow rate [g/min] in the final flow field with one inlet at 250g/min for different solutions.

Channel	Flow rate [g/min]				
Water 20°C	Sub 1	Sub 2	Sub 3	Sub 4	Sub 5
1	9.32	9.70	9.28	9.32	9.81
2	9.54	9.18	8.89	8.99	9.45
3	9.12	9.21	9.05	9.24	9.53
4	9.05	9.31	9.24	9.40	9.68
5	9.21	9.56	9.47	9.56	9.56
Water 60°C	Sub 1	Sub 2	Sub 3	Sub 4	Sub 5
1	9.33	9.73	9.29	9.35	9.82
2	9.54	9.14	8.88	9.02	9.46
3	9.07	9.22	9.06	9.26	9.51
4	9.04	9.32	9.26	9.40	9.68
5	9.22	9.55	9.49	9.56	9.57
1M KOH 60°C	Sub 1	Sub 2	Sub 3	Sub 4	Sub 5
1	9.69	10.24	9.24	9.25	9.94
2	9.77	9.16	8.77	9.11	9.80
3	9.12	9.16	8.93	9.29	9.79
4	8.93	9.33	9.25	9.60	10.18
5	8.99	9.66	9.68	9.93	10.06

Complete stack with three flow fields

A simulation on three flow fields connected to the same inlet and outlet was performed (see figure C.8.3, to simulate the complete stack and see the distribution among the different cells. The simulation was with a flow rate of 150g/min and 300g/min, where the results are given in table C.8.5 and presented as flow rate in the flow field and pressure drop over the stack in table 3.1.9. From the table, the bottom flow field have the highest flow rate, which is 1.92g/min higher than the top flow field.

Table 3.1.9: Flow rates for the different flow fields in the stack and pressure drop over the stack.

Simulated flow rate	Total flow rate [g/min]			Pressure drop [Pa]
	Flow field top	Flow field mid	Flow field bot	Stack
150 g/min	45.27	45.59	45.93	128
300 g/min	91.10	92.09	93.02	319

3.2 Structural mechanics simulation

The results from the structural mechanics simulations first presents the force needed on each bolt for the 1.8mm gasket displacement, followed by the horizontal expansion and deformation of the gaskets, illustrated as volume plots. Then, the von Mises stress occurring on different stack components from the compression and operating pressure are presented, also as volume plots. The von Mises stress are compared with the minimum value of the component material tensile strength, to estimate the Margin of Safety.

3.2.1 Gasket compression

The graph in figure 3.2.1 shows the displacement vs a factor multiplied 100N. The computations show a force between 115-120N, on each bolt, to compress the stack 1.8mm.

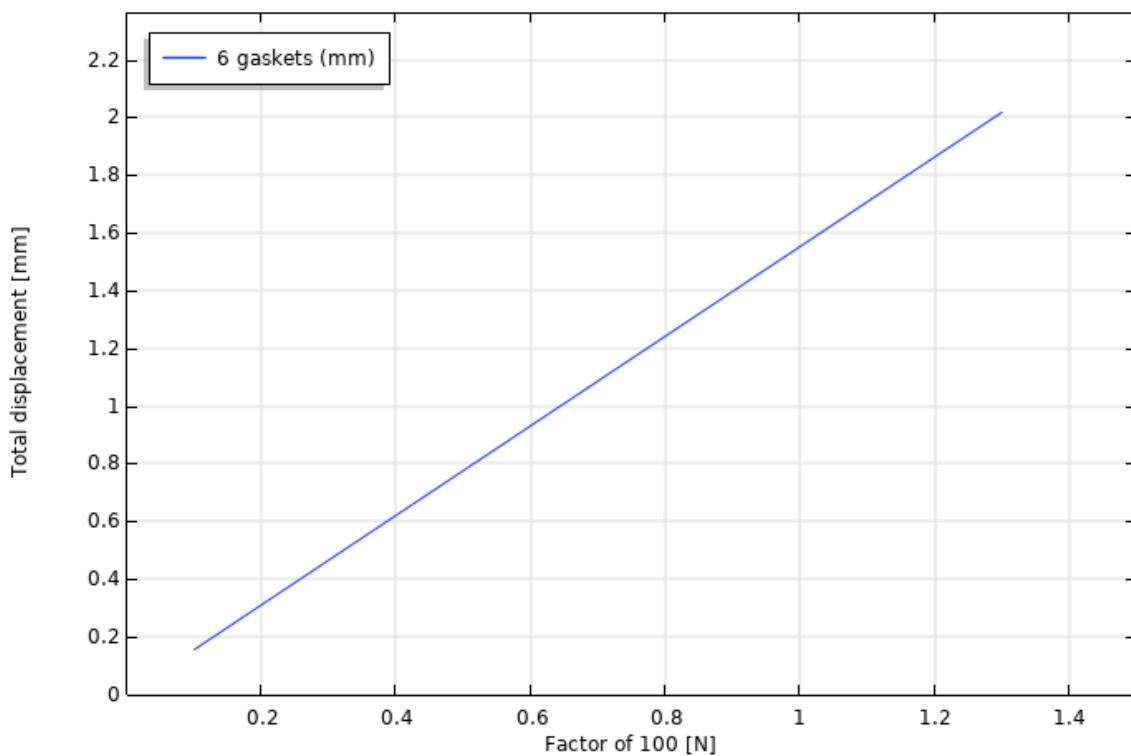
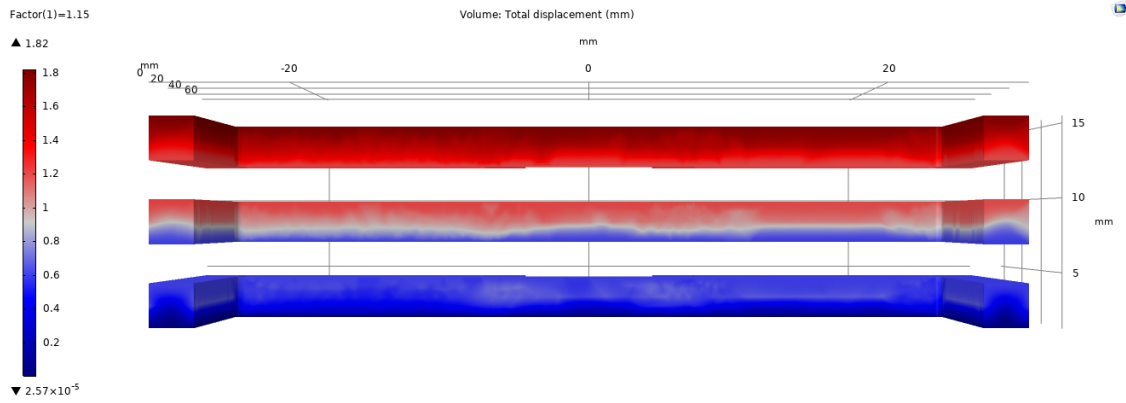
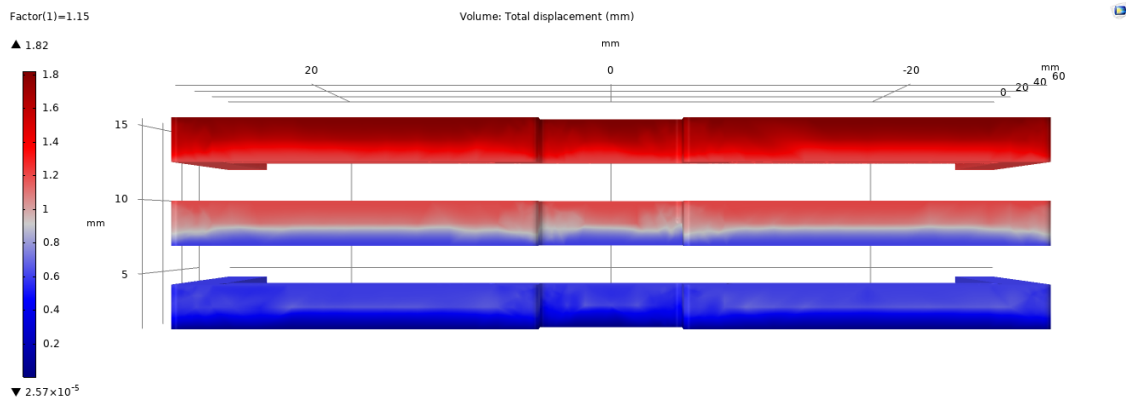


Figure 3.2.1: Gasket displacement graph.

Two and two gaskets are paired on top of each other in the stack, forming three layers, one for each cell. This is illustrated in figure 3.2.2a and 3.2.2b, where the colour legend describe the vertical displacement of each point, in millimetre. The deformation of the gaskets was also simulated, as shown in figure 3.2.3a and 3.2.3b.



(a) Inside



(b) Outside

Figure 3.2.2: Compression simulation, 115 [N] per bolt: Gasket displacement

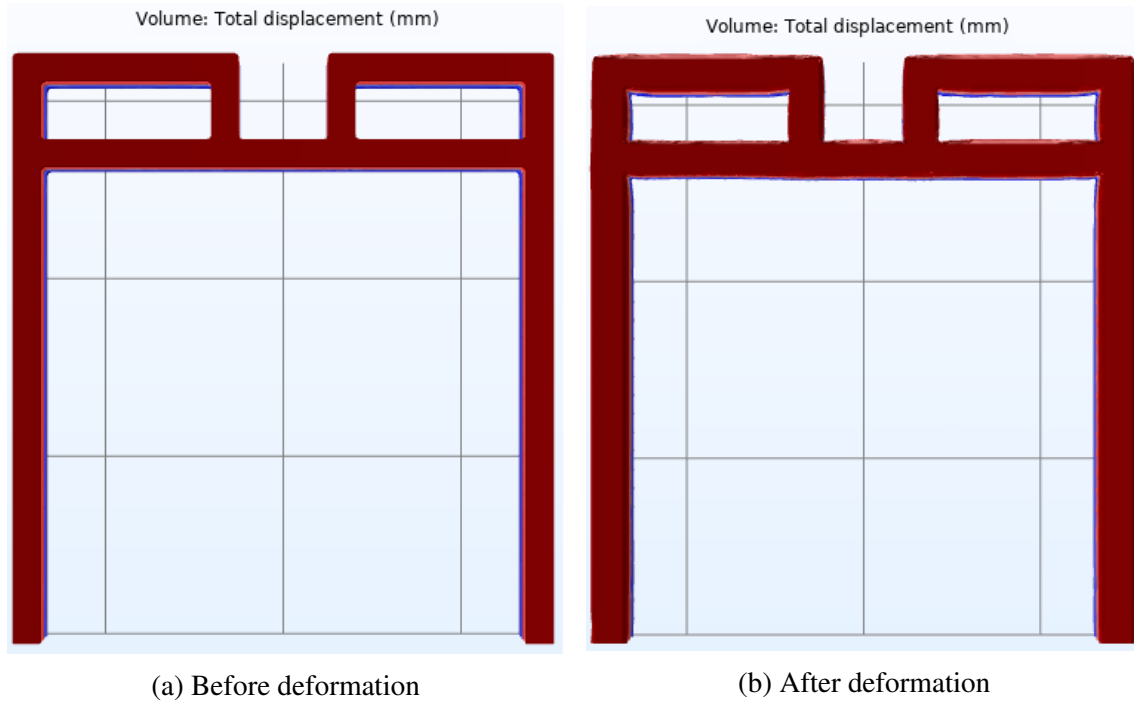


Figure 3.2.3: Compression simulation, 115N per bolt: Gasket deformation from above.

Then calculations of the displacement in y-direction (figure 3.2.4a) and x-direction (figure 3.2.4b) were made.

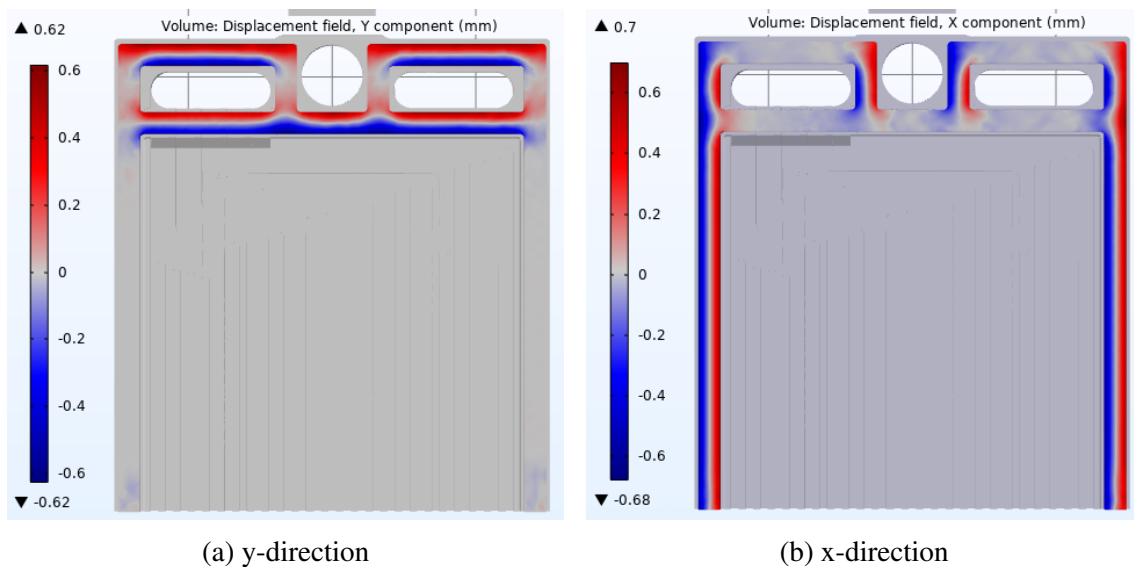


Figure 3.2.4: Compression simulation, 115 [N] per bolt: Gasket displacement, x- and y-direction from above.

All of these computations made an idea of how much space was needed for the gasket to expand on the flow field plates, without affecting other components.

3.2.2 von Mises stress

The von Mises stress simulations gives an insight on the stress impact on individual components, and an indication if the component will yield or not. The von Mises stress simulation results will be used to calculate the Margin of Safety for component yielding evaluation.

Gasket simulation

The von Mises stress in the gasket was found to see if the gaskets could handle the compression and pressure under operation. Figure 3.2.5 illustrates the von Mises stress in one cell with two gaskets that was compressed 0.6mm in figure 3.2.5a and with 5Bar applied on the inside in figure 3.2.5b. From the figures, the stress on the gaskets is located at the edges, where the highest points are in the corners. The highest value of von Mises stress is seen in figure 3.2.5b, where a value of 2.64N/mm^2 is reached.

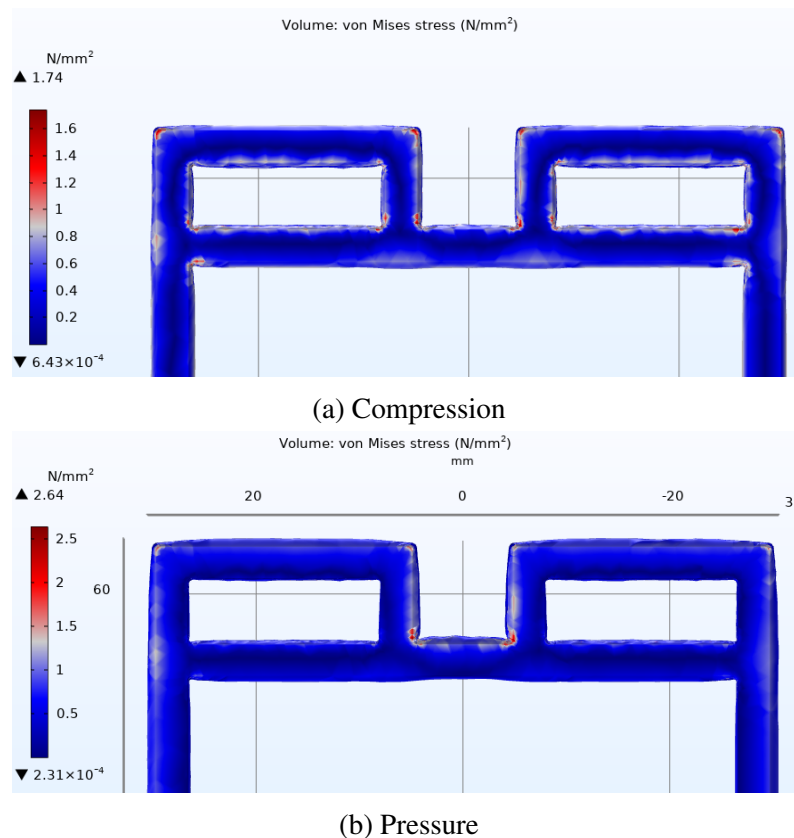


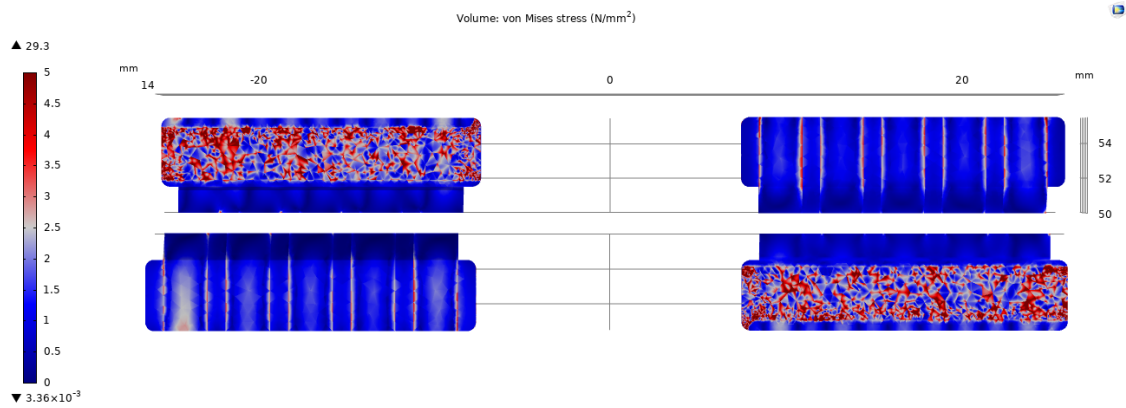
Figure 3.2.5: Von Mises stress in two gaskets at 0.6mm compression in (a) and including a pressure of 5Bar on the inside in (b).

Comparing the tensile strength of the gasket material from appendix B.3 with the von Mises stress simulations of the gasket leads to a MoS of equation 3.2.1

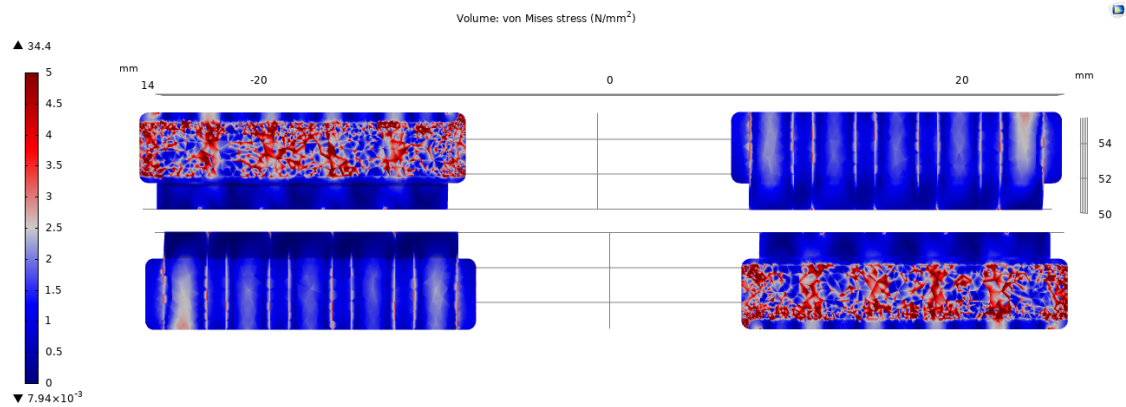
$$MoS = \frac{(7 - 2.64) \frac{N}{mm^2}}{2.64 \frac{N}{mm^2}} = 1.65 \quad (3.2.1)$$

Bridge simulation

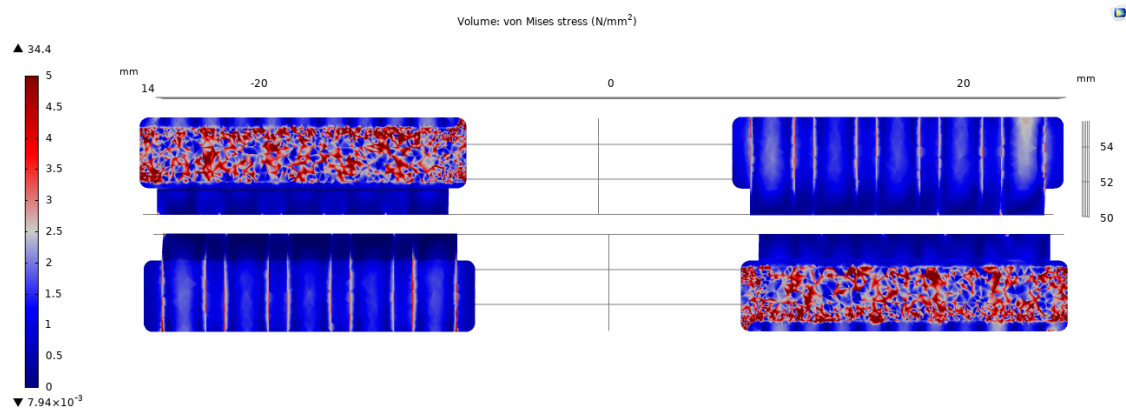
Figure 3.2.6 (a), (b) and (c) shows the upward turning bridges of the half cell stack, on the left side, and the down turning on the right side. The bridges are turned on the illustration below the upper one, to get a view on the stress occurring from the ribs. The legends shows the von Mises stress in N/mm^2 .



(a) Top cell, left and right bridge



(b) Middle cell, left and right bridge



(c) Bottom cell, left and right bridge

Figure 3.2.6: Compression simulation, 115 [N] per bolt: von Mises stress on the bridges of the three cells.

The computations indicates that almost all of the stress lies between 0- and $5N/mm^2$. The highest stress is concentrated in small points on the components.

Having the von Mises stress maximum value of 34.4N/mm^2 compared with the material properties of Inconel 625 Alloy in appendix B.2 leads to a MoS value of equation 3.2.2.

$$MoS = \frac{(460 - 34.4)\frac{N}{mm^2}}{34.4\frac{N}{mm^2}} = 12.37 \quad (3.2.2)$$

Chapter 4

Discussion

The first part of the discussion presents different computations done by simulations. Optimising the flow field of the flow field plates are made a priority of this thesis, and will be the largest part of the discussion. For the assembling and compression of the AEMWE stack, Structural Mechanics simulations have been performed, to compute gasket displacement, stress and strain due to the stack compression.

The second part of the discussion focuses on different construction solutions, reducing stack size and material usage.

4.1 Flow field simulations

The flow field is an important part of the AEMWE stack, where the optimisation of the flow field could improve cell performance. By designing a flow field that have a uniform flow distribution over the active cell area, the circulation of reactants and products can be more efficient.

In real life, there would be a two phase flow of gas bubbles and water solution in the electrolyser. Two phase computation is complex and would require both time and advanced computers to simulate. Instead, a single phased laminar flow of liquid water was used to simulate the flow over the flow field. By doing this simplification, the implication of the gas bubbles on the flow field will not be accounted for, which may lead to deviations from the simulated results. However, by designing a flow field that has an even distribution of water, the pressure drop for the different channels should be equal, which may result in a similar distribution for the two phased flow.

4.1.1 Choosing a flow field pattern

When determining the flow field pattern, two of the common flow field patterns were compared, the serpentine and the straight flow field (see figure 1.5.3). The straight flow field has shorter paths and thus lower pressure drop compared to the longer channels in the serpentine, which also has more bends. Since the flow tends to choose the easiest path, some channels may have low or no flow. From the slug formation in the flow fields (see figure 1.5.4), the serpentine flow field would tend to accumulate more gas bubbles, thus blocking more of the active cell area for new reactants. This may not be desirable for an electrolyser. Therefore a starting point was taken with a straight flow field.

The simulations in section 3.1.1 was taken with a coarse mesh and relatively low flow rate at 50g/min, which may be due to personal computer limitations. This may affect the results, but these simulations were done to get an overview of major differences between

the flow patterns, where a finer mesh may not be necessary. Although the flow rate was relatively low, this gave an indication of how the flow was distributed over the flow field, where a higher flow rate would probably have made these differences clearer.

From the simulations, the basic straight flow field has relative high pressure drop (see figure 3.1.1a), where the centre channels have little to no flow. By modifying the inlet region with a larger open area (see figure 3.1.1b) the pressure drop is reduced from 343Pa to 212Pa, while the distribution appears to be better. But this open area would have less rib contact for the PTL, which may reduce the support of the MEA.

In the five channel patterns, with horizontal and vertical inlet/outlet sections (see figure 3.1.1c and figure 3.1.1d), the flow appeared to be evenly distributed among the channels, while having an uneven distribution between the sub channels. Since the channels divide the flow field into sections, the changes can be more concentrated, which should make it easier to optimise. The channels from the inlet to the sub channels can be a downside of the five channel flow fields, where the channel to rib width can be too much in favour of the channels, which will increase the contact resistance between the ribs and PTL in this area. However, these larger channels also result in a lower pressure drop from the inlet to the sub channels, which may be preferable.

By using horizontal inlets/outlets, the channels would have a similar design but less corners, which can reduce the pressure drop increasingly at increasing flow rate, compared to the vertical inlet/outlet which also has some variation in the channels. But, with horizontal channel inlet/outlet, the flow field plate width increases, which would account for more material usage between the inlets/outlets when making the plates, especially for mass production.

4.1.2 Centre channel optimisation

Since there was little difference between the five channel flow fields, the flow field with vertical inlet/outlet that required less material, was chosen to be optimised. By isolating a channel in the flow field, the simulations in section 3.1.2 could be performed with the same flow rate of 50g/min in one channel, which was like testing the entire flow field at 250g/min. This increase amplified the effect from channel changes, which made it easier to see differences. But the smaller colour differences in the sub channels were still difficult to distinguish, where the colour changed depending on the computer screen and image size. Instead, the flow distribution was compared by the average velocity readings in the cross section of the sub channels.

The method of comparing the flow rates should be better than just looking at colour differences, where the accuracy of the measure will depend on the mesh fineness. This is due to the calculation method used in CFD, which is solved by assuming linearity in the mesh elements. The number of areas the mesh divides the cross section into (see figure 2.4.1), will therefore determine the number of values used to find the average velocity, thus affecting the accuracy of the measurements. Since models were simulated with the same mesh size, the simulations should be comparable.

The simulations in section 3.1.2 were performed on the centre channel of the flow field

in figure 3.1.1d. This channel was made of one half, which made the inlet and outlet side identical, where this can be regarded as the average channel of the flow field. The optimal design for the centre channel would not necessarily be the optimal solution for the rest of the flow field, but can be used as a starting point.

From the basic design of the channel (see figure 3.1.2a), the favoured sub channel was the one furthest away from the inlet and closest to the outlet, where the flow rate in the sub channels towards the inlet gradually decreases. This may indicate that the channel distribution is determined more by the exit point, than the entrance point in the channel. Therefore, modifications on the design should be made to evenly distribute the flow.

Restricting the sub channels with different rib lengths (see figure 3.1.2c) may contribute to a more even flow distribution to the sub channels, but, when doing this on a flow field with identical inlet/outlet channels, the restrictions done on the inlet side will affect the opposing sub channel on the outlet side. When making a restriction on sub channel 5, for instance, to get a higher flow distribution towards sub channel 1, the restriction also happens at the outlet on sub channel 1. Due to the restriction also occurring at sub channel 1, the flow distribution does not get improved. This also applies when rounding the corner to sub channel 1 (see figure 3.1.2i), making less restrictions for the flow on the inlet side, it also makes less restrictions for the flow in sub channel 5 on the outlet side. By using an incline to the sub channels 3.1.2f), the flow rate in sub channel 1 was increased, while the flow rate in sub channel 5 seemed unaffected. This limits the optimisation of identical inlet/outlet channel flow fields, designed to have flow distribution from either way.

By reducing rib length at the sub channel interconnections (see figure 3.1.2d and 3.1.2e), there would be more area for the flow to distribute over the sub channels. This improved the distribution in sub channel 2-5, while sub channel 1 got worse. This also increased the low flow zones over the sub channels on the inlet side, where gas bubbles can accumulate and block the flow. These low flow zones were reduced by increasing the bend and corner radius that made the fluid flow more easily through the channel (see figure 3.1.2b, 3.1.2g, 3.1.2h and 3.1.2j). This also reduced the pressure drop across the channel with relatively low change in the flow distribution.

The simulations showed that by optimising the flow field, the flow distribution was improved from 2.96g/min between sub channel 1 and 5 to 1.18 g/min, which resulted in 34.7% to 12.6% more flow in sub channel 5, respectively. This also reduced the pressure drop with 255Pa (see table 3.1.2). The flow still tends to prefer the sub channels closest to the outlet.

4.1.3 The effect of the channel depth

The channel depth of the flow field depends on the thickness of the flow field plates, where the manufacturing method and the design of whether the flow field is on one side, or both, limits the depth. With the traditional way of CNC-milling the flow field on the field plates, the channels could be made as deep as the cutting tool allow. Another manufacturing method is to stamp the plates into shape, which can create thinner plates to reduce weight and volume of the stack. If the goal is to make thinner plates, the channel depth should be made accordingly.

To see the effect that channel depth has to the pressure drop and flow distribution, a single channel were simulated with different depths at the same flow rate of 50g/min (see figure 3.1.3)). From the pressure computations given in table C.3.1, both the maximum and minimum values are listed, which is the pressure at the inlet and outlet, respectively. The boundary condition at the outlet was set to ambient pressure, where the pressure at the outlet would have been zero if the simulation reached the specified boundary conditions. This were achieved at lower flow rates, while for higher flow rates the values became negative. The negative values are relatively similar for the different depths, even though the inlet pressure varies more.

In CFD, the simulation run until the difference between the last and previous calculation is lower than an error limit. At this point, the simulation converges to a solution, where the solution should have reached the set boundary conditions. But this can be difficult to achieve, and the solution can vary from the specified boundary conditions, where the difference can be an indication of how much the solution deviates from the final solution. This may explain why there are negative values, but since they are similar, comparison of the different simulations should give valid results. The pressure readings from the different centre channel design were also relatively similar (see table C.2.1), where one channel stood out, channel C10. This channel was the only one that had a larger inner radius in the bend (see figure 3.1.2j). By increasing the inner radius, the flow should go easier through bends, which should lead to a more controlled streamlined flow out of the bend. Having a more controlled flow near the outlet may be the reason the simulation came closer to the set boundary condition, at the outlet.

From the graph in figure 3.1.4, the pressure drop is ever increasing with the flow rate. This can be explained by equation 1.5.1 where the pressure drop is depending on average velocity squared, where increasing the flow rate will cause more fluid to pass through the channel, thus leading to higher flow velocity. The pressure drop was also increasingly increased when the channel depth got smaller, which could also be related to the average velocity, where the same flow through a smaller channel must have a higher velocity to transport the same amount of fluid.

Even though the pressure drop over the channel changed with the depth, it seemed to have no effect on the flow distribution (see table 3.1.4). Thus, the channel depth should only be limited by the pump of the system, if it can handle the pressure drop, and the thickness of the flow field plate.

4.1.4 Inlet region

The inlet region is starting at the supply connection and ends when the reactants reaches the active cell area. In an electrolyser stack, several cells are fed from the same inlet, which means that the passage through the flow field plates must have the capacity to distribute reactants to all the flow fields. If the passage is too small, the pressure drop will increase and may hinder the reactants from reaching the flow fields furthest from the inlet.

Since the supply connection has a fixed dimension of 6.35mm in diameter, which is due to the connecting hose, this should be the part with the most friction of the inlet, the bottle-

neck. Making the passage through the plates with less friction than this should be enough for an even distribution to the flow fields. But the passage channel changes dimension between the cells and split into the different channels, which will increase the pressure drop. Therefore, the pressure drop across the passage channel should be much lower than the drop across the pipe dimension of the inlet.

The geometries used in the stack were simulated with straight models to compare the pressure drop of up to 250g/min, which is to deliver 50g/min to each channel in one flow field. But the pressure drop in straight channels can be relatively low for shorter lengths, so the models tested had a length of 1000mm, which is around ten times longer than the stack. This gave a better indication on the pressure drop differences for the different geometries (see figure 3.1.5), where the pressure drop difference between the supply pipe and passage duct increased with the flow rate, where the pipe had a much higher friction. The reason for this should be the cross section of the different areas, where the area of the pipe is smaller than the duct.

Due to the longer passage depth in the end plates, a cutting tool with the same dimension as the height of the duct at 5mm was used, which created the corners with a 2.5mm radius. To have a more consistent passage, the thinner flow field plates was also made with the same dimension. The effect this had was relatively low, with a small increase in pressure drop from a square duct. But this was still much lower than the friction from the pipe, where the passage should be large enough not to create a bottleneck in the inlet.

Connecting the inlet to the flow field

The bipolar plates made in this stack were created with flow field on both side of the same plate. This required a solution that could connect the different flow fields to the inlet passage, while being sealed from the other flow field. To do this, a bridge was designed to act as a support for the gasket and lay on top of the ribs to create channels under the bridge.

Two options were compared for the channels beneath the bridge, wider channels with lower height, or immersed channels that went up a ramp to the flow field (see figure C.5.1). The concepts were simulated at 10g/min and had both an inlet and outlet section (see figure 3.1.6), where the pressure drop for the dimensional change was around 70Pa and 50Pa with the ramp. Although these pressure values are low, the difference is relatively high.

By having wider channels with lower height, the inlet channels can be created on the same plane as the rest of the flow field, which would simplify the production. But the height of the channel is dependant on the bridge thickness, where the bridge must be thick enough to withstand the compression of the gasket and be at the same height as the rest of the plate. For a channel depth of 1.0mm, the bridge and channel depth have limited height, where lowering the channel depth will increase the pressure drop (see figure 3.1.4). Immersing the channels in the plate and connecting them with a ramp can allow the channel depth to be consistent, without reducing the thickness of the bridge. This will require a thicker flow field plate and is probably more demanding to produce. But since the bipolar plates are made with flow fields on both sides, the thickness should already be thick enough to lower the channels. For this design, the ramp seemed to be the better

solution.

Since the ramp were the preferred solution, several ramp designs were tested, where they went up 1.0mm in 1.0, 1.5, 2.0 and 3.0mm (see figure C.5.1). By increasing the ramp length, both the plate and bridge would have to compensate by increasing the length as well, which also meant longer channels from inlet to the flow field. The pressure drop over the ramps were similar, but the collection of contour lines on the shorter ramps indicated that the pressure drop was more focused in the ramp, while the longer channels had increased pressure drop because of the length (see figure 3.1.7). To further investigate the differences, the velocity field was compared for the different ramps (see figure 3.1.8), where the biggest change seemed to be between the ramp lengths 1.0-1.5mm, with little effect of increasing the ramps more. The 1.5mm ramp length was therefore seen as the most optimal to use on the flow field plates.

Width of the channels from inlet to the sub channels

Having an active flow field area of 50cm^2 lead to a flow field of $100 \times 50\text{ cm}^2$. First dividing the flow field into 25 sub channels and 25 ribs lead to one extra rib. Then dividing that 1mm rib into each sub channel left 25 sub channels of 1.04mm, and 24 ribs of 1mm.

In the five channel design, five separate channels distributes fluid to their five respective sub channels. The size of the channel should therefore be capable of delivering enough reactants to the sub channels, without requiring too much pressure force. Although a wider channel will be able to deliver more fluid at lower rate, it will also require more space in the flow field (see figure C.6.1).

The space usage of the flow field is important for the performance of the cell, where increasing the width will further favour the channels compared to the ribs, while the area of sub channels and ribs also is reduced. This area is the part of the flow field that has symmetry with the opposing flow field, where shorter ribs reduce the contact points that overlap with the other ribs to obtain a uniform compression of the cell.

To see the effect of the channel width, two flow fields were simulated at 50g/min, where one had 2.0mm channels and the other had 2.5mm channels (see figure 3.1.9), with a pressure drop of 215Pa and 171Pa, respectively. Both flow fields had ribs of 1.0mm, which made the inlet width larger for the 2.5mm flow field. This may have an effect on the pressure drop difference, but from the pressure drop across the duct geometry in figure 3.1.5, the pressure drop should be relatively small. Instead, the pressure drop difference appears to come from the channel width, where the velocity in the 2.0mm channel is higher (see figure 3.1.9a). The pressure drop may not be so high at this flow rate, but from the pressure drop readings for the varying depth in figure 3.1.4, a flow rate of 50g/min on the whole flow field will be the same as a factor of 0.2, where the pressure drop differences should increase for higher flow rates.

Even though the wider channel reduces the rib lengths, the pressure drop reduction may be necessary for the stack, where the pump may be able to reach higher flow rates. If the channels get too wide, they will also cover a larger region of the active area. Due to this, to not cover too much of the active area, there was set a channel width limit of 2.5mm.

4.1.5 Flow field with identical sides

Simulations on the whole flow field were more demanding for the computers, limiting the flow rates. By separating the channels with different inlets, each channel could be simulated with a flow rate of 50g/min simultaneously, which made it easier to see changes. But in doing so, the simulation would not show how the inlet flow was distributed between the channels.

Although this were an important part of the optimisation of the flow field, this method made it possible to measure the pressure drop over each channel. By comparing the pressure drop over the various channels, at the same flow rate, it can be assumed that the flow will choose the channel with the lowest pressure drop. From this, the channels were design with an optimal distribution among the sub channels, while having the pressure drop relatively similar.

Several simulations were performed with different changes to the different channels to optimise the flow field. But by designing a flow field that had the same inlet and outlet, where the flow could come from either way, had the same limitations as for the centre channels (see section 4.1.2).

By using the optimised centre channel design as a starting point (see figure C.2.1j), with the ramp design of 1.5mm (see figure C.5.1d) and a channel width of the 2.5mm (see figure C.6.1b) a flow field with a maximum difference of 1.5g/min between the sub channels in channel 4 was designed (see figure 3.1.10). This was the worst channel with 16.5% more flow in sub channel 5 compared to sub channel 1.

The changes that were made to the channels was relatively similar, except for the inlet section in channel 1 and the outlet section in channel 5, since these went straight to/from the inlet/outlet. Although the flow distribution in the channels was relatively uniform, each channel had a low velocity area above the sub channels on the inlet side, which may cause accumulation of bubbles.

4.1.6 Final flow field simulations

Channel distribution

Instead of going for identical channel design on the inlet/outlet channels, the channels were separately optimised with specific inlet- and outlet channel design. This made it possible to combine different concepts that did not work well for the previous flow field. The final flow field was optimised with the same simulation strategy used in section 4.1.5.

Since the flow tended to prefer the sub channels furthest away from the inlet, with a rising flow rate from sub channel 1 to 5, the channels could now be optimised by reducing the flow rate in some of the channels, while simultaneously increasing the flow rates in others. This made it possible to get better results with less change. With a channel depth of 1.2mm and the same ramp and channel width as used earlier (see section 4.1.5), the final flow field were able to reduce the difference between sub channel 1 and 5 in channel 4 down to 0.7g/min (see figure 3.1.11), with 7.5% more flow in sub channel 5. This is more than 50% distribution improvement from the channel in section 4.1.5.

In channel 2-5, the changes made were close to identical (see figure A.6.1), where the low flow zones above the sub channels also was removed. Channel 1 was the exception that required a different solution. This channel required more changes to both the inlet and outlet section of the channel, where the low flow zone still was above the sub channels at the inlet side. Due to production deadlines, models of the final flow field plates had to be delivered to the workshop, for CNC-milling. Removing the low flow zone would be more optimal for channel 1, preventing risks for bubble accumulation, but due to time limitations this was not completed. If the the five channel design with the horizontal inlet/outlet had been selected from the first simulations (see figure 3.1.1c), channel 1 would have been similar to the rest, where applying the same changes should have worked.

The pressure drop across the channels in the final flow field has very similar trends (see figure 3.1.13), where channel 2 has a slightly higher pressure drop, followed by channel 3. This may give an indication that channel 2 and 3 will have a slightly lower flow rate than the rest, when connected to the same inlet.

By simulating the final flow field from the outlet side (see figure 3.1.14), the distribution seems to be worse than for the basic design of which it was based on. This can be explained by the restrictions that were set on the best sub channels, now restricts the worst channels.

Flow field distribution

To simulate how the flow distribution in the channels of the final flow field was, a model of the inlet and outlet for the stack were created (see figure C.8.2). This was a simplification of the inlet path without the changes between the flow field plates, which would have made more disturbance in the flow. Since the point of the simulation was to find the distribution when combined to the same inlet, this did not matter.

When simulating on this model, the computation time went down, compared to previous simulations of flow field connected to the same inlet. Previous simulations had the inlet/outlet close to the channel entrances, where simulations struggle to find a solution, which could use multiple hours at higher flow rates, like 100g/min, without converging to a solution. In contrast, the new model with the inlet/outlet away from the entrances, could run a simulation at 250g/min at around the same time as testing the separate channels with 50g/min each. This may indicate that the simulation converges faster when the inlet/outlet regions are less disturbed from changes in the flow. But this was discovered later in the process, after the design was finished.

To find the flow rate in each channel, the flow rate in the sub channel was combined. From the simulation of up to 250g/min in the final flow field (see figure 3.1.15), the distribution between the channels were similar, where channel 2 and 3 had a slightly lower flow rate. This shows that the pressure drop over the channels from figure 3.1.13 would be a good indication of where the fluid would flow. The biggest difference in flow rate was between channel 1 and 2 with 1.38g/min, where channel 2 have 3.0% higher flow rate.

The flow rates obtained from the channels were lower than the simulated flow rate, where the difference increased relative to flow rate (see table 3.1.7). This is the case for all the simulations, where this may be the solution of the simulation that converges before the boundary condition is reached or that the mesh size is not optimal. It may also be that the calculation of the flow rate was done with values from appendix C.9.1 and not from COMSOL. But since the results were calculated the same way (see equation C.0.1), it would be correct relative to each other and should only give small differences.

The simulations with water used the standard temperature set in COMSOL at 20°C, while the operating environment for the electrolyser will be 1M KOH at 60°C. Since KOH was not listed in the program, it was added with values for density and dynamic viscosity, which was obtained from appendix C.9.2. This was simulated at 250g/min and compared with water at 60°C (see table 3.1.8). Water at 60°C still had relatively the same distributions as water at 20°C, while 1M KOH at 60°C had higher differences in the sub channels, where the highest was in channel 4 with 1.25g/min between sub channel 1 and 5.

The pressure drop was 695Pa for KOH and 932Pa for water at 60°C. From the material properties of 1M KOH (see appendix C.9.2) and water (see appendix C.9.1, the differences of density and dynamic viscosity was relatively small. This may be an indication that the results obtained from the KOH simulation are not valid.

Flow field distribution in the stack

In the last simulation, a model of three flow fields were connected to the same inlet to see how the distribution between them would be (see figure C.8.3). The stack model was simulated with 150g/min and 300g/min, which was like 50g/min and 100g/min per flow field. From this simulation, the simplification of the inlet between the flow field may lead to some variations from the results, where the dimensional changes between the flow field plates is not accounted for.

With the same trend as for channels, the flow tended to favour the flow field that was closest to the outlet (see table 3.1.9), which was the bottom one that had 1.92g/min more flow rate the top flow field, which is 2.1% more. This is a relatively low difference compared to the flow rate off 300g/min, but the stack has three flow fields, if more were added, the difference may increase.

4.2 Structural mechanics simulations

Stack compression is both for sealing, and making contact between components. The gaskets has to be displaced a certain length to be co-planar with the PTLs.

The compression of the gaskets may cause a number of problems. The structural mechanics simulations from Comsol Multiphysics are in an automatic form union relationship between stack components, that make all surface relationships act as a fixed constraint, having non slip conditions. This leads to the compression simulations of the gaskets being linear. In practice there will be friction between the two gaskets in each cell, and between

the gaskets and flow field plates. This causes a nonlinear compression, making the displacement and deformation harder to predict, expanding only from the middle of each gasket. Computing a non linear simulation requires large computing power, and having limited computing resources causes all simulations to be linear with non slip conditions.

Having an even and stable compression of the gasket is essential for sealing the electrolytic process, making the environment stable, and preventing blending of the different reactions occurring.

Results from figure 3.2.2a may show that the compression of the gasket will vary in the three cell layers. The centre lines of the gasket layers in the three cells are uneven, having more peaked centre lines towards the bottom cell. The displacement results of the top cell gasket are more evenly distributed over the two gaskets than the middle and bottom cell, showing a bigger and more uneven displacement in the lower gaskets.

Figure 3.2.2b and 3.2.3b, which shows the displacement and deformation of the gaskets, also suggests the gaskets having a larger displacement on the outward-facing corners of the gaskets, and a minimum on the inward-facing corners. The largest displacement seems to be on the outer surface of the gasket, where the vertical and horizontal gasket section around the flow field meet.

The dimensions of the bridge area may be too small, which opens the possibility for the gasket to expand into the inlet/outlet area. There are 0.6mm from the centred gasket to the inlet/outlet on the bridges, giving little room for over-exceeding the results from figure 3.2.4a. If the expansion does not over-exceed too much, it will not cause too much problems.

On the previous design of the flow field plates there were a gasket groove of 3.5mm (shown in figure A.2.2 appendix A.2). This groove was to shorten the displacement length, for the gaskets to be coplanar with the PTLs. Also, the groove made it easier to centre the gasket on the flow field plates, and left 0.25mm on each side of the centred gasket for expansion. The displacement simulation of the gasket shown an expansion of at least 0.6mm (figure 3.2.4), which would make the gasket expand onto the corners of the groove. It was then decided to remove the outer wall of the groove, and make an incline of 0.2mm towards the flow field (as figure A.2.1 in appendix A.2). This was to make room for the gasket expansion, and to make it easier for the CNC-milling.

Having the 0.2mm incline towards the flow field may also cause problems for the gasket compression, making the compression uneven. The incline is made to make a softer transition from the gasket groove, if it will expand further than the groove. There are 0.4mm from the centred gasket to the incline, the results from the simulations in figure 3.2.4 may indicate that the gaskets will expand into the incline. If this will be a problem or not is unsure, but having in mind that the incline is not very steep, or particularly wide, it is considered as a good solution, contrary the sharp edge on the 0.2mm groove.

To make the gaskets expand as planned, the gaskets must be centred as well as possible.

The von Mises stress simulations of the gaskets show a maximum value of 2.64 N/mm^2 . Compared to the material properties of the gaskets with a tensile strength of 7 N/mm^2 , gives a MoS of 1.65. This does not show signs of yielding caused by the stack compres-

sion. The form union function also here, cause the contact surfaces of components to have non-slip conditions. Since the gaskets were locked in place, it is uncertain if the friction between the flow field plates and the gaskets, created by the compression, is sufficient to keep the gaskets in place. As the simulations is not certainty, this has yet to be proven.

Results of von Mises stress and strain simulation on the bridges shows a maximum value of 34.4N/mm^2 at the middle and bottom cell. Comparing this with the tensile strength of 460N/mm^2 of Inconel 625 Alloy, results in a MoS of 12.37. Having in mind that the rule of a $\text{MoS} \geq 0$ is a structure with adequate strength for the applied load, this will not cause the bridges to yield, but the bridge being 0.8mm may still be too thin.

The von Mises simulations shows only microscopic concentrated points for the maximum values, which may indicate that they are caused by simulation errors. The average value of both the gaskets and bridges are far below the maximum value.

4.3 Stack components

4.3.1 End plate

Volume reduction

The end plates are the thickest component of the AEMWE stack. Reducing width and length of the end plates makes a significant difference in weight and material usage of both the end plates and stack assembly. Moving the centre bolt hole between the inlet/outlet area made a volume and material reduction of more than 18%, on each end plate, from the original design in figure A.1.1. Despite this, having two bolts through the stack may also lead to complications.

To make sure the end blocks are electrical insulated, the bolts through the stack section has to be electrical insulated. This means either having an electrical insulated material covering bolts of metal, requiring more space for the bolts, or having the bolts electrical insulated themselves. Previous testing and use of plastic screws have shown varying results, and there is often great wear on the threads, which means that the screws need to be replaced at more frequent intervals. The solution chosen for this project is to have the bolts electrical insulated, with a RENY plastic/glass fiber material. RENY material is known to be the strongest of all plastic materials, and are suitable as a metal substitute in many applications, as automobiles and construction, which may make them applicable for stack compression as well.

Gasket width

Placing the centre bolt hole between the inlets/outlets caused limitations of the gasket width. As seen i figure A.2.1 the length between the inlet/outlet- and centre bolt hole is 4.3mm, which limited the gasket width to 3mm total width. This leave 0.65mm for gasket expansion on each side of the centred gasket. The gasket could be thinner at this particular area, but to have as even compression as possible, the same length have been chosen for the whole gasket.

4.3.2 Flow field plates

Material selection

As the flow field plates are essential components of the stack assembly, the choice of material has to be carefully selected. For the material selection, SINTEF run a series of corrosion and ICR screening tests of different materials. Test results (figure 2.2.5) proved Inconel 625 Alloy to be the most applicable for this project, and electrolytic environment.

Current collector

Many electrolyzers are designed with a current collector unit, such as a current collector plate. In this design, the current terminals are attached to the unipolar plates, using the unipolar plates as current collectors. This reduces usage of material, cost, size and weight of the stack. The angle of the current collector connection to the unipolar plates are not optimised, which may lead to an uneven current distribution.

Anode/Cathode flow field

It is an identical flow field on the anode and cathode electrode of each cell in the AEMWE stack. Having in mind that the reactions occurring on each electrode are different, this may not be optimal. The distribution of products and reactants on each electrode differs, and may cause one side "drying out". There will be water/KOH distribution on each electrode, increasing the ionic conductivity and are contributing to prevent occurring of concentration gradients and drought.

If the flow fields are asymmetrical there might be an uneven division of rib and channel area, which will further on lead to uneven contact resistance. Having a symmetrical flow field pattern may provide more balanced current conduction, having the same contact resistance on each electrode.

Bridge

The bridge turned out to be a solution to several things. First off it started as a solution to reduce the flow field plate thickness. Making an immersion at the inlet/outlet area with an interconnected ramp to the flow field, made it possible to make the gasket groove at the same height as the flow field. This made it possible making 3mm thick bipolar plates. The bridge are used as support for the gasket across the inlet/outlet channel area, and as a flow channel limit, constraining the size and path of the inlet/outlet flow channels and the ramp section.

The incline towards the flow field, for the ramp section, are very thin, but this does not seem like a problem, according to the von Mises stress simulations.

This being a separate part from the flow field plates can lead to some complications during assembling, but may be solved by welding, or tape.

4.3.3 Stack assembly

Keeping gaskets and components steady during the assembling of the stack may be challenging. The dimensions of the stack components are relatively small, making the chances of error margins higher. The gaskets are cut by hand with a template and a scalpel, that also increase chances of margin errors, imperfections and uneven surfaces. The PTLs are

also cut by hand.

To support the stack assembling, the centre bolts will be used as guide pins for the flow field plates, and helical compression springs are used to keep the bolts centred. Still, there are 0.2mm on each side of the centre bolts, which means it does not keep the flow field plates locked in place, and leaves room for the plates to slip out of the centring.

Workshop

The final design of all components were delivered to the workshop in the end of March and beginning of April. Unfortunately the corona situation delayed the CNC-milling of the components until the middle of May due to urgent corona virus missions, at the workshop. Thus the practical tests of the AEMWE stack was delayed and will not be a part of this bachelor report.

Chapter 5

Conclusion

Fluid flow simulation

This study has shown how Computational Fluid Dynamics (CFD) can be used as a tool to analyse and optimise the flow distribution on a flow field. Single phase liquid water are used to simplify the simulation computations, due to limited computer resources. The computation time was greatly reduced when the simulated model had extended inlet and outlet.

A straight flow field pattern was chosen, based on the fact that the serpentine flow field pattern has a tendency to have more accumulation of gas bubbles. This may block the passage in the active cell area.

Simulations for both vertical- and horizontal inlets/outlets were computed, showing a lower pressure drop on the horizontal inlets/outlets. This may be on account of the horizontal design having less corners than the vertical design. The vertical inlet/outlet solution was chosen, based on the fact that the horizontal design caused a higher material usage.

Dividing the flow field into separate channels make the flow distribution more concentrated, and thus easier to optimise. The flow field was divided into 25 sub channels of 1.04mm, and 24 ribs of 1mm. Further on, the sub channels was divided into sections of five, with a larger channel distributing flow to the sub channels, from the inlet. Simulations of different channel widths showed that wider inlet channels lead to a lower pressure drop, but this would also take up space of the active cell area. In the final design, inlet channels of 2.5mm were chosen.

The inlet passage through the flow field plates was created with a 16.5x5mm square hole, with 2.5mm radius in the corners. This was to ensure that the pressure drop in the passage would not create a bottleneck for the distribution to the flow fields, preventing reactants to reach all of the flow field plates. The bottleneck of the AEMWE stack will be the 6.35mm diameter of the Swagelok tube fitting, connected to the end plate threads.

Both wider channels with reduced height, and immersed channels with a ramp was simulated as a solution to the bridge support. Having the wider channel with a distinctly higher pressure drop than the immersed channel, the immersed channel was preferred. Interconnecting the immersed area at the inlet-/outlet section to the flow field by a ramp, creates a continuous flow having a consistent channel depth, together with the bridge constraining the immersion channel from above. The ramp length selected was 1.5mm, after the computations from the flow simulations proved this to be optimal.

Results from simulations have shown that:

- The flow tend to favour the sub channel closest to the outlet, and is reduced in the sub channels towards the inlet.
- Low flow zones in the flow field can be discovered and removed to reduce areas for gas bubble accumulation.
- Reducing the depth of the channel have increasingly increased pressure drop, without affecting the flow distribution.

With identical inlet and outlet sides of the centre channel, the flow distribution in the channel was improved from 34.7% to 12.6% higher flow rate in the favoured sub channel compared to the worst. By using the centre channel as a starting point, less changes was required to the rest of the flow field. Results shows that a flow field with identical inlet and outlet sides has limited possibilities to optimise flow distribution and removing low flow zones, since it is optimised to operated in both directions. The worst channel in the flow field had a 16.5% higher flow rate in the favoured sub channel compared to the worst.

By designing inlet and outlet specified sides, the channel optimisation can be more direct, which lead to better flow distribution and less low flow zones from one direction. The worst channel in the flow field had a 7.5% higher flow rate in the favoured sub channel compared to the worst. This is a 50% distribution improvement from the channel in the flow field with identical sides. From individual simulating on the channels and optimising each channel with similar pressure drop, the distribution among the channels were optimised to a 3% higher flow rate in the preferred channel compared to the worst. This was chosen as flow field plate design, with a channel depth of 1.2mm to reduce pressure drop, where this give 0.6mm between the flow fields on the bipolar plates

Structural mechanics simulation

Computing the stack compression simulations with the form union function leave out the non-linearity of the practical compression. This brings higher uncertainty to the expansion and deformation computations of the gaskets. This can further lead to complications with the gaskets expanding into the inlets/outlets from the bridge area, and/or into the incline towards the flow field. Having the gaskets expanding into the incline may result in uneven gasket compression. The simulations further on showed a larger displacement at the outwards facing corners, and less displacement at the inward facing corners. The need of a good centring of the gaskets are essential to minimise over-expansion.

The results from the von Mises stress simulations does not show any signs of yielding on exposed components. Computations resulted in a MoS of 1.65 for the gaskets, and 12.37 for the most exposed bridges. The MoS is calculated with the maximum value of the von Mises stress on the components, even though the average values were much lower. Also in the von Mises stress simulations, the form union function between the stack components affect the results, especially the von mises stress simulations on the gaskets, having them with non-slip conditions on the contact surfaces.

Stack components

Placing the centre bolts of the stack assembly between the inlets/outlets made a significant volume reduction of more than 18%. The RENY bolts used through the centre holes are made of RENY material, which are seen as the most durable of all plastic materials. Still, there might be great wear on the threads, leading to more frequent replacement intervals.

The two centre bolts with passage through the stack assembly made restrictions for the width of the gaskets. It was chosen to have a gasket width of 3mm, for the whole gasket, to have as even gasket compression as possible.

The flow fields being identical at the anode/cathode electrode of each cell in the AEMWE stack may not be optimal. There is differ in reactants and products on each electrode, which may cause one side "drying out". As a solution to this, there will be water/KOH distribution on each electrode, increasing the ionic conductivity and prevention of occurring concentration gradients and drought. The symmetric flow field may also cause the current conduction between the stack components to be more balanced, having the same contact resistance on each side of the cell.

Screening tests proved Inconel 625 Alloy to be the most suitable material for the flow field plates of the AEMWE stack. This was based on Inconel being the material with lowest ICR increase after corrosion testing at two different compression pressures, it was also done a series of other tests. The immersion at the inlet/outlet area, and using bridges to support the gaskets during compression, reduces the thickness of the bipolar plates to 3mm. Reducing material usage, stack size and -weight are essential for up scaling. Other measures done for reducing stack properties is attaching the current terminals to the unipolar plates, and removing the outer gasket groove and the gasket groove around holes. Removing the outer gasket groove was particularly done to make room for gasket expansion, but also resulted in weight reduction, and making it easier and time saving for the CNC milling process.

It may be challenging to assemble the AEMWE stack components. Working with small components increase chances of margin errors. Having the gaskets cut by hand with a scalpel and a template may lead to imperfections and uneven surfaces on the gaskets. Even though the centre bolts work as guide pins, they have a clearance of 0.2mm on each side, not keeping the flow field plates in place. This leaves room for the plates to slip out of centring.

Delays at the workshop due to corona virus and urgent corona virus missions lead to delayed practical testing of the AEMWE stack. Thus there will be no practical stack testing in this bachelor report.

Bibliography

- [1] jlab. *10 Most abundant elements of the universe*. URL: https://education.jlab.org/glossary/abund_uni.html. (accessed: 20.05.2020).
- [2] G.W. Crabtree and M.S. Dresselhaus. “The Hydrogen Fuel Alternative”. In: *MRS Bulletin* 33.4 (2008), pp. 421–428. DOI: 10.1557/mrs2008.84.
- [3] Energy gov. *Fuel cell fact sheet*. URL: https://www.energy.gov/sites/prod/files/2015/11/f27/fcto_fuel_cells_fact_sheet.pdf. (accessed: 20.05.2020).
- [4] Immanuel Vincent and Dmitri Bessarabov. “Low cost hydrogen production by anion exchange membrane electrolysis: A review”. eng. In: *Renewable and Sustainable Energy Reviews* 81.P2 (2018), pp. 1690–1704. ISSN: 1364-0321.
- [5] Hydrogen Europe. *HydrogenEurope: Electrolysis*. URL: <https://hydrogeneurope.eu/electrolysers>. (accessed: 18.02.2020).
- [6] *Ion definition*. URL: <http://www.qrg.northwestern.edu/projects/vss/docs/propulsion/1-what-is-an-ion.html>. (accessed: 10.04.2020).
- [7] Aneeya Kumar Samantara and Satyajit Ratha. “Types of Electrolysis and Electrochemical Cell”. In: *Metal Oxides/Chalcogenides and Composites: Emerging Materials for Electrochemical Water Splitting*. Cham: Springer International Publishing, 2019, pp. 5–9. ISBN: 978-3-030-24861-1. DOI: 10.1007/978-3-030-24861-1_2. URL: https://doi.org/10.1007/978-3-030-24861-1_2.
- [8] Chemistry libretexts. *Unique Features of Aqueous Solutions*. URL: [https://chem.libretexts.org/Bookshelves/Inorganic_Chemistry/Modules_and_Websites_\(Inorganic_Chemistry\)/Descriptive_Chemistry/Main_Group_Reactions/Reactions_in_Aqueous_Solutions/Unique_Features_of_Aqueous_Solutions](https://chem.libretexts.org/Bookshelves/Inorganic_Chemistry/Modules_and_Websites_(Inorganic_Chemistry)/Descriptive_Chemistry/Main_Group_Reactions/Reactions_in_Aqueous_Solutions/Unique_Features_of_Aqueous_Solutions). (Accessed:27.04.2020).
- [9] Chemguide. *Reduction and Oxidation*. URL: <https://www.chemguide.co.uk/inorganic/redox/oxidnstates.html>. (accessed: 16.04.2020).
- [10] *Cell potential at different pH*. URL: <http://www1.lsbu.ac.uk/water/electrolysis.html>. (accessed: 08.04.2020).
- [11] W. Wang et al. “Electrochemical cells for medium-and large-scale energy storage: Fundamentals”. English. In: *Advances in Batteries for Medium and Large-Scale Energy Storage: Types and Applications*. Elsevier, 2015, pp. 3–28. ISBN: 9781782420224.
- [12] L. An et al. “Mathematical modeling of an anion-exchange membrane water electrolyzer for hydrogen production”. English. In: *International Journal of Hydrogen Energy* 39.35 (2014), p. 19869. ISSN: 0360-3199.

- [13] Frano Barbir. “CHAPTER 3 - Fuel Cell Electrochemistry”. In: *PEM Fuel Cells*. Ed. by Frano Barbir. Burlington: Academic Press, 2005, pp. 33–72. ISBN: 978-0-12-078142-3. DOI: <https://doi.org/10.1016/B978-012078142-3/50004-5>. URL: <http://www.sciencedirect.com/science/article/pii/B9780120781423500045>.
- [14] Luca Bertuccioli et al. “Development of water electrolysis in the European Union”. In: *Fuel cells and hydrogen joint undertaking 83* (2014).
- [15] “Renewable hydrogen technologies : production, purification, storage, applications and safety”. eng. In: Amsterdam: Elsevier, 2013. Chap. 2 Water Electrolysis Technologies. ISBN: 0-444-56361-X.
- [16] Alexander Buttler and Hartmut Spliethoff. “Current status of water electrolysis for energy storage, grid balancing and sector coupling via power-to-gas and power-to-liquids: A review”. eng. In: *Renewable and Sustainable Energy Reviews* 82.P3 (2018), pp. 2440–2454. ISSN: 1364-0321.
- [17] Marcelo Carmo et al. “A comprehensive review on PEM water electrolysis”. eng. In: *International Journal of Hydrogen Energy* 38.12 (2013), pp. 4901–4934. ISSN: 0360-3199.
- [18] Alaa Faid et al. “Highly Active Nickel-Based Catalyst for Hydrogen Evolution in Anion Exchange Membrane Electrolysis”. eng. In: (2018). URL: <http://hdl.handle.net/11250/2586987>.
- [19] Yongjun Leng et al. “Solid-State Water Electrolysis with an Alkaline Membrane”. eng. In: 134.22 (2012), pp. 9054–9057. ISSN: 0002-7863.
- [20] Ji Eun Park et al. “High-performance anion-exchange membrane water electrolysis”. eng. In: *Electrochimica Acta* 295 (2019), pp. 99–106. ISSN: 0013-4686.
- [21] Emily Cossar et al. “The performance of nickel and nickel-iron catalysts evaluated as anodes in anion exchange membrane water electrolysis”. eng. In: (2019). URL: <http://hdl.handle.net/11250/2634421>.
- [22] Cho Min Kyung. “A Review on Membranes and Catalysts for Anion Exchange Membrane Water Electrolysis Single Cells”. In: *J. Electrochem. Sci. Technol* 8.3 (2017), pp. 183–196. DOI: 10.5229/JECST.2017.8.3.183. URL: <http://www.jecst.org/journal/view.php?number=97>.
- [23] Enapter. *AEM Electrolyser EL 2.1*. URL: <https://www.enapter.com/electrolyser>. (Accessed:06.05.2020).
- [24] Rajindar Singh. “Chapter 1 - Introduction to Membrane Technology”. In: *Membrane Technology and Engineering for Water Purification (Second Edition)*. Ed. by Rajindar Singh. Second Edition. Oxford: Butterworth-Heinemann, 2015, pp. 1–80. ISBN: 978-0-444-63362-0. DOI: <https://doi.org/10.1016/B978-0-444-63362-0.00001-X>. URL: <http://www.sciencedirect.com/science/article/pii/B978044463362000001X>.
- [25] Jude O Majasan et al. “Effect of Microstructure of Porous Transport Layer on Performance in Polymer Electrolyte Membrane Water Electrolyser”. eng. In: *Energy Procedia* 151 (2018), pp. 111–119. ISSN: 1876-6102.

- [26] Julio Cesar Garcia-Navarro K. Andreas Friedrich and Mathias Schulze. *Figure of the Porous Transport Layer*. URL: <https://advanceseng.com/gas-transport-porous-transport-layers-performance-proton-exchange-membrane-water-electrolysis/>. (Accessed:07.05.2020).
- [27] Robert Bock et al. “Measuring the thermal conductivity of membrane and porous transport layer in proton and anion exchange membrane water electrolyzers for temperature distribution modeling”. eng. In: *International Journal of Hydrogen Energy* 45.2 (2020), pp. 1236–1254. ISSN: 0360-3199.
- [28] H Ishikawa et al. “Effects of Pt and ionomer ratios on the structure of catalyst layer: A theoretical model for polymer electrolyte fuel cells”. eng. In: *Journal of Power Sources* 374 (2018), pp. 196–204. ISSN: 0378-7753.
- [29] Hiroshi Ito et al. “Investigations on electrode configurations for anion exchange membrane electrolysis”. eng. In: *Journal of Applied Electrochemistry* 48.3 (2018), pp. 305–316. ISSN: 0021-891X.
- [30] Sivakumar Pasupathi Bernard Bladergroen Huaneng Su and Vladimir Linkov. *Overview of Membrane Electrode Assembly Preparation Methods for Solid Polymer Electrolyte Electrolyzer*. URL: <https://www.intechopen.com/books/electrolysis/overview-of-membrane-electrode-assembly-preparation-methods-for-solid-polymer-electrolyte-electrolyz>. (Accessed:05.05.2020).
- [31] Marcelo Carmo and Detlef Stolten. “Chapter 4 - Energy Storage Using Hydrogen Produced From Excess Renewable Electricity: Power to Hydrogen”. In: *Science and Engineering of Hydrogen-Based Energy Technologies*. Ed. by Paulo Emilio V. [de Miranda]. Academic Press, 2019, pp. 165–199. ISBN: 978-0-12-814251-6. DOI: <https://doi.org/10.1016/B978-0-12-814251-6.00004-6>. URL: <http://www.sciencedirect.com/science/article/pii/B9780128142516000046>.
- [32] Xianguo Li and Imran Sabir. “Review of bipolar plates in PEM fuel cells: Flow-field designs”. eng. In: *International Journal of Hydrogen Energy* 30.4 (2005), pp. 359–371. ISSN: 0360-3199.
- [33] Chen-Yu Chen and Sheng-Chun Su. “Effects of assembly torque on a proton exchange membrane fuel cell with stamped metallic bipolar plates”. eng. In: *Energy* 159 (2018), pp. 440–447. ISSN: 0360-5442.
- [34] Barnwell. *What is a Gasket?* URL: <https://www.barnwell.co.uk/what-is-a-gasket/>. (Accessed:29.04.2020).
- [35] The Engineering Toolbox. *Gasket Characteristics*. URL: https://www.engineeringtoolbox.com/gaskets-properties-d_34.html. (Accessed:03.05.2020).
- [36] Apple Rubber. *What are Static Seals?* URL: <https://www.applerubber.com/hot-topics-for-engineers/what-are-static-seals/>. (Accessed:29.04.2020).
- [37] S Asghari, M Shahsamandi, and Mrashraf Khorasani. “Design and manufacturing of end plates of a 5 kW PEM fuel cell”. eng. In: *International Journal of Hydrogen Energy* 35.17 (2010), pp. 9291–9297. ISSN: 0360-3199. URL: <http://search.proquest.com/docview/901667931/>.
- [38] Omer F Selamet and M. Said Ergoktas. “Effects of bolt torque and contact resistance on the performance of the polymer electrolyte membrane electrolyzers”. eng. In: *Journal of Power Sources* 281 (2015), pp. 103–113. ISSN: 0378-7753.

- [39] “Fundamentals and performance of low temperature fuel cells”. eng. In: vol. no. 30. Polymer electrolyte membrane and direct methanol fuel cell technology ; Oxford: Woodhead Pub., 2012. Chap. 4 Gas diffusion media, flowfields and system aspects in low temperature fuel cells, pp. 92–97. ISBN: 0-85709-547-1.
- [40] Trygve Holtebekk. *viskositet*. URL: <https://snl.no/viskositet>. (accessed: 12.04.2020).
- [41] Yunus A Çengel. “Fluid mechanics : fundamentals and applications”. eng. In: 3rd ed. in SI units. Boston: McGraw-Hill, 2014. Chap. 8 Internal flow, pp. 348–358, 374–380. ISBN: 9781259011221.
- [42] *Laminar vs. Turbulent Flow*. URL: <https://www.cfdsupport.com/OpenFOAM-Training-by-CFD-Support/node334.html>. (accessed: 13.04.2020).
- [43] Store norske leksikon. *Reynolds’ tall*. URL: [https://snl.no/Reynolds’_tall](https://snl.no/Reynolds'_tall). (accessed: 09.04.2020).
- [44] Mohammad Ziauddin Chowdhury, Omer Genc, and Serkan Toros. “Numerical optimization of channel to land width ratio for PEM fuel cell”. eng. In: *International Journal of Hydrogen Energy* 43.23 (2018), pp. 10798–10809. ISSN: 0360-3199.
- [45] P Zhou, C.W Wu, and G.J Ma. “Contact resistance prediction and structure optimization of bipolar plates”. eng. In: *Journal of Power Sources* 159.2 (2006), pp. 1115–1122. ISSN: 0378-7753.
- [46] Jude O Majasan et al. “Two-phase flow behaviour and performance of polymer electrolyte membrane electrolyzers: Electrochemical and optical characterisation”. eng. In: *International Journal of Hydrogen Energy* 43.33 (2018), pp. 15659–15672. ISSN: 0360-3199.
- [47] COMSOL. *Navier-Stokes Equations*. URL: <https://www.comsol.com/multiphysics/navier-stokes-equations>. (Accessed:21.02.2020).
- [48] Yunus A Çengel. “Fluid mechanics : fundamentals and applications”. eng. In: 3rd ed. in SI units. Boston: McGraw-Hill, 2014. Chap. 9 Differential analysis of fluid flow, pp. 464–477. ISBN: 9781259011221.
- [49] SIMSCALE. *What are the Navier-Stokes Equations?* URL: <https://www.simscale.com/docs/content/simwiki/numerics/what-are-the-navier-stokes-equations.html>. (accessed: 16.04.2020).
- [50] The Engineering Toolbox. *Young’s Modulus - Tensile and Yield Strength for common Materials*. URL: https://www.engineeringtoolbox.com/young-modulus-d_417.html. (accessed: 08.04.2020).
- [51] *YOUNG’S MODULUS*. URL: <https://christoffphysics.weebly.com/youngs-modulus.html>. (accessed: 08.04.2020).
- [52] The Efficient Engineer. *Understanding Young’s Modulus*. Youtube. 2019. URL: <https://www.youtube.com/watch?v=DLE-ie0VFjI>. (seen: 08.04.2020).
- [53] The Engineering Toolbox. *Poisson’s ratio*. URL: https://www.engineeringtoolbox.com/poissons-ratio-d_1224.html. (accessed: 08.04.2020).
- [54] Roderic Lakes. *Meaning of Poisson’s ratio*. URL: <http://silver.neep.wisc.edu/~lakes/PoissonIntro.html>. (accessed: 08.04.2020).

- [55] The Efficient Engineer. *Understanding Poisson's Ratio*. Youtube. 2019. URL: <https://commons.wikimedia.org/wiki/File:PoissonRatio.svg>. (seen: 08.04.2020).
- [56] *Poisson's ratio*. URL: <https://upload.wikimedia.org/wikipedia/commons/e/ec/PoissonRatio.svg>. (accessed: 09.04.2020).
- [57] *von Mises stress*. URL: <https://www.simscale.com/blog/2017/04/von-mises-stress/>. (accessed: 08.04.2020).
- [58] *von Mises*. URL: https://www.researchgate.net/publication/272678959_Correlation_between_Engineering_Stress-Strain_and_True_Stress-Strain_Curve. (accessed: 09.04.2020).
- [59] NASA. *Margin of Safety*. URL: <https://ntrs.nasa.gov/archive/nasa/casi.ntrs.nasa.gov/20190032150.pdf>. (accessed: 18.05.2020).
- [60] *Siemens: Solid Edge*. URL: <https://media.plm.automation.siemens.com/solidedge/whitepages/Siemens-PLM-Solid-Edge-portfolio-br-75631-A18.pdf>. (accessed: 22.02.2020).
- [61] *Siemens: Solid Edge, Ordered and Synchronous environment*. URL: <http://support.industrysoftware.automation.siemens.com/training/se/en/ST3/pdf/spse01536.pdf>. (accessed: 08.04.2020).
- [62] *Siemens: Solid Edge, Student edition*. URL: https://www.plm.automation.siemens.com/plmapp/education/solid-edge/en_us/free-software/student. (accessed: 08.04.2020).
- [63] NBK1560. *Properties, plastic screws*. URL: <https://www.nbk1560.com/>. (accessed: 18.05.2020).
- [64] m-ep. *Usage of RENY bolts*. URL: <https://www.m-ep.co.jp/en/product/brand/reny/index.html>. (accessed: 18.05.2020).
- [65] Jim do free. *RENY material information*. URL: <https://plasticscrew.jimdofree.com/material-information/>. (accessed: 16.05.2020).
- [66] FIBRO. *Helical compression spring datasheet*. URL: <https://www.fibro.de/en/standardparts/downloads/pdf-downloads/springs-gas-springs/>. (accessed: 16.05.2020).
- [67] Per Egil Andresen (TTP seals). private communication. 2020.
- [68] NTNU. *Comsol Multiphysics, software information*. URL: <https://innsida.ntnu.no/wiki/-/wiki/English/Comsol+Multiphysics>. (Accessed:19.02.2020).
- [69] SIMSCALE. *What is CFD — Computational Fluid Dynamics?* URL: <https://www.simscale.com/docs/content/simwiki/cfd/whatis CFD.html>. (accessed: 15.04.2020).
- [70] Yunus A Çengel. “Fluid mechanics : fundamentals and applications”. eng. In: 3rd ed. in SI units. Boston: McGraw-Hill, 2014. Chap. 15 Introduction to computational fluid dynamics, pp. 879–893. ISBN: 9781259011221.
- [71] COMSOL Andrew Griesmer. *Meshing and Optimization in Engineering Magazines*. URL: <https://www.comsol.com/blogs/meshing-and-optimization-in-engineering-magazines/>. (accessed: 16.04.2020).

- [72] COMSOL. *Perform Mechanical Analyses with the Structural Mechanics Module*. URL: <https://www.comsol.com/structural-mechanics-module>. (Accessed:03.04.2020).
- [73] NTNU. *Matlab, software information*. URL: <https://innsida.ntnu.no/wiki/-/wiki/English/Matlab>. (Accessed:07.04.2020).
- [74] MatWeb. *316 Stainless Steel, annealed bar*. URL: <http://www.matweb.com/search/DataSheet.aspx?MatGUID=dfced4f11d63459e8ef8733d1c7c1ad2>. (accessed: 18.05.2020).
- [75] MatWeb. *Special Metals INCONEL Alloy 625*. URL: <http://www.matweb.com/search/DataSheet.aspx?MatGUID=4a194f59f35a427dbc5009f043349cb5>. (accessed: 18.05.2020).
- [76] The Engineering Toolbox. *Water - Dynamic and Kinematic Viscosity*. URL: https://www.engineeringtoolbox.com/water-dynamic-kinematic-viscosity-d_596.html. (Accessed:14.05.2020).
- [77] The Engineering Toolbox. *Water - Density, Specific Weight and Thermal Expansion Coefficient*. URL: https://www.engineeringtoolbox.com/water-density-specific-weight-d_595.html. (Accessed:12.05.2020).
- [78] Ya-jie GUO et al. "Density and viscosity of aqueous solution of K₂CrO₄/KOH mixed electrolytes". In: *Transactions of Nonferrous Metals Society of China* 20 (2010), s32–s36.

Appendix A

Design solid edge

A.1 End plate dimensions

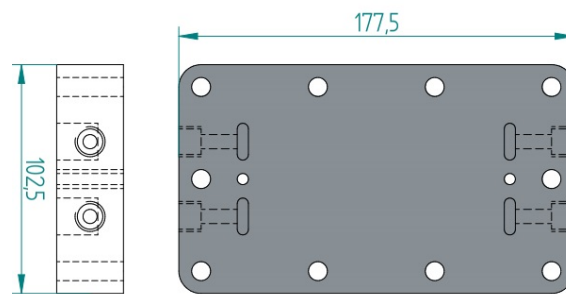


Figure A.1.1: Original end plate dimensions, before decreased length by centre hole

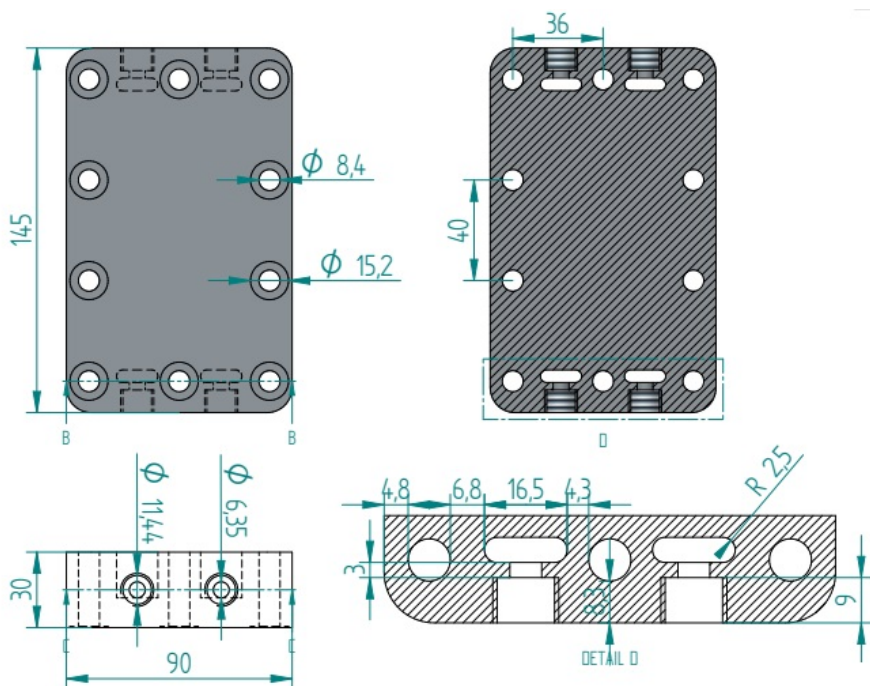


Figure A.1.2: Dimensions of the final end plate design. Top figures: Top and bottom surface, respectively. Bottom left figure: Short surface and Swagelok coupling, Bottom right figure: Dimensions between bolt-, inlet and coupling holes.

A.2 Bipolar plate dimensions

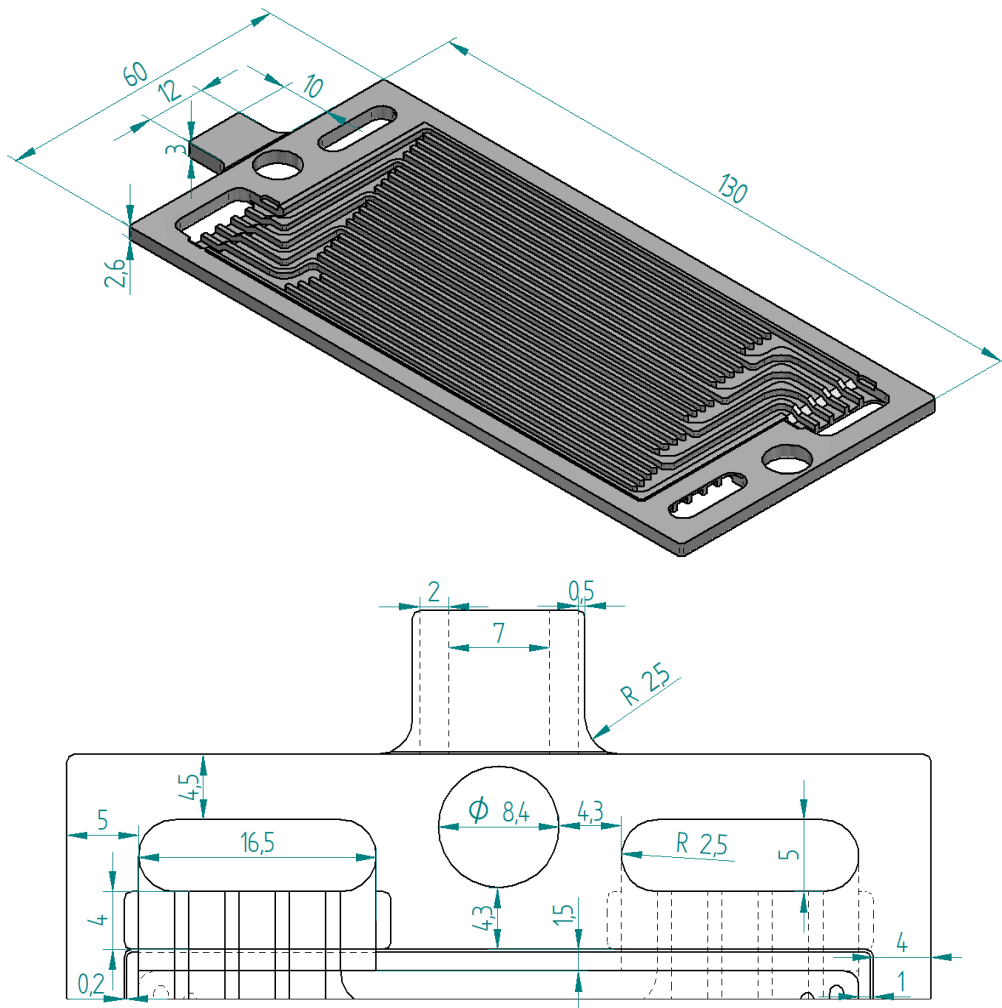


Figure A.2.1: Final dimensions of the bipolar plates.

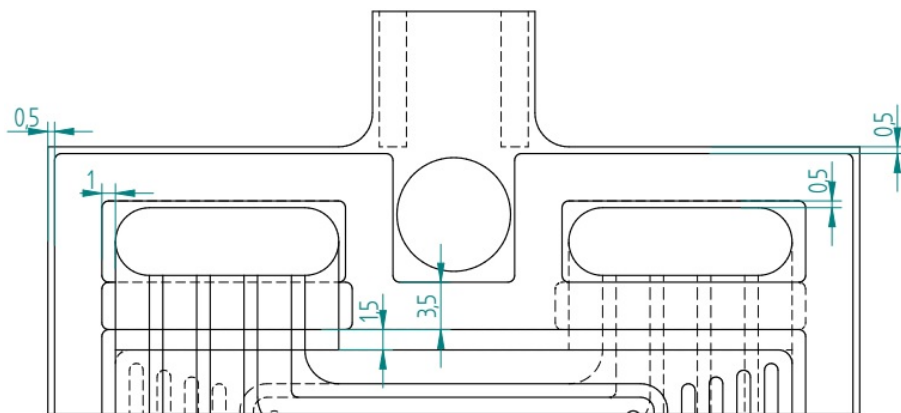


Figure A.2.2: Previous design of flow field plates, with gasket groove.

A.3 Unipolar plate dimensions

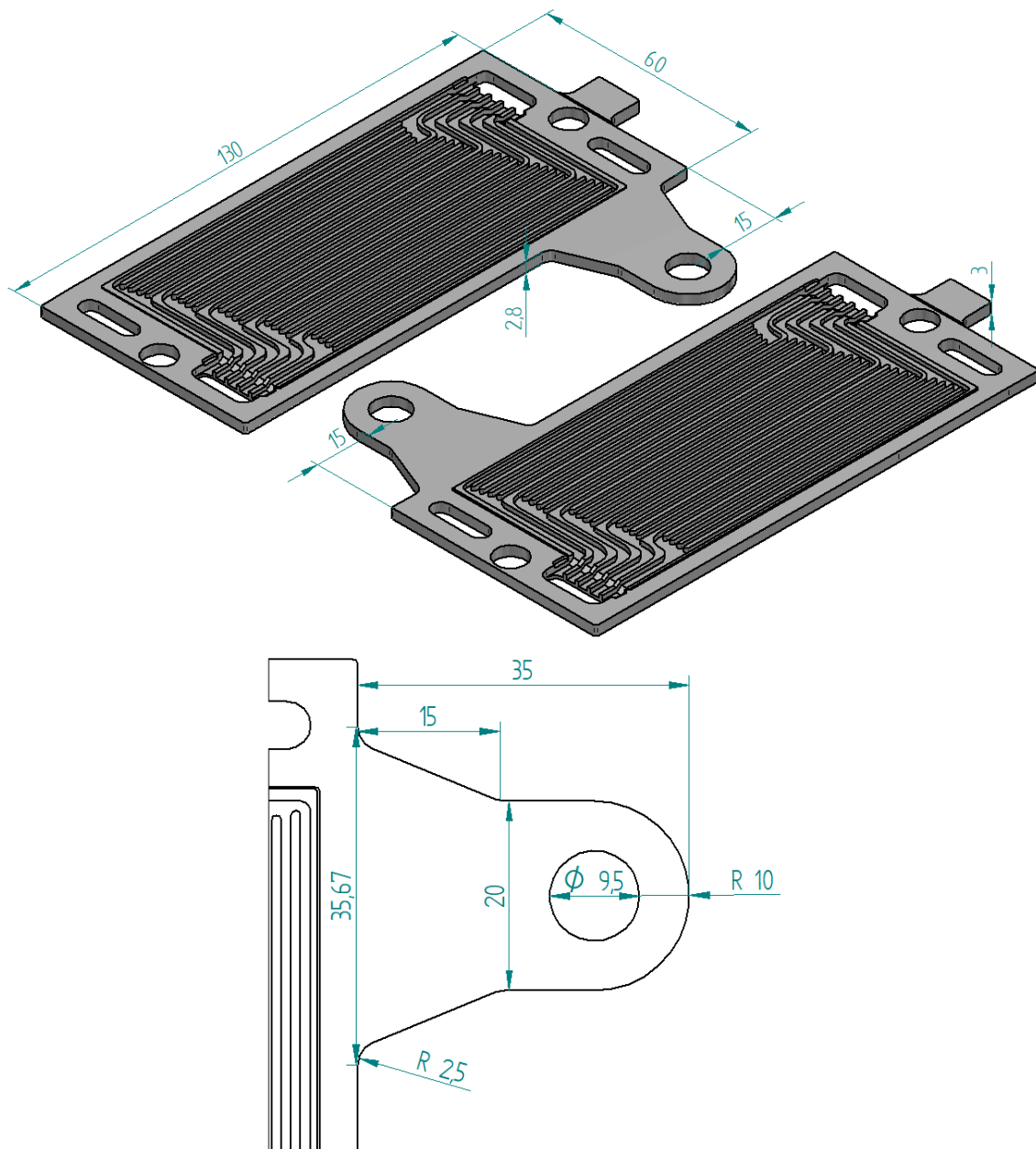


Figure A.3.1: Dimensions of the unipolar plates with terminal, the rest is similar to the bpp in figure A.2.1

A.4 Bridge dimensions

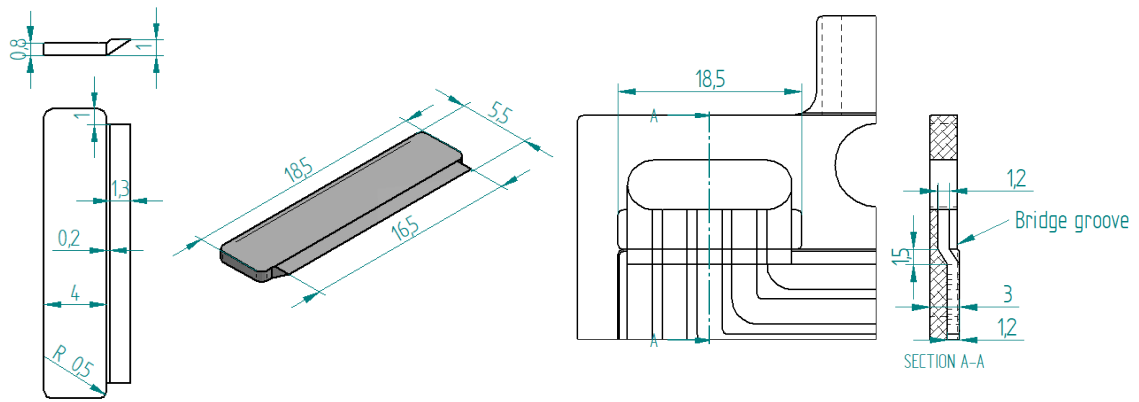


Figure A.4.1: Dimensions of the bridge and bridge groove.

A.5 Gasket dimensions

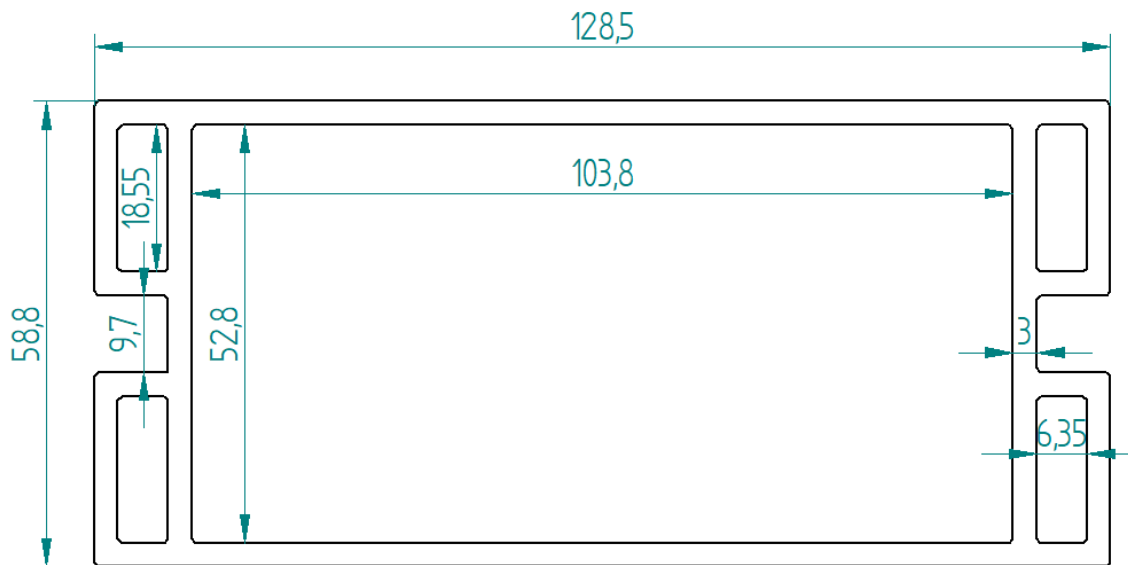


Figure A.5.1: Dimensions of the gasket, with either 1 or 1.5mm thickness.

A.6 Flow field dimensions

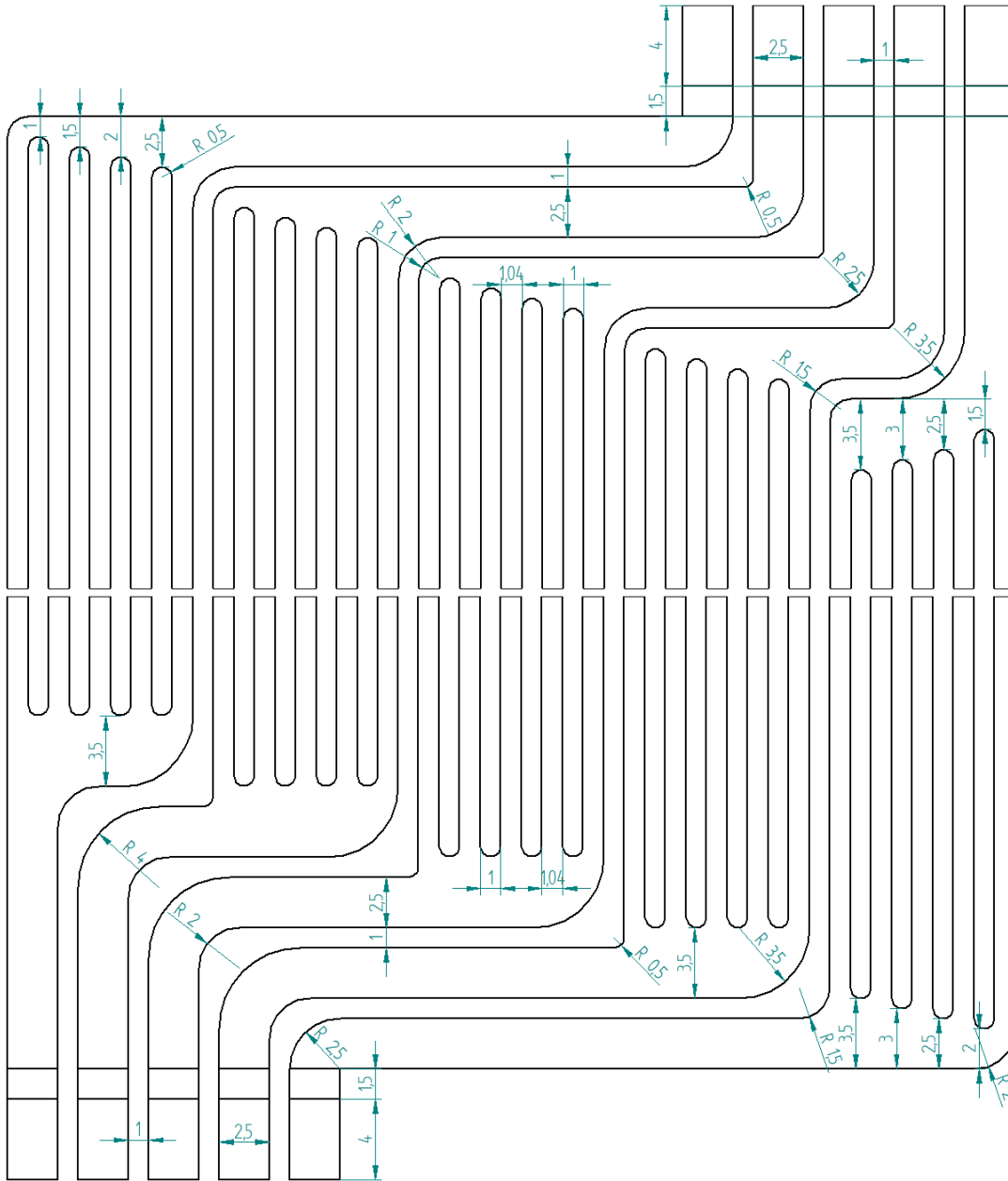


Figure A.6.1: Dimensions of the inlet(upper) and outlet(lower) side of the final flow field.

Appendix B

Components and materials

B.1 Stainless steel 316 Datasheet


316 Stainless Steel, annealed bar			
Physical Properties	Metric	English	Comments
Density	8.00 g/cc	0.289 lb/in ³	
Mechanical Properties	Metric	English	Comments
Hardness, Brinell	149	149	
Hardness, Knoop	169	169	Converted from Brinell
Hardness, Rockwell B	80	80	
Hardness, Vickers	155	155	Converted from Brinell
Tensile Strength, Ultimate	550 MPa	79800 psi	
Tensile Strength, Yield	240 MPa	34800 psi	
Elongation at Break	60 %	60 %	in 50 mm
Modulus of Elasticity	193 GPa	28000 ksi	
Izod Impact	129 J	95.1 ft-lb	
Charpy Impact	105 J	77.4 ft-lb	V-notch
Electrical Properties	Metric	English	Comments
Electrical Resistivity	0.0000740 ohm-cm	0.0000740 ohm-cm	at 20°C
Magnetic Permeability	1.008	1.008	at RT
Thermal Properties	Metric	English	Comments
CTE, linear 	16.0 µm/m-°C	8.89 µin/in-°F	
	@Temperature 0.000 - 100 °C	@Temperature 32.0 - 212 °F	
	16.2 µm/m-°C	9.00 µin/in-°F	
@Temperature 0.000 - 315 °C	@Temperature 32.0 - 599 °F		
	17.5 µm/m-°C	9.72 µin/in-°F	
@Temperature 0.000 - 540 °C	@Temperature 32.0 - 1000 °F		
Specific Heat Capacity	0.500 J/g-°C	0.120 BTU/lb-°F	
@Temperature 0.000 - 100 °C	@Temperature 32.0 - 212 °F		
Thermal Conductivity	16.3 W/m-K	113 BTU-in/hr-ft ² -°F	
@Temperature 100 °C	@Temperature 212 °F		
Melting Point	1370 - 1400 °C	2500 - 2550 °F	
Solidus	1370 °C	2500 °F	
Liquidus	1400 °C	2550 °F	
Maximum Service Temperature, Air	870 °C	1600 °F	Intermittent
	925 °C	1700 °F	Continuous Service
Component Elements Properties	Metric	English	Comments
Carbon, C	<= 0.080 %	<= 0.080 %	
Chromium, Cr	16 - 18 %	16 - 18 %	
Iron, Fe	61.8 - 72 %	61.8 - 72 %	As Remainder
Manganese, Mn	<= 2.0 %	<= 2.0 %	
Molybdenum, Mo	2.0 - 3.0 %	2.0 - 3.0 %	
Nickel, Ni	10 - 14 %	10 - 14 %	
Phosphorous, P	<= 0.045 %	<= 0.045 %	
Silicon, Si	<= 1.0 %	<= 1.0 %	
Sulfur, S	<= 0.030 %	<= 0.030 %	

Figure B.1.1: Stainless steel 316, end plate material, datasheet, edited from reference.[74]

B.2 Inconel 625 Alloy Datasheet






Special Metals INCONEL® Alloy 625			
Physical Properties	Metric	English	Comments
Density	8.44 g/cc	0.305 lb/in ³	
Mechanical Properties	Metric	English	Comments
Tensile Strength, Ultimate	880 MPa	128000 psi	Annealed
	760 MPa	110000 psi	Annealed prior to test
	@Temperature 650 °C	@Temperature 1200 °F	
Tensile Strength, Yield	460 MPa	66700 psi	Annealed
	290 MPa	42100 psi	Annealed prior to test
	@Temperature 650 °C	@Temperature 1200 °F	
Elongation at Break	50 %	50 %	Annealed prior to test.
	55 %	55 %	Annealed prior to test.
	@Temperature 650 °C	@Temperature 1200 °F	
Rupture Strength 	17.2 MPa	2500 psi	
	@Temperature 982 °C, Time 3.60e+6 sec	@Temperature 1800 °F, Time 1000 hour	
	31.0 MPa	4500 psi	
	@Temperature 982 °C, Time 360000 sec	@Temperature 1800 °F, Time 100 hour	
	89.6 MPa	13000 psi	
	@Temperature 816 °C, Time 3.60e+6 sec	@Temperature 1500 °F, Time 1000 hour	
	124 MPa	18000 psi	
	@Temperature 816 °C, Time 360000 sec	@Temperature 1500 °F, Time 100 hour	
	365 MPa	53000 psi	
	@Temperature 649 °C, Time 3.60e+6 sec	@Temperature 1200 °F, Time 1000 hour	
	441 MPa	64000 psi	
	@Temperature 649 °C, Time 360000 sec	@Temperature 1200 °F, Time 100 hour	
Electrical Properties	Metric	English	Comments
Electrical Resistivity	0.000129 ohm-cm	0.000129 ohm-cm	
Magnetic Permeability	1.0006	1.0006	at 200 Oersted (15.9 kA/m)
Curie Temperature	<= -196 °C	<= -321 °F	
Thermal Properties	Metric	English	Comments
CTE, linear	12.8 µm/m-°C	7.11 µin/in-°F	
	@Temperature 20.0 - 100 °C	@Temperature 68.0 - 212 °F	
Specific Heat Capacity	0.410 J/g-°C	0.0980 BTU/lb-°F	
Thermal Conductivity	9.80 W/m-K	68.0 BTU-in/hr-ft ² -°F	
Melting Point	1290 - 1350 °C	2350 - 2460 °F	
Solidus	1290 °C	2350 °F	
Liquidus	1350 °C	2460 °F	
Component Elements Properties	Metric	English	Comments
Aluminum, Al	<= 0.40 %	<= 0.40 %	
Carbon, C	<= 0.10 %	<= 0.10 %	
Chromium, Cr	20 - 23 %	20 - 23 %	
Cobalt, Co	<= 1.0 %	<= 1.0 %	
Iron, Fe	<= 5.0 %	<= 5.0 %	
Manganese, Mn	<= 0.50 %	<= 0.50 %	
Molybdenum, Mo	8.0 - 10 %	8.0 - 10 %	
Nickel, Ni	>= 58 %	>= 58 %	
Niobium, Nb (Columbium, Cb)	3.15 - 4.15 %	3.15 - 4.15 %	Includes Ta
Phosphorous, P	<= 0.015 %	<= 0.015 %	
Silicon, Si	<= 0.50 %	<= 0.50 %	
Sulfur, S	<= 0.015 %	<= 0.015 %	
Titanium, Ti	<= 0.40 %	<= 0.40 %	

Figure B.2.1: Inconel 625 Alloy, datasheet, edited from reference.[75]

B.3 EPDM 4000 HG-60 Datasheet

	RUBBER SHEETS		PHYSICAL PROPERTIES AND TECHNICAL INFORMATION	
	CODE	TRADE NAME		
	4000 60	Standard EPDM sheet 60 ShA		
POLYMER: EPDM	APPLICATION Ethylene-propylene			

CHARACTERISTICS	UNITS OF MEASURE	SPECIFICATIONS	VALUES	TOLERANCE
HARDNESS (H):	Sh.A3	ASTM D 2240	60	± 5
TENSILE STRENGTH (CR)	MPa	ASTM D 412C	7	min.
ELONGATION AT BREAK (AR)	%	ASTM D 412C	350	min.
TEAR STRENGTH	N/mm (.)	ASTM D 624B	20	min.
ABRASION RESISTANCE	mm ³	DIN 53516		
SPECIFIC GRAVITY	g/cm ³	DIN 53479	1,28	± 0,03

AGEING	Δ H	Sh.A3		8
In: Air	Δ CR	%	ASTM D 573	- 20
For: 72 h	Δ AR	%		- 40
At: 100 °C	Δ V	%		
AGEING	Δ H	Sh.A3		
In: Ozone	Δ CR	%	ASTM D 1149	OK
For: 70 h	Δ AR	%		
At: 30 °C -100 pphm- all. 50	Δ V	%		
AGEING	Δ H	Sh.A3		-5
In: Water	Δ CR	%	ASTM D 471	
For: 72 h	Δ AR	%		
At: 100 °C	Δ V	%		+ 5

WORKING TEMPERATURES					
In Air	°C	ASTM D 573	min:	- 30	max: + 100
In Oil	°C	ASTM D 471	min:		max:
In Water	°C	ASTM D 471	min:		max: +90

MAIN CHARACTERISTICS					
Elasticity	Compression	Abrasion	Flame	Fuels	Ozone
GOOD	GOOD/POOR	GOOD/POOR	POOR	UNSUITABLE	EXCELLENT

This data sheet has been issued with the greatest care and it is the result of several proofs made in our laboratory, according to specific norms. We don't ensure that the same tests carried out in other laboratories at the same conditions can give the same results.

B.4 Helical compression spring Datasheet



Gelb / Yellow
eXtra Large Force

Hülsen-Ø Ø guide sleeve	Dorn-Ø Ø guide pin	Länge Length	Bestell.-Nr. Order No	Federrate Spring rate
10	5	25	241.17.10.025	36,8
		32	241.17.10.032	27,9
		38	241.17.10.038	23,7
		44	241.17.10.044	19,2
		51	241.17.10.051	16,5
		64	241.17.10.064	13,2
		76	241.17.10.076	10,9
		305	241.17.10.305	2,6
12,5	6,3	25	241.17.13.025	58,5
		32	241.17.13.032	43,9
		38	241.17.13.038	36,0
		44	241.17.13.044	30,3
		51	241.17.13.051	26,2
		64	241.17.13.064	21,2
		76	241.17.13.076	17,1
		89	241.17.13.089	14,5
		305	241.17.13.305	4,3
16	8	25	241.17.16.025	118,0
		32	241.17.16.032	89,0
		38	241.17.16.038	72,1
		44	241.17.16.044	60,9
		51	241.17.16.051	52,3
		64	241.17.16.064	41,2
		76	241.17.16.076	34,1
		89	241.17.16.089	29,5
		102	241.17.16.102	25,6
		305	241.17.16.305	8,4

Figure B.4.1: Helical compression spring data sheet.

B.5 RENY bolt Datasheet



Properties of Plastic Screws

- The Abbreviations, Names, and Heat Resistance Temperature of Plastics

Abbreviation	Name	Heat Resistance Temperature
VESPEL*	SCP-5000	288°C
PEEK	Polyetheretherketone	350°C
PTFE	Tetrafluoroethylene	180°C
PPS	Polyphenylene Sulfide	260°C
HPVC	Hard Polyvinyl Chloride	200°C
RENY*	RENY	35°C
PC	Polycarbonate	105°C
PP	Polypropylene	115°C
PVDF	Polyvinylidene Fluoride	65°C

*The heat resistance temperatures in the chart are for the plastic material. The max. operating temperature of the product changes with performance conditions such as tightening torque.

*VESPEL is a registered trademark of DuPont.
*RENY is a registered trademark of Mitsubishi Engineering-Plastics Corporation.

- Selection Criteria for Plastic Screws

Strength RENY>PPS>VESPEL(SCP-5000)>PEEK>VESPEL(SP-1)>PC>PVDF>PP>HPVC>PTFE From tensile strength data
Heat Resistance VESPEL(SCP-5000)>VESPEL(SP-1)>PTFE>PPS>PEEK>PVDF>PC>RENY>PP>HPVC From heat resistance temperature
Chemical Resistance PTFE>PVDF>HPVC>PP>PEEK>PPS>PC>VESPEL(SCP-5000)>VESPEL(SP-1)>RENY From chemical resistance data

Precautions for Plastic Screws

- While these plastics screws comply with JIS and ISO standards, there are some areas irrelevant to these screws as their manufacturing methods differ from that of metal screws.
- The values in the mechanical properties chart are reference values.
- Use a torque driver or torque wrench when tightening.
- Always carry out tests under performance conditions similar to actual conditions in advance.
- The color of machine screws, bolts, nuts, and washers may differ by lot.

Physical Properties

Properties	Test Method	Unit	VESPEL SP-1	VESPEL SCP-5000	PEEK	PTFE	PPS	RENY	PC	PP	PVDF
Tensile Strength	D638	N/mm ²	86	160	97	24	185	285	62	36	57
Tensile Elongation	D638	%	7.5	200-400	1.9	2.1	110	500	70-80	—	—
Flexural Strength	D790	N/mm ²	110	247	156	—	255	360	86.2	—	75
Flexural Modulus	D790	GPa	3.1	5.7	4.1	0.56	13.2	17.4	2.3	1.5	1.99
Izot Impact (with Notch)	D256	J/m	42.7	—	94	160	100	110	880	30	160-375
Rockwell Hardness	D785	R and M Scales	M90	M100	M99	—	M100	M111	R120	R100	R93-116
Deflection Temp. under Load (1.82 MPa)	D648	°C	360	350	152	—	260	234	135	120	80
Flame Class	UL94	—	V-0	V-0	V-0	V-0	V-0	HB	V-2	HB	V-0
Dielectric Constant (10 ⁴ Hz)	D150	—	3.6	3.3	3.3	<2.1	4.6	4.0	2.9	—	10
Dielectric Loss Tangent (10 ⁴ Hz)	D150	—	0.0034	0.001	0.003	<0.0002	0.002	0.009	0.009	—	0.015
Volume Resistivity (X10 ¹⁴)	D257	Ω·m	1-10	1	4.9	>100	1.0	1.3	4.0	1.0	0.1-1
Dielectric Breakdown Strength	D149	MV/m	22	—	17	19	12	32	16	31	300
Arc Resistance	D495	sec	—	23	>300	120	129	120	—	—	—
Specific Gravity	D792	—	1.43	1.30	2.14-2.2	1.66	1.65	1.20	0.91	1.79	—
Water Absorption (in 23 °C Water for 24 h)	D570	%	0.240	0.080	0.500	0.010	0.015	0.140	0.150	0.010	0.030
Glass Fiber Content	—	%	—	—	—	—	40	50	—	—	—

*Values in chart are for reference only. They are not guaranteed values.

Physical Properties (HPVC)

Properties	Test Method (JIS)	Unit	HPVC
Tensile Strength	JISK7162	Test Speed : 10mm/min	38.8
Tensile Elongation	JISK7162	Test Speed : 10mm/min	%
Hardness	JISK7215	10 seconds later (2 mm thickness 3 sheets overlaid)	188
Specific Gravity	JISK7112 : Method A	—	97

*Values in chart are for reference only. They are not guaranteed values.

Chemical Resistance

Chemical Name	VESPEL SP-1	VESPEL SCP-5000	PEEK	PTFE	PPS	HPVC	RENY	PC	PP	PVDF
10% Hydrochloric Acid	○	○	○	○	○	○	○	○	○	○
10% Sulfuric Acid	○	○	○	○	○	○	○	○	○	○
50% Sulfuric Acid	×	×	×	×	×	×	×	×	×	×
10% Nitric Acid	△	△	△	△	△	△	△	△	△	△
50% Nitric Acid	×	×	×	×	×	×	×	×	×	×
10% Hydrofluoric Acid	△	△	△	△	△	△	△	△	△	△
50% Hydrofluoric Acid	×	×	×	×	×	×	×	×	×	×
Phosphoric Acid	△	△	△	△	△	△	△	△	△	△
Formic Acid	△	△	△	△	△	△	△	△	△	△
Phosphoric Acid	○	○	○	○	○	○	○	○	○	○
Citric Acid	○	○	○	○	○	○	○	○	○	○
Chromic Acid	○	○	○	○	○	○	○	○	○	○
Boric Acid	○	○	○	○	○	○	○	○	○	○
Methyl Alcohol	△	△	△	△	△	△	△	△	△	△
Glycol	○	○	○	○	○	○	○	○	○	○
Ammonia	×	×	×	×	×	×	×	×	×	×
10% Sodium Hydroxide	×	×	×	×	×	×	×	×	×	×
10% Potassium Hydroxide	×	×	×	×	×	×	×	×	×	×
Calcium Hydroxide	—	—	—	—	—	—	—	—	—	—
Water	○	○	○	○	○	○	○	○	○	○
Hydrogen Sulfide (Gas)	○	○	○	○	○	○	○	○	○	○
Sulfur Dioxide	—	—	—	—	—	—	—	—	—	—
Ammonium Nitrate	—	—	—	—	—	—	—	—	—	—
Sodium Nitrate	—	—	—	—	—	—	—	—	—	—
Calcium Carbonate	—	—	—	—	—	—	—	—	—	—
Calcium Chloride	—	—	—	—	—	—	—	—	—	—
Magnesium Chloride	—	—	—	—	—	—	—	—	—	—
Magnesium Sulfate	—	—	—	—	—	—	—	—	—	—
Zinc Sulfate	—	—	—	—	—	—	—	—	—	—
Hydrogen peroxide	△	△	△	△	△	△	△	△	△	△

○ Usable
△ Usable under certain conditions
× Non-usable
— A test piece was used to acquire the test data at room temperature (23°C). Chemical resistance changes with performance conditions. Always carry out tests under performance conditions similar to actual conditions in advance.

Torsional Torque of Plastic Screws (N·m)

Material	VESPEL SP-1	VESPEL SCP-5000	PEEK	PTFE	PPS	HPVC	RENY	PC	PP	PVDF
M1.7	—	—	0.02	—	—	—	0.03	0.02	—	—
M2	—	—	0.06	—	0.08	—	0.1	0.05	—	—
M2.6	—	—	0.16	—	—	—	0.24	—	—	—
M3	0.12	0.21	0.3	0.02	0.36	—	0.39	0.22	—	—
M4	0.27	0.47	0.64	0.03	0.71	0.18	0.79	0.54	0.23	—
M5	0.54	0.98	1.28	0.08	1.42	0.41	1.77	1.03	0.51	0.64
M6	0.95	1.65	2.26	0.14	2.11	0.65	2.94	1.37	0.8	0.88
M8	2.26	4.04	5.98	0.24	5.29	—	7.85	—	2.2	2.65
M10	—	—	—	—	11.8	—	—	—	—	—
M12	—	—	—	—	20.6	—	—	—	—	—

*Values in chart are for reference only. They are not guaranteed values. The recommended torque is 50% of the value in the chart. The value differs depending on the head shape of the screw. See the product page for details.

NBK <https://www.nbk1560.com>

Appendix C

Fluid flow simulations from COMSOL

Unless other information are given, simulations was performed with water at 20°C. The average velocity results was converted to flow rate with equation C.0.1.

$$\text{Flow rate [g/min]} = V_{avg}[\text{m/s}] \cdot A_c[\text{m}^2] \cdot \rho[\text{kg/m}^3] \cdot 1000[\text{g/kg}] \cdot 60[\text{s/min}] \quad (\text{C.0.1})$$

C.1 Different flow field patterns

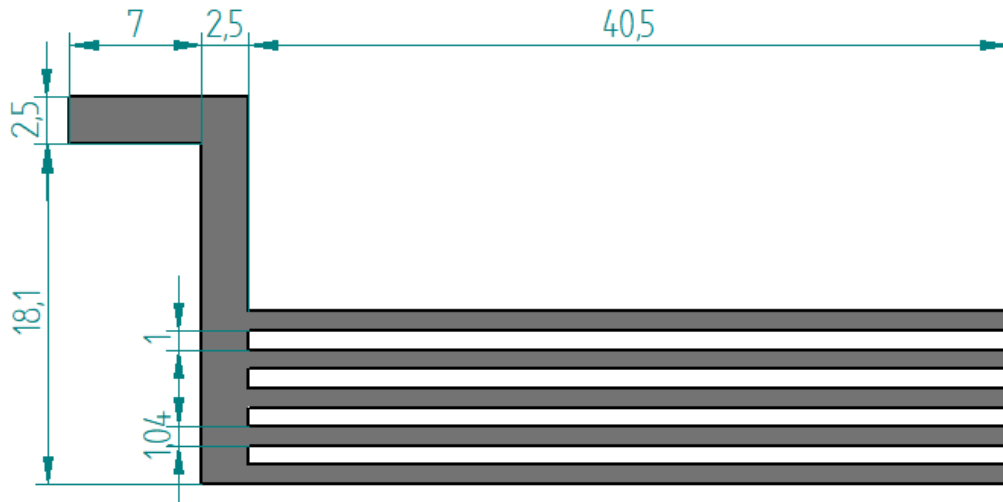
Table C.1.1: Results from simulations on the flow fields in figure 3.1.1 at 50g/min. Displaying the pressure [Pa] over the flow fields.

Flow field	Max	Min
Straight	341	-2
Straight V-neck	210	-2
5ch horizontal	180	-1
5ch vertical	189	-1

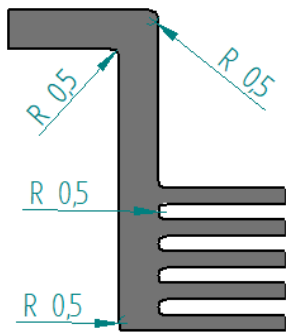
C.2 Centre channels

Table C.2.1: Results from simulations on different centre channels (figure C.2.1) with a flow rate of 50g/min. Displaying the average velocity in the sub channels (cross section: 1.04x1mm) and pressure over the channels.

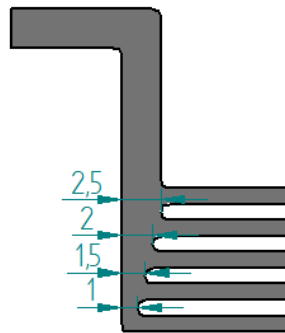
Channel	Average velocity [m/s]					Pressure [Pa]	
	Sub 1	Sub 2	Sub 3	Sub 4	Sub 5	Max	Min
C1	0.1368	0.1452	0.1547	0.1661	0.1843	1002	-34
C2	0.1417	0.1483	0.1540	0.1632	0.1800	892	-54
C3	0.1334	0.1540	0.1562	0.1668	0.1773	908	-57
C4	0.1288	0.1623	0.1687	0.1628	0.1648	862	-53
C5	0.1314	0.1643	0.1600	0.1627	0.1691	870	-56
C6	0.1495	0.1540	0.1553	0.1600	0.1687	837	-59
C7	0.1494	0.1550	0.1551	0.1599	0.1682	833	-54
C8	0.1504	0.1546	0.1543	0.1594	0.1684	829	-53
C9	0.1503	0.1540	0.1536	0.1587	0.1711	831	-52
C10	0.1501	0.1538	0.1541	0.1600	0.1691	778	-2



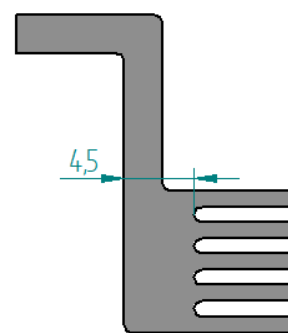
(a) C1



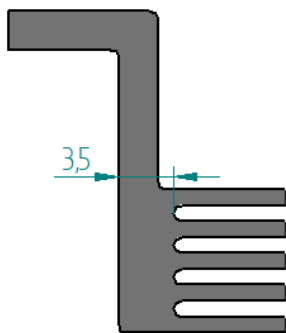
(b) C2



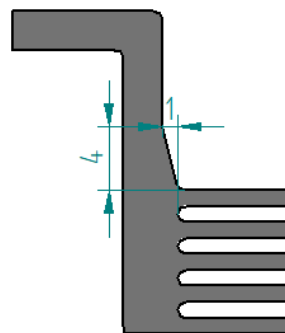
(c) C3



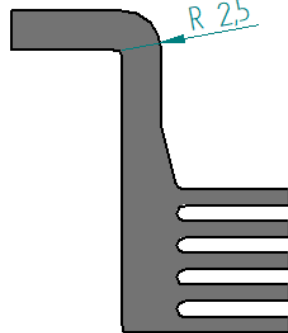
(d) C4



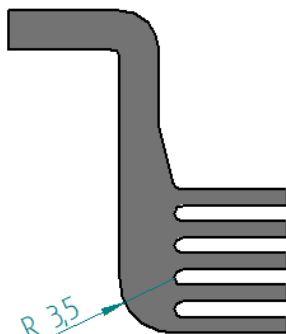
(e) C5



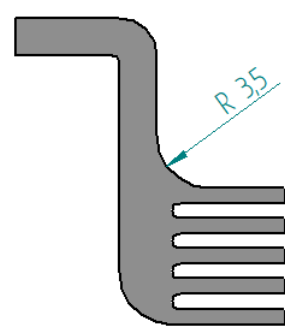
(f) C6



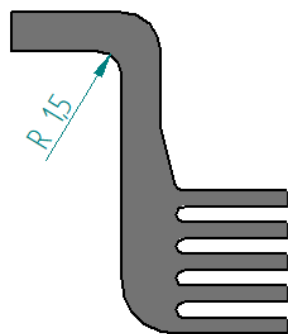
(g) C7



(h) C8



(i) C9



(j) C10

Figure C.2.1: Centre models used to simulate pressure drop and the fluid distribution in the sub channels. The dimensions are in [mm], and the depth is 1mm.

C.3 Different channel depths

Table C.3.1: Results from the simulations on the centre channel in figure C.2.1b with different depths, ranging from 0.5-1.3mm. Displaying the pressure [Pa] with a flow rate of up to 50g/min (at 1.0).

—	0.5 mm		0.6 mm		0.7 mm		0.8 mm		0.9 mm	
Factor	Max	Min	Max	Min	Max	Min	Max	Min	Max	Min
0.1	332	0	205	0	139	0	101	0	76	0
0.2	681	0	423	0	289	0	211	0	159	0
0.3	1050	1	655	0	450	0	330	0	249	0
0.4	1442	1	902	0	623	0	458	-1	347	-1
0.5	1862	1	1167	1	809	-1	594	-9	451	-7
0.6	2310	1	1451	-12	1009	-11	740	-20	562	-16
0.7	2789	1	1756	-28	1224	-22	896	-33	681	-26
0.8	3300	-3	2082	-48	1456	-36	1062	-49	808	-38
0.9	3844	-21	2429	-71	1703	-52	1239	-66	944	-51
1.0	4422	-42	2804	-98	1969	-70	1428	-86	1093	-66
—	1.0 mm		1.1 mm		1.2 mm		1.3 mm			
Factor	Max	Min	Max	Min	Max	Min	Max	Min		
0.1	59	0	48	0	40	0	34	0		
0.2	125	0	101	0	84	-0	71	0		
0.3	197	0	159	0	132	-0	112	0		
0.4	275	-2	223	-2	185	-2	157	-2		
0.5	359	-8	291	-7	242	-6	206	-6		
0.6	450	-15	365	-13	304	-12	260	-11		
0.7	548	-24	444	-21	373	-18	318	-18		
0.8	653	-35	532	-30	446	-26	381	-25		
0.9	768	-47	625	-41	525	-35	448	-33		
1.0	892	-60	724	-52	608	-46	519	-43		

Table C.3.2: Results from the simulations on the centre channel in figure C.2.1b with different depths, ranging from 0.5-1.3mm. Displaying average velocity [m/s] in the sub channels (cross section: Depthx1.04mm) at a flow rate of 50g/min.

Depth	Sub 1	Sub 2	Sub 3	Sub 4	Sub 5
0.5 mm	0.2834	0.2963	0.3076	0.3272	0.3558
0.6 mm	0.2394	0.2457	0.2560	0.2736	0.2975
0.7 mm	0.2034	0.2111	0.2195	0.2340	0.2542
0.8 mm	0.1769	0.1844	0.1921	0.2049	0.2234
0.9 mm	0.1568	0.1650	0.1716	0.1819	0.2005
1.0 mm	0.1421	0.1485	0.1538	0.1640	0.1789
1.1 mm	0.1278	0.1346	0.1413	0.1499	0.1622
1.2 mm	0.1160	0.1245	0.1296	0.1384	0.1470
1.3 mm	0.1084	0.1140	0.1191	0.1258	0.1364

C.4 Inlet geometries

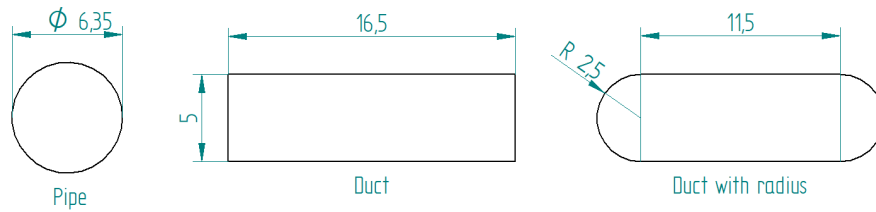


Figure C.4.1: Models used to simulate pressure drop in the inlet geometries, values in [mm]. Pipe is the inlet from the connection to the stack and duct is the channel from the pipe to the sub channels, with and without radius.

Table C.4.1: Results from the simulation on different geometries in figure C.4.1 with a length of 1000mm and a flow rate of up to 250g/min (factor=1.0). Displaying the pressure drop [Pa] over the different models.

Factor	Pipe	Duct	Duct with radius
0.1	12	3	3
0.2	26	6	7
0.3	42	10	11
0.4	59	14	15
0.5	76	18	20
0.6	94	21	24
0.7	112	25	29
0.8	130	29	34
0.9	148	33	38
1.0	166	37	43

C.5 Immersion channels

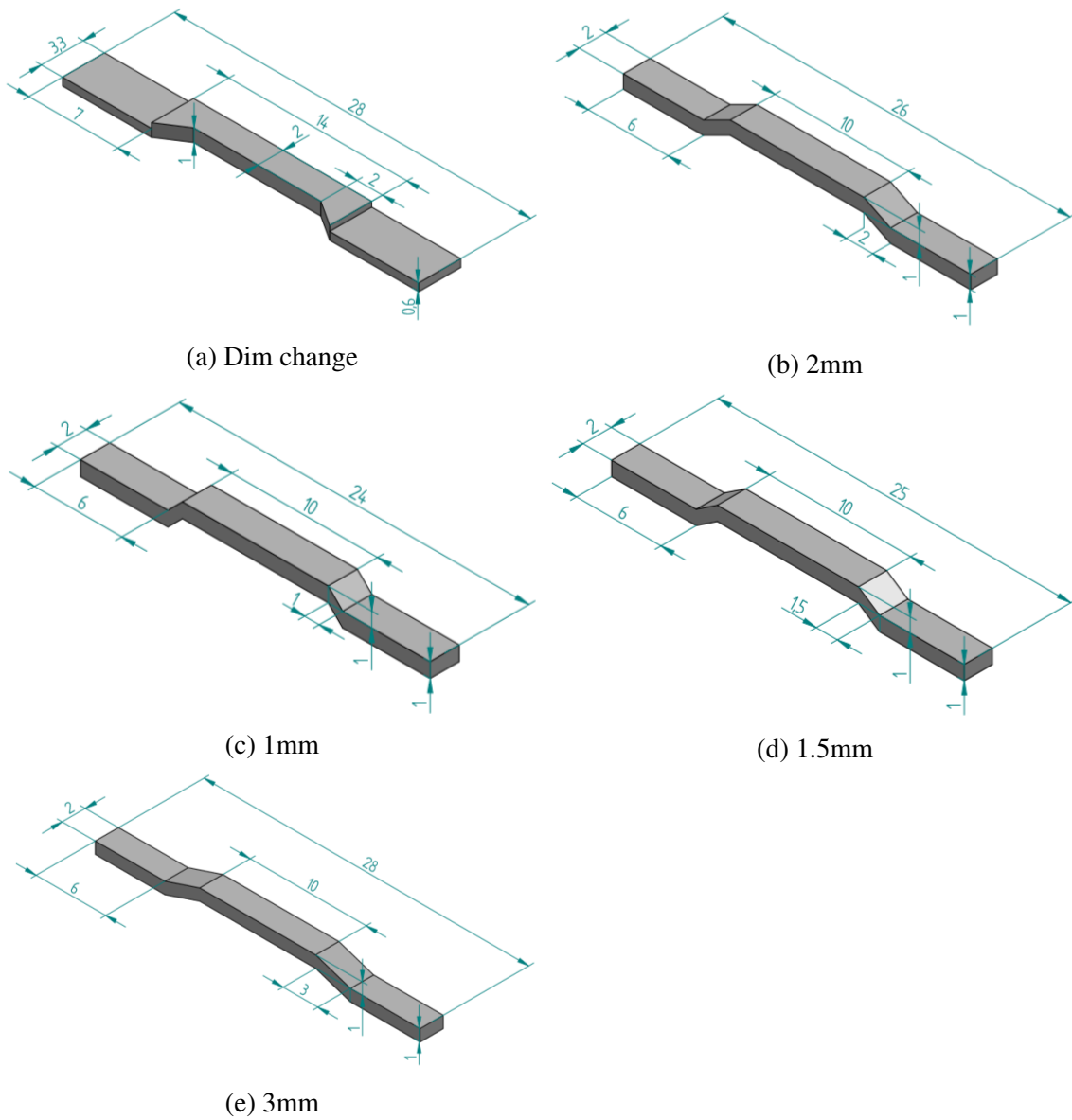


Figure C.5.1: Models for simulating from inlet to channels under the bridge. Figure (a) has a dimension change and (b-e) have a ramp that is moving the channel up 1mm in different lengths.

C.6 Width of channels and inlet

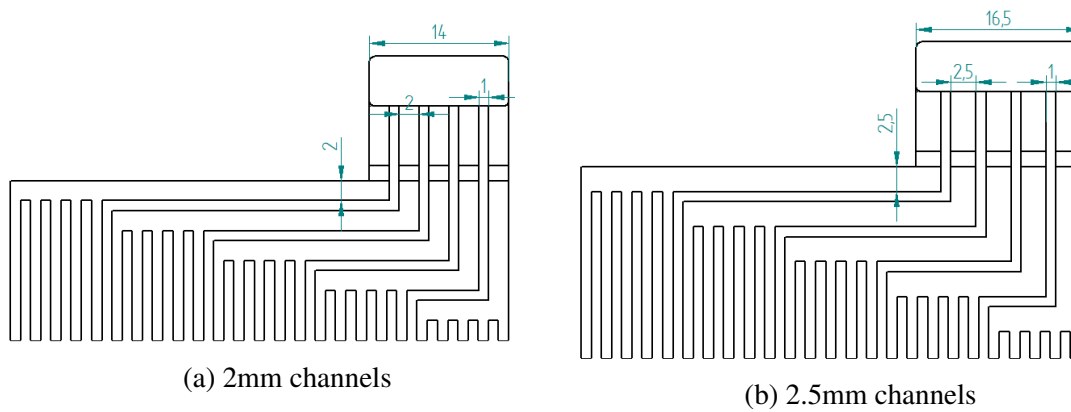


Figure C.6.1: Models used to simulate the different channel widths in figure 3.1.9, where (a) has 2mm channels and (b) has 2.5mm channels.

Table C.6.1: Pressure results from simulations of the models in C.6.1 at 50g/min.

Channel width [mm]	Max [Pa]	Min [Pa]
2	214	-1
2.5	170	-1

C.7 Flow field with identical inlet/outlet

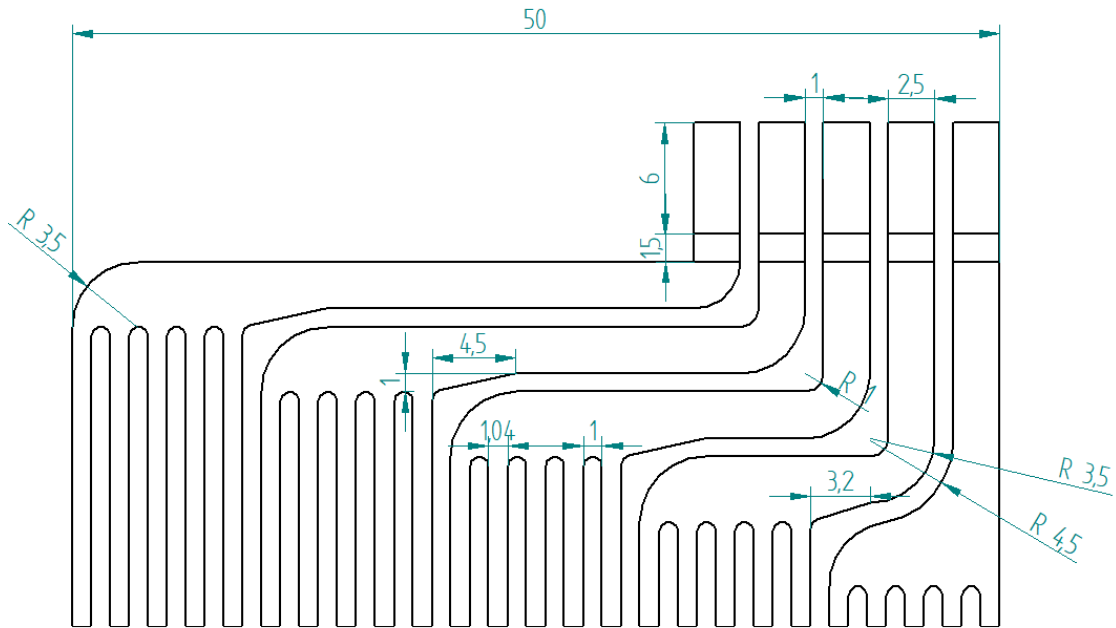


Figure C.7.1: Model used for simulating the different channels with identical half sides, where the values are in [mm] and the depth of the channels is 1mm. Channel 1 is on the right side and the same goes for sub channel 1.

Table C.7.1: Results from the simulation on the flow field in figure C.7.1, with a flow rate of 50g/min per channel. Displaying average velocity in sub channels (cross section: 1.04x1mm) and pressure over the channels.

Channel	Average velocity [m/s]					Pressure [Pa]	
	sub 1	sub 2	sub 3	sub 4	sub 5	max	min
1	0.1532	0.1667	0.1565	0.1509	0.1562	1002	-27
2	0.1579	0.1519	0.1522	0.1575	0.1649	1054	-14
3	0.1465	0.1532	0.1554	0.1609	0.1680	1051	-13
4	0.1447	0.1529	0.1554	0.1611	0.1687	1036	-13
5	0.1471	0.1572	0.1589	0.1606	0.1599	987	-13

C.8 Final flow field

C.8.1 Five channels

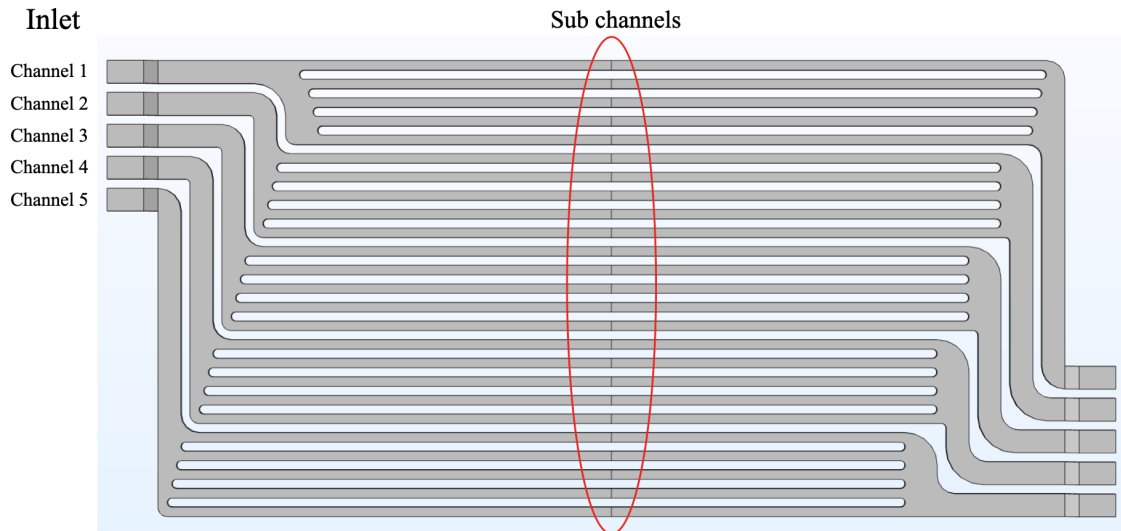


Figure C.8.1: Model in COMSOL of the final flow field divided into five separate channels. Each sub channel is referred to as Sub x.x (Sub "channel number" "1-5, starting at the top") and the dimensions is specified in appendix A.6.

Table C.8.1: Results from the simulation on the final design of the channels in figure C.8.1. Displaying the average velocity in the sub channels and pressure [Pa] over the channels with a flow rate of up to 50 g/min(Factor=1.0).

Average velocity [m/s]						Pressure drop [Pa]		
Ch 1	Sub 1.1	Sub 1.2	Sub 1.3	Sub 1.4	Sub 1.5	Ch 1	Max	Min
0.1	0.0122	0.0124	0.0126	0.0129	0.0130	0.1	45	0
0.2	0.0246	0.0251	0.0254	0.0259	0.0263	0.2	95	0
0.3	0.0370	0.0381	0.0382	0.0391	0.0398	0.3	150	-1
0.4	0.0495	0.0512	0.0511	0.0522	0.0533	0.4	210	-4
0.5	0.0620	0.0644	0.0639	0.0654	0.0669	0.5	275	-7
0.6	0.0745	0.0777	0.0768	0.0785	0.0805	0.6	345	-11
0.7	0.0872	0.0910	0.0897	0.0916	0.0941	0.7	420	-15
0.8	0.1000	0.1045	0.1025	0.1047	0.1078	0.8	500	-20
0.9	0.1129	0.1180	0.1153	0.1177	0.1214	0.9	586	-26
1.0	0.1260	0.1317	0.1280	0.1306	0.1350	1.0	676	-33
Ch 2	Sub 2.1	Sub 2.2	Sub 2.3	Sub 2.4	Sub 2.5	Ch 2	Max	Min
0.1	0.0130	0.0128	0.0126	0.0125	0.0123	0.1	46	0
0.2	0.0260	0.0258	0.0253	0.0252	0.0251	0.2	97	0
0.3	0.0391	0.0388	0.0380	0.0380	0.0380	0.3	153	-0
0.4	0.0524	0.0520	0.0508	0.0510	0.0511	0.4	215	-2
0.5	0.0657	0.0651	0.0635	0.0639	0.0643	0.5	282	-4
0.6	0.0790	0.0783	0.0762	0.0769	0.0776	0.6	354	-7
0.7	0.0924	0.0916	0.0889	0.0899	0.0909	0.7	433	-11
0.8	0.1058	0.1049	0.1015	0.1030	0.1042	0.8	517	-15
0.9	0.1194	0.1182	0.1141	0.1161	0.1176	0.9	606	-19
1.0	0.1329	0.1316	0.1266	0.1292	0.1311	1.0	701	-24
Ch 3	Sub 3.1	Sub 3.2	Sub 3.3	Sub 3.4	Sub 3.5	Ch 3	Max	Min
0.1	0.0130	0.0128	0.0126	0.0125	0.0124	0.1	46	0
0.2	0.0260	0.0257	0.0253	0.0252	0.0251	0.2	97	0
0.3	0.0388	0.0387	0.0382	0.0381	0.0382	0.3	153	-0
0.4	0.0517	0.0518	0.0510	0.0512	0.0515	0.4	214	-2
0.5	0.0645	0.0648	0.0639	0.0643	0.0649	0.5	280	-4
0.6	0.0774	0.0779	0.0768	0.0774	0.0785	0.6	351	-7
0.7	0.0903	0.0910	0.0897	0.0906	0.0921	0.7	428	-10
0.8	0.1031	0.1041	0.1025	0.1039	0.1058	0.8	511	-14
0.9	0.1160	0.1173	0.1154	0.1172	0.1195	0.9	599	-19
1.0	0.1288	0.1306	0.1282	0.1305	0.1334	1.0	693	-24
Ch 4	Sub 4.1	Sub 4.2	Sub 4.3	Sub 4.4	Sub 4.5	Ch 4	Max	Min
0.1	0.0130	0.0128	0.0126	0.0125	0.0123	0.1	46	0
0.2	0.0259	0.0257	0.0253	0.0252	0.0252	0.2	96	0
0.3	0.0387	0.0388	0.0382	0.0381	0.0383	0.3	152	-1
0.4	0.0513	0.0519	0.0512	0.0512	0.0516	0.4	212	-2
0.5	0.0637	0.0651	0.0642	0.0643	0.0652	0.5	277	-4
0.6	0.0762	0.0783	0.0773	0.0775	0.0788	0.6	348	-7
0.7	0.0885	0.0915	0.0903	0.0908	0.0926	0.7	424	-11
0.8	0.1008	0.1047	0.1034	0.1041	0.1065	0.8	506	-15
0.9	0.1130	0.1180	0.1165	0.1175	0.1205	0.9	593	-19
1.0	0.1252	0.1313	0.1296	0.1308	0.1346	1.0	685	-24
Ch 5	Sub 5.1	Sub 5.2	Sub 5.3	Sub 5.4	Sub 5.5	Ch 5	Max	Min
0.1	0.0131	0.0128	0.0126	0.0125	0.0122	0.1	46	0
0.2	0.0260	0.0258	0.0255	0.0252	0.0247	0.2	97	0
0.3	0.0389	0.0389	0.0385	0.0382	0.0376	0.3	153	-1
0.4	0.0515	0.0521	0.0517	0.0513	0.0506	0.4	213	-2
0.5	0.0641	0.0652	0.0649	0.0645	0.0637	0.5	277	-5
0.6	0.0765	0.0784	0.0782	0.0779	0.0770	0.6	348	-8
0.7	0.0889	0.0916	0.0916	0.0913	0.0903	0.7	423	-11
0.8	0.1012	0.1047	0.1050	0.1048	0.1037	0.8	503	-15
0.9	0.1136	0.1179	0.1184	0.1184	0.1172	0.9	588	-20
1.0	0.1258	0.1311	0.1318	0.1320	0.1307	1.0	678	-25

C.8.2 Stack with one flow field

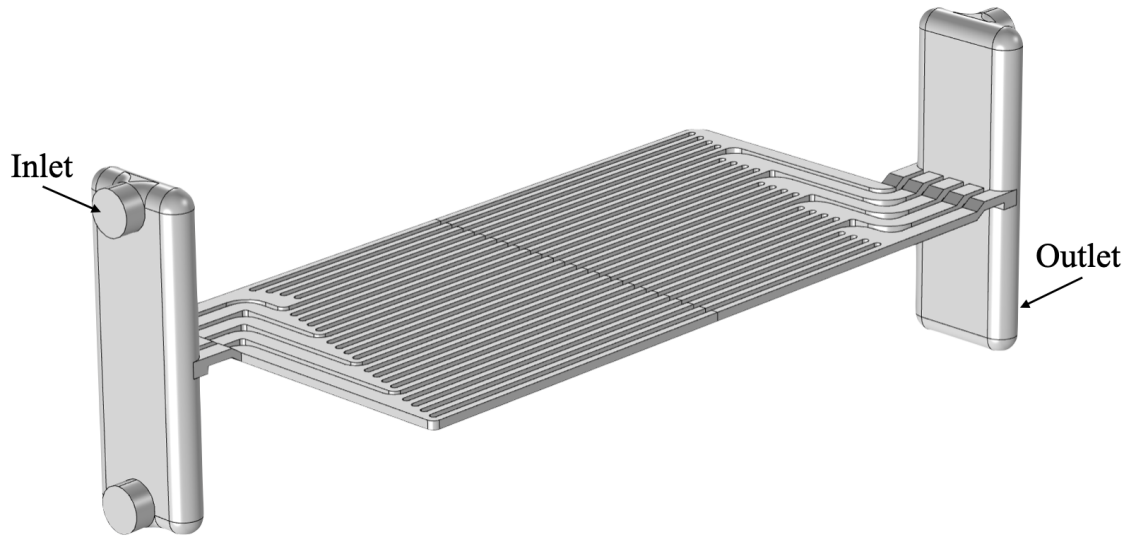


Figure C.8.2: Model used to simulate the fluid flow of the flow field with one inlet.

Table C.8.2: Results from simulations of the model in figure C.8.2 at 250g/min, displaying the average velocity [m/s] in the sub channels (cross section:1.04x1.2mm) for different solutions.

Channel	Average velocity					Pmax	Pmin
Water 60°C	Sub 1	Sub 2	Sub 3	Sub 4	Sub 5	928	-4
1	0.1267	0.1322	0.1262	0.1270	0.1334	-	-
2	0.1295	0.1241	0.1206	0.1226	0.1285	-	-
3	0.1232	0.1252	0.1231	0.1257	0.1291	-	-
4	0.1228	0.1267	0.1258	0.1277	0.1314	-	-
5	0.1253	0.1298	0.1289	0.1299	0.1300	-	-
1M KOH 60°C	Sub 1	Sub 2	Sub 3	Sub 4	Sub 5	692	-3
1	0.1252	0.1323	0.1194	0.1195	0.1284	-	-
2	0.1262	0.1183	0.1133	0.1177	0.1266	-	-
3	0.1178	0.1183	0.1153	0.1200	0.1265	-	-
4	0.1154	0.1206	0.1195	0.1240	0.1315	-	-
5	0.1161	0.1248	0.1250	0.1283	0.1300	-	-

Table C.8.3: Pressure readings related to table C.8.4, which display the pressures over the model in figure C.8.2 with a factor of 250g/min.

Factor	Pressure [Pa]	
	Max	Min
0.1	50	0
0.2	108	0
0.3	176	-1
0.4	253	-1
0.5	340	-1
0.6	436	-2
0.7	541	-2
0.8	657	-3
0.9	781	-3
1.0	916	-4

Table C.8.4: Results from the simulation on the model in figure C.8.2 with a flow rate of up to 250g/min (Factor=1.0). Displaying the Average velocity in the sub channels (cross section: 1.04x1.2mm) of model C.8.2.

Average velocity [m/s]					
Factor	Sub 1.1	Sub 1.2	Sub 1.3	Sub 1.4	Sub 1.5
0.1	0.0118	0.0121	0.0121	0.0122	0.0124
0.2	0.0237	0.0245	0.0244	0.0247	0.0252
0.3	0.0357	0.0370	0.0368	0.0373	0.0383
0.4	0.0479	0.0496	0.0493	0.0499	0.0515
0.5	0.0603	0.0625	0.0618	0.0625	0.0647
0.6	0.0729	0.0756	0.0743	0.0750	0.0780
0.7	0.0857	0.0888	0.0868	0.0875	0.0913
0.8	0.0986	0.1023	0.0993	0.1000	0.1046
0.9	0.1116	0.1160	0.1117	0.1124	0.1180
1.0	0.1247	0.1298	0.1242	0.1248	0.1313
—	Sub 2.1	Sub 2.2	Sub 2.3	Sub 2.4	Sub 2.5
0.1	0.0124	0.0124	0.0122	0.0119	0.0119
0.2	0.0247	0.0247	0.0244	0.0239	0.0242
0.3	0.0372	0.0370	0.0364	0.0359	0.0366
0.4	0.0497	0.0492	0.0484	0.0479	0.0492
0.5	0.0623	0.0615	0.0603	0.0599	0.0618
0.6	0.0750	0.0738	0.0721	0.0720	0.0746
0.7	0.0880	0.0860	0.0839	0.0840	0.0874
0.8	0.1011	0.0983	0.0956	0.0961	0.1004
0.9	0.1144	0.1106	0.1073	0.1082	0.1134
1.0	0.1277	0.1229	0.1190	0.1203	0.1265
—	Sub 3.1	Sub 3.2	Sub 3.3	Sub 3.4	Sub 3.5
0.1	0.0125	0.0123	0.0122	0.0121	0.0120
0.2	0.0250	0.0246	0.0246	0.0244	0.0244
0.3	0.0373	0.0370	0.0369	0.0367	0.0369
0.4	0.0496	0.0493	0.0491	0.0491	0.0496
0.5	0.0618	0.0616	0.0613	0.0616	0.0624
0.6	0.0739	0.0740	0.0734	0.0740	0.0753
0.7	0.0860	0.0863	0.0854	0.0864	0.0882
0.8	0.0980	0.0986	0.0973	0.0989	0.1012
0.9	0.1101	0.1109	0.1092	0.1113	0.1143
1.0	0.1221	0.1232	0.1211	0.1237	0.1275
—	Sub 4.1	Sub 4.2	Sub 4.3	Sub 4.4	Sub 4.5
0.1	0.0124	0.0121	0.0122	0.0119	0.0118
0.2	0.0247	0.0244	0.0244	0.0241	0.0240
0.3	0.0371	0.0368	0.0368	0.0365	0.0365
0.4	0.0493	0.0493	0.0493	0.0490	0.0492
0.5	0.0615	0.0619	0.0617	0.0616	0.0622
0.6	0.0736	0.0744	0.0741	0.0743	0.0753
0.7	0.0856	0.0869	0.0865	0.0871	0.0886
0.8	0.0975	0.0994	0.0989	0.0999	0.1021
0.9	0.1093	0.1120	0.1113	0.1128	0.1158
1.0	0.1211	0.1246	0.1237	0.1258	0.1296
—	Sub 5.1	Sub 5.2	Sub 5.3	Sub 5.4	Sub 5.5
0.1	0.0125	0.0122	0.0118	0.0118	0.0115
0.2	0.0251	0.0246	0.0240	0.0239	0.0235
0.3	0.0376	0.0372	0.0364	0.0363	0.0357
0.4	0.0501	0.0499	0.0490	0.0488	0.0483
0.5	0.0625	0.0627	0.0617	0.0616	0.0610
0.6	0.0748	0.0756	0.0745	0.0745	0.0740
0.7	0.0871	0.0886	0.0874	0.0877	0.0872
0.8	0.0992	0.1017	0.1004	0.1010	0.1006
0.9	0.1113	0.1148	0.1136	0.1144	0.1142
1.0	0.1232	0.1279	0.1268	0.1279	0.1279

C.8.3 Complete stack with three flow fields

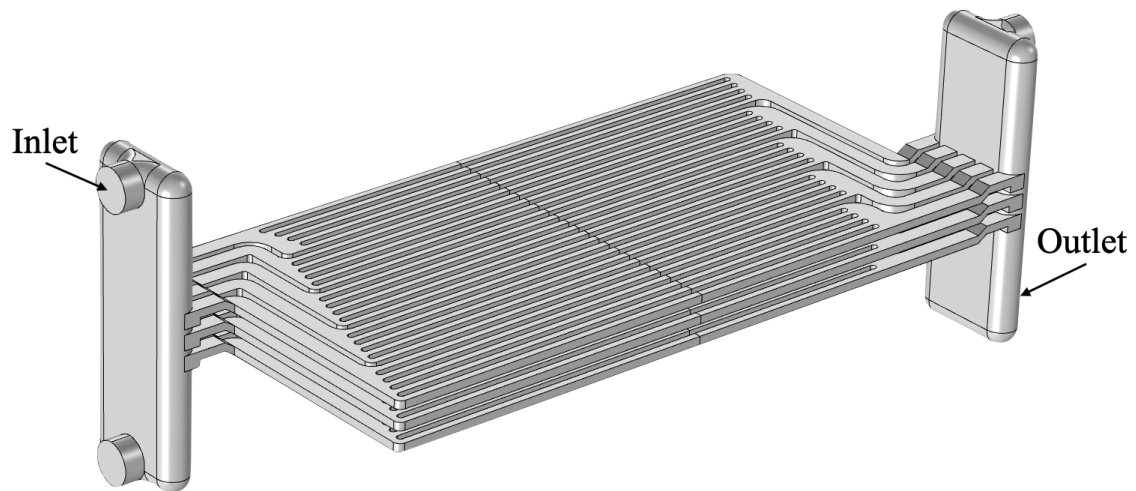


Figure C.8.3: Model used to simulate the fluid flow in the stack with three flow fields.

Table C.8.5: Results from the simulation of the stack displayed in figure C.8.3. Displaying the average velocity in each sub channel (25 per flow field with a cross section: 1.04x1.2 mm) for the flow fields in the stack, and pressure over the stack.

simulated flow rate	Average velocity [m/s]			Pressure [Pa]	
	Flow field top	Flow field mid	Flow field bot	Max pressure	Min
150 g/min	0.0242	0.0244	0.0246	126	-2
300 g/min	0.0488	0.0493	0.0498	314	-5

C.9 Fluid properties

C.9.1 Water properties

Temperature [°C]	Pressure [MPa]	Dynamic viscosity			Kinematic viscosity [m ² /s*10 ⁻⁶], [cSt]
		[Pa s], [N s/m ²]	[cP], [mPa s]	[lbf s/ft ² *10 ⁻⁵]	
0.01	0.000612	0.0017914	1.79140	3.7414	1.7918
10	0.0012	0.0013060	1.30600	2.7276	1.3065
20	0.0023	0.0010016	1.00160	2.0919	1.0035
25	0.0032	0.0008900	0.89004	1.8589	0.8927
30	0.0042	0.0007972	0.79722	1.6650	0.8007
40	0.0074	0.0006527	0.65272	1.3632	0.6579
50	0.0124	0.0005465	0.54650	1.1414	0.5531
60	0.0199	0.0004660	0.46602	0.9733	0.4740
70	0.0312	0.0004035	0.40353	0.8428	0.4127
80	0.0474	0.0003540	0.35404	0.7394	0.3643
90	0.0702	0.0003142	0.31417	0.6562	0.3255
100	0.101	0.0002816	0.28158	0.5881	0.2938

Figure C.9.1: Kinematic and dynamic viscosity of water from 0.1-100°C, edited from reference.[76]

Temperature [°C]	Density (0-100°C at 1 atm, >100 °C at saturation pressure)					Specific weight		Thermal expansion coefficient [-10 ⁻⁴ K ⁻¹]
	[g/cm ³]	[kg/m ³]	[sl/ft ³]	[lb _m /ft ³]	[lb _m /gal(US liq)]	[kN/m ³]	[lb _f /ft ³]	
0.1	0.9998495	999.85	1.9400	62.4186	8.3441	9.8052	62.419	-0.68
1	0.9999017	999.90	1.9401	62.4218	8.3446	9.8057	62.422	-0.50
4	0.9999749	999.97	1.9403	62.4264	8.3452	9.8064	62.426	0.003
10	0.9997000	999.70	1.9397	62.4094	8.3429	9.8037	62.409	0.88
15	0.9991026	999.10	1.9386	62.3719	8.3379	9.7978	62.372	1.51
20	0.9982067	998.21	1.9368	62.3160	8.3304	9.7891	62.316	2.07
25	0.9970470	997.05	1.9346	62.2436	8.3208	9.7777	62.244	2.57
30	0.9956488	995.65	1.9319	62.1563	8.3091	9.7640	62.156	3.03
35	0.9940326	994.03	1.9287	62.0554	8.2956	9.7481	62.055	3.45
40	0.9922152	992.22	1.9252	61.9420	8.2804	9.7303	61.942	3.84
45	0.99021	990.21	1.9213	61.8168	8.2637	9.7106	61.817	4.20
50	0.98804	988.04	1.9171	61.6813	8.2456	9.6894	61.681	4.54
55	0.98569	985.69	1.9126	61.5346	8.2260	9.6663	61.535	4.86
60	0.98320	983.20	1.9077	61.3792	8.2052	9.6419	61.379	5.16
65	0.98055	980.55	1.9026	61.2137	8.1831	9.6159	61.214	5.44
70	0.97776	977.76	1.8972	61.0396	8.1598	9.5886	61.040	5.71
75	0.97484	974.84	1.8915	60.8573	8.1354	9.5599	60.857	5.97
80	0.97179	971.79	1.8856	60.6669	8.1100	9.5300	60.667	6.21
85	0.96861	968.61	1.8794	60.4683	8.0834	9.4988	60.468	6.44
90	0.96531	965.31	1.8730	60.2623	8.0559	9.4665	60.262	6.66
95	0.96189	961.89	1.8664	60.0488	8.0274	9.4329	60.049	6.87
100	0.95835	958.35	1.8595	59.8278	7.9978	9.3982	59.828	7.03

Figure C.9.2: Density of water from 0.1-100°C, edited from reference.[77]

C.9.2 KOH properties

s34

GUO Ya-jie, et al/Trans. Nonferrous Met. Soc. China 20(2010) s32–36s

Table 1 Experimental densities (ρ) and viscosities (η) of ternary system (KOH+K₂CrO₄+H₂O) as a function of chromate and hydroxide concentration from 15 °C to 60 °C

c(KOH)/ (mol·L ⁻¹)	c(K ₂ CrO ₄)/ (mol·L ⁻¹)	ρ /(g·cm ⁻³)						η /(mPa·s)					
		15 °C	25 °C	30 °C	40 °C	50 °C	60 °C	15 °C	25 °C	30 °C	40 °C	50 °C	60 °C
0.507 6	0	1.025 7	1.023 9	1.022 1	1.018 3	1.014 9	1.010 9	1.204 2	0.948 2	0.852 1	0.702 1	0.590 9	0.505 7
0.498 5	0.197 5	1.058 5	1.056 8	1.054 4	1.049 5	1.044 6	1.038 8	1.233 8	0.988 3	0.891 0	0.735 4	0.619 9	0.532 5
0.501 8	0.500 5	1.099 9	1.097 2	1.095 8	1.092 2	1.087 6	1.082 8	1.306 2	1.049 5	0.946 3	0.786 6	0.667 0	0.573 8
0.503 1	0.999 0	1.170 2	1.166 9	1.165 2	1.161 8	1.156 7	1.151 5	1.452 7	1.168 3	1.060 9	0.889 0	0.753 3	0.653 3
0.502 0	2.072 9	1.296 3	1.292 3	1.290 2	1.284 1	1.279 8	1.274 5	1.826 2	1.481 0	1.346 6	1.132 3	0.970 2	0.841 6
0.503 3	2.247 0	1.337 4	1.333 2	1.330 9	1.325 1	1.321 5	1.316 2	1.963 4	1.601 5	1.467 5	1.225 1	1.049 2	0.925 4
0.995 2	0	1.050 9	1.047 9	1.046 8	1.043 2	1.038 6	1.033 9	1.267 0	1.005 1	0.905 7	0.749 3	0.631 2	0.540 5
0.997 4	0.208 6	1.080 4	1.077 2	1.076 1	1.072 4	1.068 2	1.063 4	1.315 2	1.051 6	0.947 3	0.785 1	0.663 6	0.570 1
0.998 5	0.517 4	1.124 9	1.121 5	1.120 1	1.116 3	1.111 1	1.106 9	1.393 4	1.123 8	1.017 5	0.846 6	0.718 1	0.618 6
0.997 4	1.068 6	1.195 0	1.191 2	1.189 9	1.185 6	1.181 4	1.176 7	1.579 5	1.279 8	1.163 0	0.974 0	0.830 3	0.719 4
0.998 6	1.658 3	1.260 3	1.257 1	1.255 2	1.251 2	1.247 0	1.242 2	1.749 5	1.421 7	1.293 7	1.087 2	0.928 7	0.835 4
1.012 1	2.107 7	1.311 1	1.307 2	1.305 2	1.301 8	1.296 4	1.291 9	1.921 2	1.571 3	1.440 7	1.209 6	1.037 3	0.902 0
1.497 1	0	1.073 3	1.071 1	1.068 6	1.065 8	1.060 2	1.055 9	1.336 2	1.067 8	0.962 2	0.798 7	0.672 3	0.576 6
1.503 9	0.199 1	1.105 4	1.100 4	1.098 8	1.094 5	1.090 0	1.085 5	1.392 3	1.113 0	1.006 2	0.836 4	0.707 3	0.608 1
1.499 3	0.504 4	1.148 0	1.145 2	1.142 9	1.138 2	1.133 8	1.129 3	1.476 4	1.193 4	1.083 0	0.899 6	0.806 4	0.703 7
1.500 5	1.024 0	1.212 1	1.209 2	1.208 1	1.204 2	1.198 1	1.194 5	1.637 9	1.327 2	1.204 5	1.009 2	0.857 9	0.741 9
1.507 3	1.594 3	1.281 1	1.276 3	1.274 6	1.270 1	1.266 3	1.262 0	1.877 7	1.524 6	1.385 0	1.162 4	0.992 2	0.859 7
1.508 4	1.788 1	1.322 0	1.316 2	1.314 5	1.310 1	1.305 3	1.301 2	2.098 2	1.704 9	1.534 9	1.325 5	1.098 0	0.945 9

Figure C.9.3: Density and viscosity of KOH solutions at different temperatures, edited from reference. [78]

